+UNIVERSITY OF GENOA
Polytechnic School

DIME - Department of Mechanical, Energy, Management and Transportation Engineering

PhD Thesis

PhD in Marine Science and Technology: Curriculum Technologies and System Engineering for Marine Applications (XXXVIII Course)

Title

MEDO (Multi-Energy Dispatch Optimiser): A MILP-Based Optimisation Framework for Energy Management in the Maritime Sector and Isolated Islands

Supervisor:

Prof. Alessandro Sorce

Candidate:

Andriy Vasylyev

May 2026

UNIVERSITÀ DEGLI STUDI DI GENOVA
SCUOLA POLITECNICA

DIME - Dipartimento di Ingegneria Meccanica, Energetica, Gestionale e dei Trasporti

Tesi di Dottorato

Dottorato Scienze e Tecnologie del mare Curriculum Macchine e Sistemi Energetici per il Mare (XXXVIII Ciclo)

Titolo

MEDO (Multi-Energy Dispatch Optimiser): Framework di Ottimizzazione Basato su MILP per la Gestione Energetica nel Settore Marittimo e nelle Isole Remote

Supervisore:

Prof. Alessandro Sorce

Candidato:

Andriy Vasylyev

Maggio 2026

Abstract

The present thesis addresses the increasing complexity of modern energy systems, driven by the need for decarbonisation, improved efficiency, and the integration of renewable energy sources. The maritime sector and isolated energy systems are of particular interest due to their high operational constraints, limited infrastructure, and strong dependence on fossil fuels. In such contexts, the implementation of advanced Energy Management Systems (EMS) is imperative to ensure the optimal coordination of multiple energy carriers. These include electricity, heat, fuels, and emerging vectors such as hydrogen and freshwater.

To address these challenges, this work proposes the development of the Multi-Energy Dispatch Optimiser (MEDO), a flexible, modular optimisation framework based on Mixed-Integer Linear Programming (MILP). The framework has been developed to address complex dispatch optimisation problems by balancing modelling accuracy, computational efficiency, and robustness. Nonlinear system behaviours are approximated using piecewise linearisation techniques. This enables the representation of detailed physical processes while preserving global optimality and scalability.

A thoroughgoing comparative analysis of optimisation methodologies is conducted, demonstrating that the mixed-integer linear programming (MILP) approach outperforms non-linear and heuristic approaches in terms of convergence reliability, solution optimality, and computational performance, particularly for large-scale and deterministic dispatch problems. The development of advanced component-level models is predicated on the preceding foundation. This development encompasses degradation-aware formulations for Battery Energy Storage Systems (BES) and flexible operational models for conventional power generation units, including gas turbines (GTs) and combined-cycle gas turbines (CCGTs).

The MEDO framework has been applied to a variety of real-world case studies to demonstrate its versatility and effectiveness. In the maritime domain, the tool is employed to optimise the onboard energy systems of a cruise ship. This results in fuel consumption, operational costs, and CO_2 emissions being reduced by approximately 5%, which corresponds to annual savings of around 1,450 tons of CO_2. Concurrently, the framework is being applied to isolated island energy systems, where it supports the integration of renewable energy sources, energy storage, desalination processes, and hydrogen production, enhancing system flexibility and reducing reliance on imported fuels.

The present thesis establishes a robust and adaptable link between optimisation theory and practical engineering applications. This link provides the reader with a tool for the techno-economic analysis and optimal operation of complex multi-energy systems. The proposed MEDO framework is set to contribute to the development of next-generation EMS solutions, thereby supporting the transition towards more sustainable, efficient, and resilient energy infrastructures.

Sommario

La tesi affronta la crescente complessità dei moderni sistemi energetici, dovuta alla necessità di decarbonizzazione, di miglioramento dell'efficienza e di integrazione delle fonti di energia rinnovabile. In particolare, si concentra sul settore marittimo e sui sistemi energetici isolati, che presentano elevati vincoli operativi, infrastrutture limitate e una forte dipendenza dai combustibili fossili. In tali contesti, l'implementazione di avanzati sistemi di gestione dell'energia (Energy Management Systems, EMS) risulta fondamentale per garantire il coordinamento ottimale di molteplici vettori energetici, quali l'elettricità, il calore, i combustibili e i vettori emergenti, come l'idrogeno e l'acqua dolce.

Per affrontare queste sfide, il presente lavoro propone lo sviluppo del Multi-Energy Dispatch Optimiser (MEDO), un framework di ottimizzazione flessibile e modulare basato sulla programmazione lineare intera mista (Mixed-Integer Linear Programming, MILP). Il framework è stato sviluppato per risolvere problemi complessi di ottimizzazione del dispacciamento energetico, garantendo un equilibrio tra accuratezza modellistica, efficienza computazionale e robustezza. I comportamenti non lineari dei sistemi vengono approssimati mediante tecniche di linearizzazione a tratti che consentono di rappresentare in modo dettagliato i processi fisici, preservando al contempo l'ottimalità globale e la scalabilità.

È stata condotta anche un'approfondita analisi comparativa delle metodologie di ottimizzazione dalla quale è emerso che l'approccio MILP supera gli approcci non lineari ed euristici in termini di affidabilità della convergenza, ottimizzazione della soluzione e prestazioni computazionali, in particolare per i problemi di dispacciamento deterministici e su larga scala. Su queste basi sono stati sviluppati modelli avanzati a livello di componente che includono formulazioni che tengono conto del degrado dei sistemi di accumulo elettrochimico (Battery Energy Storage Systems, BESS) e modelli operativi flessibili per le unità convenzionali di generazione elettrica, come le turbine a gas (GT) e gli impianti a ciclo combinato (Combined-Cycle Gas Turbines, CCGT).

Il framework MEDO è stato applicato a diversi casi di studio reali per dimostrarne la versatilità e l'efficacia. In ambito marittimo, lo strumento è stato utilizzato per ottimizzare i sistemi energetici di bordo di una nave da crociera, ottenendo una riduzione del 5% circa dei consumi di combustibile, dei costi operativi e delle emissioni di CO_2, pari a un risparmio annuale di 1.450 tonnellate di CO_2. Parallelamente, il framework viene applicato ai sistemi energetici insulari isolati, supportando l'integrazione di fonti rinnovabili, sistemi di accumulo energetico, processi di desalinizzazione e di produzione di idrogeno, e migliorando la flessibilità del sistema e riducendo la dipendenza dai combustibili importati.

La tesi stabilisce un collegamento solido e adattabile tra la teoria dell'ottimizzazione e le applicazioni ingegneristiche pratiche, fornendo uno strumento per l'analisi tecno-economica e la gestione ottimale di complessi sistemi multi-energetici. Il framework MEDO proposto rappresenta un contributo significativo allo sviluppo di soluzioni EMS di nuova generazione, sostenendo la transizione verso infrastrutture energetiche più sostenibili, efficienti e resilienti.

Ringraziamenti

Di solito non dedico molto tempo ai ringraziamenti, ma credo che sia il momento giusto per farlo. Per me il percorso di dottorato è stato qualcosa di inaspettato; per questo devo ringraziare il mio supervisor, Alessandro. Se non fosse per lui, molto probabilmente non avrei mai cominciato e tantomeno avrei avuto la determinazione per portare a termine il percorso di dottorato. Durante questi anni è stato fondamentale non solo dal punto di vista scientifico, che non smette mai di stupirmi, ma anche tantissimo dal punto di vista umano.

Durante questo percorso, voglio ringrazie tutti i colleghi del gruppo TPG, che sono stati una garanzia di disponibilità e supporto. In particolare, Matteo (aka presidente), Alberto (aka direttore) e il malesian dog, con i quali abbiamo condiviso momenti di felicità, ma soprattutto ci siamo stati nei momenti di difficoltà, frustrazione e incertezza durante il percorso di dottorato.

Il periodo all'International Energy Agency è stato molto complesso ma, al tempo stesso, motivante, durante il quale ho conosciuto persone incredibili e, in particolare, Jinil Kim, che mi ha fatto vivere un po' di cultura coreana a Parigi. Quelle serate con soju e somaek hanno lasciato segni indelebili che mi porterò sempre addosso.

Ovviamente tutte le persone fuori dall'ambito accademico sono state fondamentali per staccare la spina quando serviva, soprattutto i miei compagni di squadra all'Abisola. Credo sia scontato, ma doveroso, ringraziare i parenti più stretti, tra cui mia mamma e Pier Mario, per aver contribuito a loro modo.

Infine, non per ordine di importanza, voglio ringraziare Amebina, che, nonostante la mia incertezza sul futuro, ha sempre voluto farne parte fin dall'inizio di ogni mio percorso. Grazie per esserci stata. Spero che anche in futuro tu abbia la pazienza e, soprattutto, la resistenza per sopportare i miei mille cambi di programma, che patisci così tanto. Come sempre, un tanto più di te!

List of Publications

1. Vasylyev, A., Vannoni, A., and Sorce, A., 2023, “Best Practices for Electricity Generators and Energy Storage Optimal Dispatch Problems,” Journal of Gas Turbine and Power, 146(3). https://doi.org/https://doi.org/10.1115/1.4063529.
2. Vasylyev, A., Vannoni, A., and Sorce, A., 2023, “Optimal Dispatch of Battery Energy Storage Considering Cycling and Calendar Ageing,” E3S Web of Conferences. https://doi.org/10.1051/e3sconf/202341401004.
3. Vasylyev, A., Vannoni, A., and Sorce, A., 2025, “Optimal Dispatch of Li-Ion Battery Energy Storage, Reviewing and Considering Cycling and Calendar Ageing Models,” Appl. Therm. Eng., 265. https://doi.org/10.1016/j.applthermaleng.2025.125597.
4. Cavo, M., Mantelli, L., Rivarolo, M., and Vasylyev, A., 2023, “A MILP Approach for Hybrid Energy Systems Design for Sustainable Maritime Mobility,” 36th International Conference on Efficiency, Cost, Optimisation, Simulation and Environmental Impact of Energy Systems, ECOS 2023. https://doi.org/10.52202/069564-0131.
5. Vasylyev, A., Passalacqua, M., Mantelli, L., Rivarolo, M., and Sorce, A., 2024, “Piecewise-Linear MILP Optimisation for Energy System Design On-board Hybrid Ships,” Journal of Physics: Conference Series, Institute of Physics. https://doi.org/10.1088/1742-6596/2893/1/012040.
6. Vasylyev, A., and Sorce, A., 2024, “Optimisation of Reversible Heat Pumps Utilising Waste Heat from Electric Power Plants,” Journal of Physics: Conference Series. https://doi.org/10.1088/1742-6596/2893/1/012048.
7. Vasylyev, A., Dubey, A., Malamaki, K.-N. D., Andriopoulos, N., Apostolidou, N., and Sorce, A., 2025, Long-Term Strategy To Optimise RES Penetration In Isolated Grid, Paris (FR).
8. Vasylyev, A., Bozzolo, M., Passalacqua, M., Machaj, K., Maria de Càssia Crispim, A., Anfosso, C., Bellotti, D., Baldinelli, A., Pineider, F., and Sorce, A., 2025, Strategies For Solar-Driven Fresh Water And Hydrogen Production In Island Scenarios, Paris, (FR).
9. Saadeldin, M., Vasylyev, A., Rivarolo, M., and Sorce, A., 2026, “Feasibility Analysis of Hydrogen Fuel Cell-Powered Passenger Vessels: A Multi-Criteria and MILP-Based

Analysis for Sustainable Inland Navigation," Ocean Engineering, 349. https://doi.org/10.1016/j.oceaneng.2026.124186.

Tables of Contents

List of Figures

List of Tables

Nomenclature

Acronymous

BC	Bottoming Cycle
BES	Battery Energy Storage
BOP	Balance of Plant
CAPEX	Capital Expenditure
CCGT	Combined Cycle Gas Turbine
CHP	Combined Heat and Power
COE	Cost Of Electricity
CPS	Current Policies Scenario
C-rate	Current Rate
CRF	Capital Recovery Factor
CSS	Clean Spark Spread
DoD	Depth of Discharge
EC	Electrolyser
ED	Electrodialysis
EDR	Electrodialysis Reversal
EH	Electric Heater
EMS	Energy Management System
EOH	Equivalent Operating Hours
FB	Faired Boiler
FC	Fuel Cell
FH	Fired Hours
GHG	Green House Gas
GT	Gas Turbine
HFO	Heavy Fuel Oil
HGPI	Hot Gas Path Inspection
HP	Heat Pump
ICE	Internal Combustion Engine
IGV	Inlet Guide Vanes
IMO	International Maritime Organization
KPI	Key Performance Indicator
LCOW	Levelised Cost of Water
LHV	Low Heating Value
MAE	Mean Absolute Error
MAPE	Mean Absolute Percentage Error
MDO	Marin Diesel Oil

MED	Multi-Effect Distillation
MEDO	Multi Energy Dispatch Optimiser
MEL	Minimum Environmental Load
MES	Multi Energy Systems
MFS	Multi-Stage Flash
MILP	Mix Integer Linear Programing
MVC	Mechanical Vapor Compression
NEC	Net Energy Consumption
NTC	Net Transmission Capacities
O&M	Operation and Maintenance
OP	Operational Profits
OPEX	Operating Expenditure
PEM	Proton Exchange Membrane
PFR	Primary Frequency regulation
RC	Reverse Cell
RH	Rolling Horizon
RO	Reverse Osmosis
rSOC	reversible Solid Oxide Cell
SOC	Solid Oxide Cell
SoC	State of Charge
SoH	State of Health
SP	Saved Periods
SSH	Stand Still Hours
STEPS	The Stated Policies Scenario
SW	Simulation Window
TBT	Top Brine Temperature
TES	Thermal Energy Storage
TP	Total Periods
TVC	Thermal Vapor Compression
VC	Vapor Compression
VRE	Variable Renewable Energy
ZP	Zonal Price

Variables

t	time	h
T	Temperature	°C
P	Power	kW
onoff	binary on-off variable	-
m	fuel	kg
C_{SU}	Start Up Cost	€/SU
C_{gas}	Gas Cost	€/kWh

C_{CO2}	CO2 Tax	€/ton
e	emission factor	kg/kWh
FH	Fired Hour	h
C_{SD}	Shut down cost	€/SD

Chapter 1

Introduction and Motivation

The global energy sector is currently experiencing a period of significant transformation, driven by the pressing need to reduce greenhouse gas emissions, enhance energy efficiency, and integrate renewable energy sources into existing infrastructure. This transition is especially challenging in sectors characterised by high energy intensity and operational complexity, such as maritime transportation and isolated energy systems. In such contexts, energy management is of critical importance in ensuring economic viability, operational reliability, and environmental sustainability.

The maritime sector, which has historically relied on fossil fuels, is now facing mounting regulatory pressure to reduce its carbon emissions while adhering to stringent operational constraints [1,2]. Similarly, isolated islands and remote grids encounter unique challenges due to limited interconnection capacity, high dependence on imported fuels, and growing penetration of variable renewable energy sources. In both cases, the efficient coordination of multiple energy carriers, such as electricity, heat, and fuels, requires advanced Energy Management Systems (EMS) capable of handling complex, multi-vector interactions.

A fundamental challenge in such systems pertains to the optimal allocation of generation and storage resources. The process of dispatch optimisation involves the strategic scheduling of energy resources over time, with the objective of either meeting demand or maximising economic performance, while ensuring that technical constraints are adhered to. However, the increasing complexity of modern energy systems, characterised by hybrid configurations, stochastic renewable generation, and nonlinear component behaviour, poses significant challenges for traditional optimisation approaches.

Existing methodologies encompass a range of approaches, from linear programming techniques, which offer computational efficiency and global optimality, to nonlinear and heuristic methods that capture detailed physical behaviour. However, these latter methods frequently encounter convergence issues and high computational cost. In this context, the identification of a modelling framework that balances accuracy, robustness, and scalability is of paramount importance.

This thesis proposes a solution to these challenges through the development of the Multi-Energy Dispatch Optimiser (MEDO), a Mixed-Integer Linear Programming (MILP)-based framework designed for the optimal management of complex energy systems. The proposed approach utilises linearisation techniques to approximate the nonlinear system behaviour, while preserving computational tractability and ensuring global optimality.

The impetus for this work is based on the following objectives:

- Identify the most appropriate optimisation framework for dispatching problems by comparing various nonlinear approaches, such as genetic algorithms and the more traditional MILP modelling.
- Provide a robust and flexible optimisation framework capable of handling multi-energy systems in both maritime and isolated grid applications. Managing all nonlinearities in the modelled components through the piecewise linearisation technique and the Big-M method.
- The development of advanced modelling approaches for key system components, including battery energy storage systems. Such approaches must incorporate degradation-aware cost formulations.
- In the context of traditional power plants such as GT and CCGT, the development of a flexible solution is essential for enhancing the adaptability of these components to the new grid requirements.

The integration of these elements is intended to contribute to the development of EMS tools that support the transition towards more sustainable and efficient energy systems. The MEDO framework has been designed to be modular and adaptable, thus enabling its application across a wide range of scenarios, from onboard ship energy systems to remote island microgrids.

The objective of this work is to establish a connection between theoretical optimisation methods and practical engineering applications, thereby providing a tool that is both mathematically rigorous and industrially relevant.

Chapter 2

Global Scenario

The global energy landscape is currently experiencing a period of rapid transformation, driven by the need to address multiple challenges in a coordinated manner. These include ensuring secure energy production (both electricity and heat) to meet growing demand, while continuously reducing greenhouse gas (GHG) emissions and air pollutants. Figure 2.1 illustrates the historical trends in GHG emissions for the major regions.

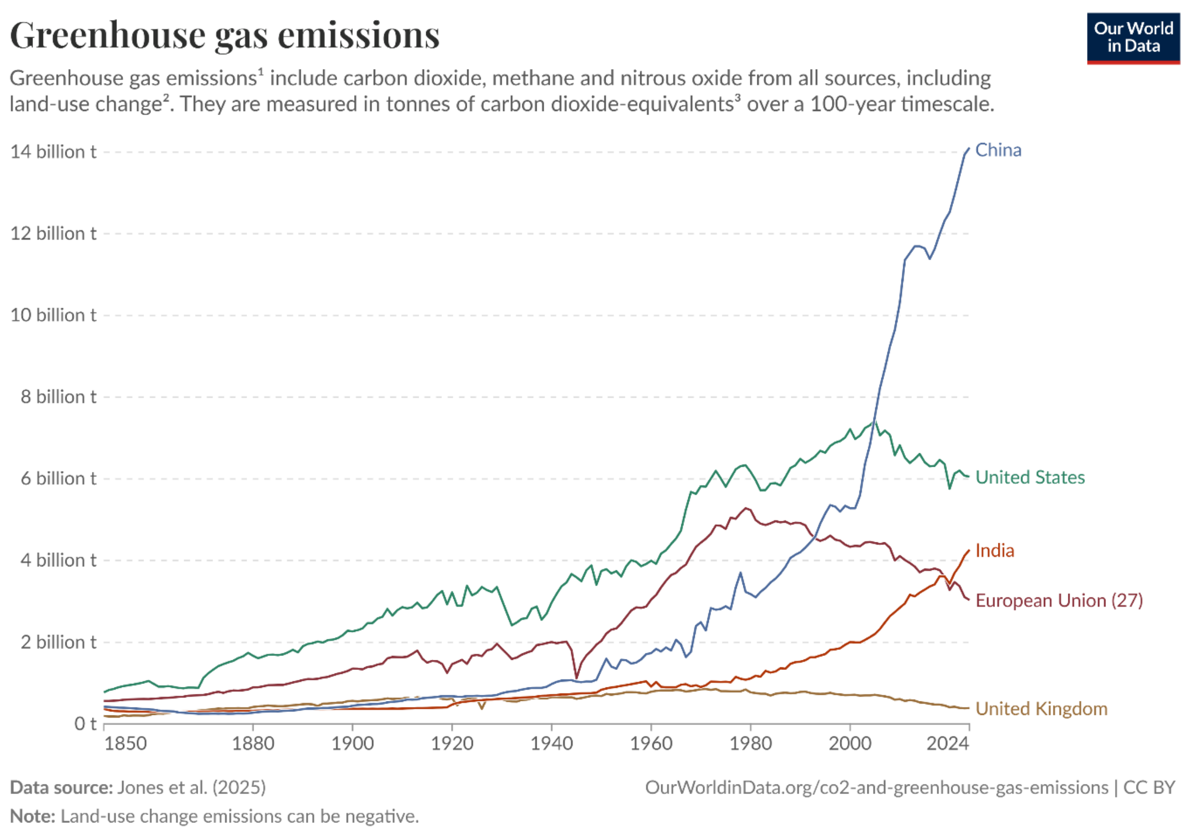

Figure 2.1: Annual CO2 emissions by world region [3].

As demonstrated in Figure 2.2, the contribution of CO_2 emissions by sector is illustrated. As is evident, the three sectors responsible for the majority of emissions, approximately 70%, are the power industry, industrial combustion and processes, and transportation. Consequently, it has become imperative to adopt a cross-sectoral approach across all sectors in order to reduce greenhouse gas (GHG) emissions.

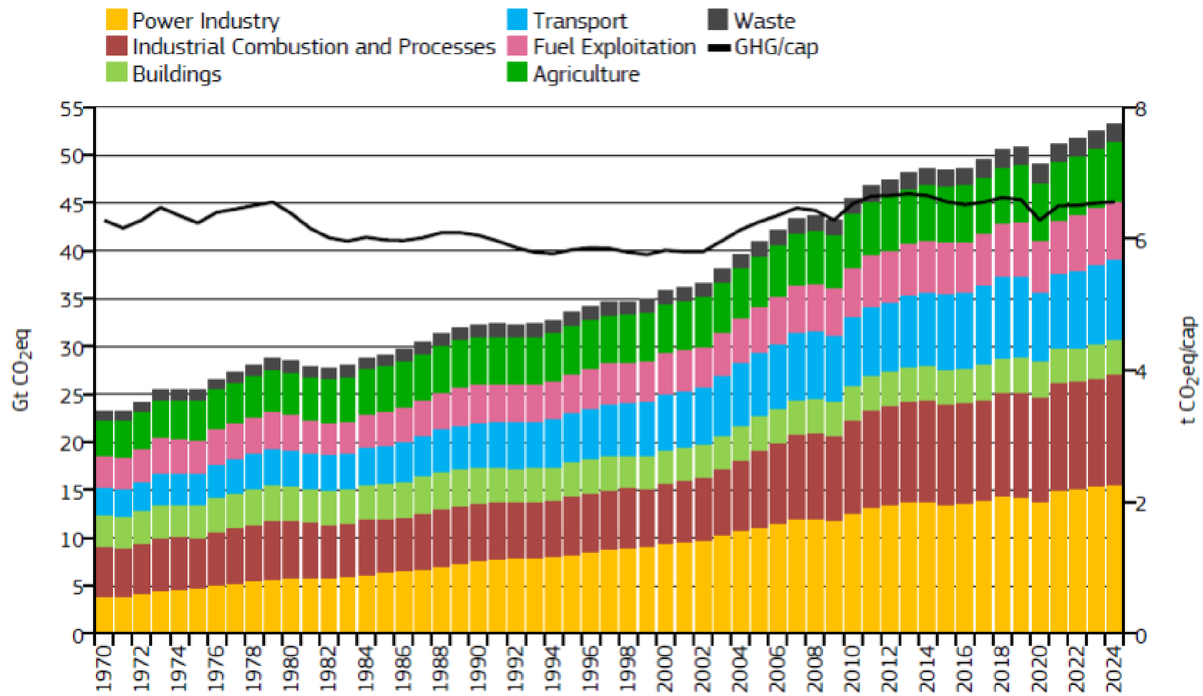

Figure 2.2: Global GHG emissions by sector (left axis, bars) and per capita (right axis, black line), 1970-2024 (in Gt $CO2_{eq}$) [4]

The Stated Policies Scenario (STEPS) and the Current Policies Scenario (CPS) offer two distinct perspectives on the potential evolution of the global energy system as outlined by International Energy Agency *[5]*. Despite these differences, both scenarios indicate similar overarching trends. In particular, they project a continued increase in energy demand, driven by a growing and increasingly affluent global population requiring more energy services.

According to the latest projections from the STEPS project, the total energy demand is anticipated to rise by around 55 exajoules (EJ) by the year 2035. This represents an 8% increase compared to current levels. In contrast, the CPS projects a more rapid growth, with demand increasing by around 90 EJ, or 14%, over the same period (Figure 2.3) [5].

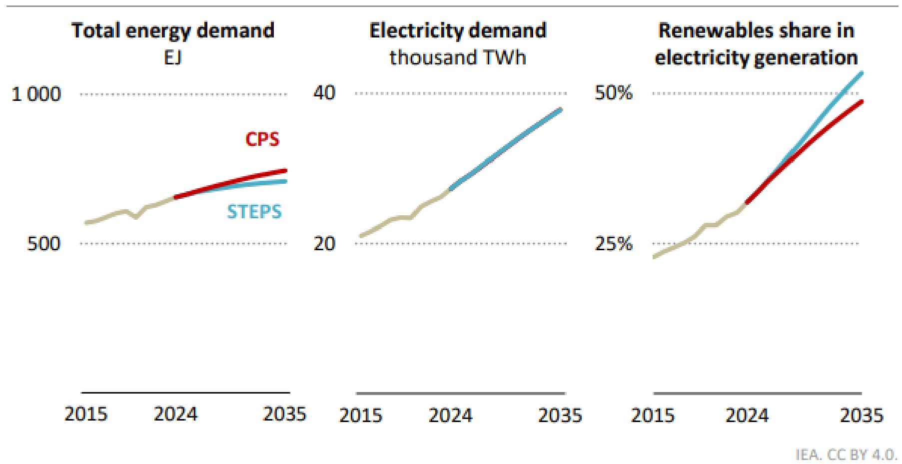

Figure 2.3: Total energy demand, electricity demand, and renewables in electricity generation by scenario, 2015-2035 [5].

While the electrical demand remains broadly similar in both scenarios, the divergence in total energy demand is primarily attributed to differences in technological efficiency and fuel use. It is important to note that around 60% of the difference between the two scenarios is due to the higher reliance on fossil fuels in electricity generation and transport within the CPS, resulting in greater energy losses in the form of waste heat. Furthermore, the implementation of stronger efficiency policies in the STEPS contributes to moderating the growth in energy demand relative to the CPS [5].

The demand for the three main fossil fuels follows divergent trajectories in the STEPS and CPS scenario, with specific factors explaining the differences observed in each case (Figure 2.4). Demand for coal is particularly sensitive to developments in the power sector. Around 55% of global coal consumption is attributed to electricity generation in emerging market and developing economies, notably China. Consequently, the outlook for coal demand is closely linked to the rate of renewable energy deployment. In the STEPS, the average annual increase in renewable capacity in these regions is expected to be approximately 620 gigawatts (GW) up to 2035, compared with 515 GW in 2024. This sustained growth is sufficient to drive a decline in global coal demand within this decade. In contrast, the CPS is hindered by weaker policy support and greater challenges related to grid integration, which slow the expansion of renewables. Consequently, demand for coal remains higher, peaks later and declines more gradually. However, in both scenarios, global coal demand is projected to begin decreasing before the end of the decade.

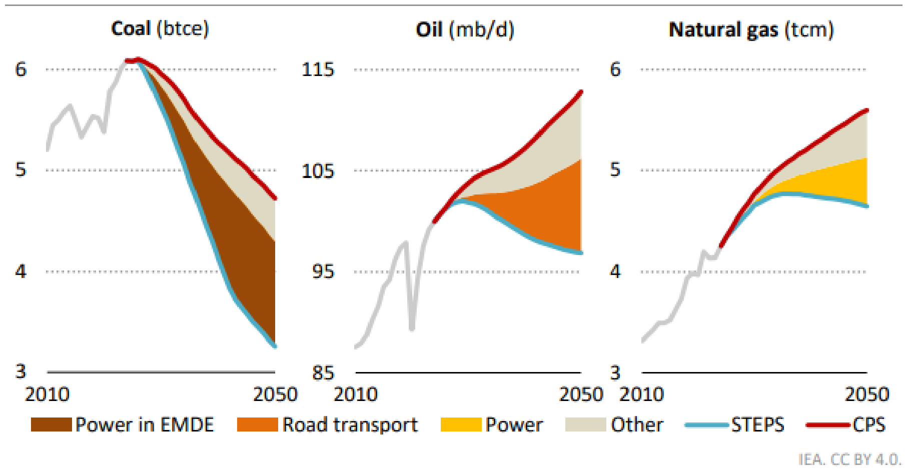

Figure 2.4: Demand for coal, oil and gas by major driver and scenario, 2010-2050 [5].

Oil demand is predominantly driven by the transport sector (Figure 2.4), with road transport accounting for approximately 45% of global consumption. Its future trajectory is strongly influenced by improvements in the efficiency of internal combustion engine (ICE) vehicles and the adoption of electric vehicles (EVs). In the STEPS scenario, the share of EVs in global car sales is projected to double by 2030 and exceed 50% by 2035, leading to a decline in oil demand from road transport and a peak in total oil demand around 2030. In contrast, in the CPS, EV adoption slows, with the sales share plateauing after 2035, while improvements in ICE vehicle efficiency continue broadly in line with historical trends. As a result, total oil demand in 2035 is approximately 5 million barrels per day (mb/d) higher in the CPS than in the STEPS, with around 40% of this difference attributable to slower EV uptake. The stagnation in EV market share in the CPS is set to contribute to continued growth in oil demand throughout the 2030s and beyond.

There are also notable differences in natural gas demand between the two scenarios (Figure 2.4), particularly in the power sector. In the STEPS project, the expansion of renewable energy has been identified as a key factor in the decline of gas-fired electricity generation in major consuming regions, with Europe and advanced Asian economies experiencing notable decreases. It is estimated that global natural gas use for electricity generation will increase by slightly less than 10% by 2035. However, the CPS is experiencing a slower deployment of renewables and alternative generation sources, leading to a stronger reliance on natural gas. As a result, demand in the power sector is rising by more than 15%. Consequently, global natural gas demand reaches a plateau in the mid-2030s in the STEPS, whereas it continues to grow in the CPS. It is important to note that, according to the most recent STEPS outlook, this plateau is occurring later and at a higher level than was indicated in previous assessments.

The IEA's different scenarios show how the global focus on the environment is ongoing with particular focus on the reduction of GHG. In response to these pressing challenges, new international agreements and policies have been introduced over time. The first attempts to reduce air pollution took place in the late 1970s. A significant milestone was the adoption of the Kyoto Protocol in 1997, which came into effect in 2005 and established the framework for subsequent international climate agreements. However, the protocol has been the subject of significant criticism, as binding emission reduction commitments were primarily imposed on developed countries, while global emissions continued to rise compared to 1990 levels [6].

A more comprehensive approach was introduced with the Paris Agreement, adopted in 2015 and entering into force in 2016. This agreement set more ambitious goals, aiming to limit the increase in global average temperature to well below 2°C above pre-industrial levels, while pursuing efforts to restrict it to 1.5°C. In contrast to the Kyoto Protocol, the Paris Agreement calls for contributions from both developed and developing countries, including major emitters in the Global South such as China and India [7].

2.1 Strategies and regulations for decarbonisation in maritime transportation

As the preceding analysis has shown, reducing emissions from the maritime sector is important to achieving global climate objectives. In response, the International Maritime Organization (IMO) and major global economies have established specific targets and regulatory frameworks aimed at steering the shipping industry towards full decarbonization. In order to enhance comprehension of the prevailing policy environment, a thorough review has been undertaken, incorporating the viewpoint of the IMO and major stakeholders such as the European Union, the United States, China, and Japan.

The IMO has developed a comprehensive framework at the international level with the aim of reducing sulphur oxides (SO_x), nitrogen oxides (NO_x) and greenhouse gases (GHG). It is important to note that SO_x and NOx emissions, which originate from fuel combustion, pose significant risks to human health and the environment. In order to mitigate the aforementioned impacts, Emission Control Areas (ECAs) have been established on a global scale, with more stringent limits on these pollutants being enforced [8].

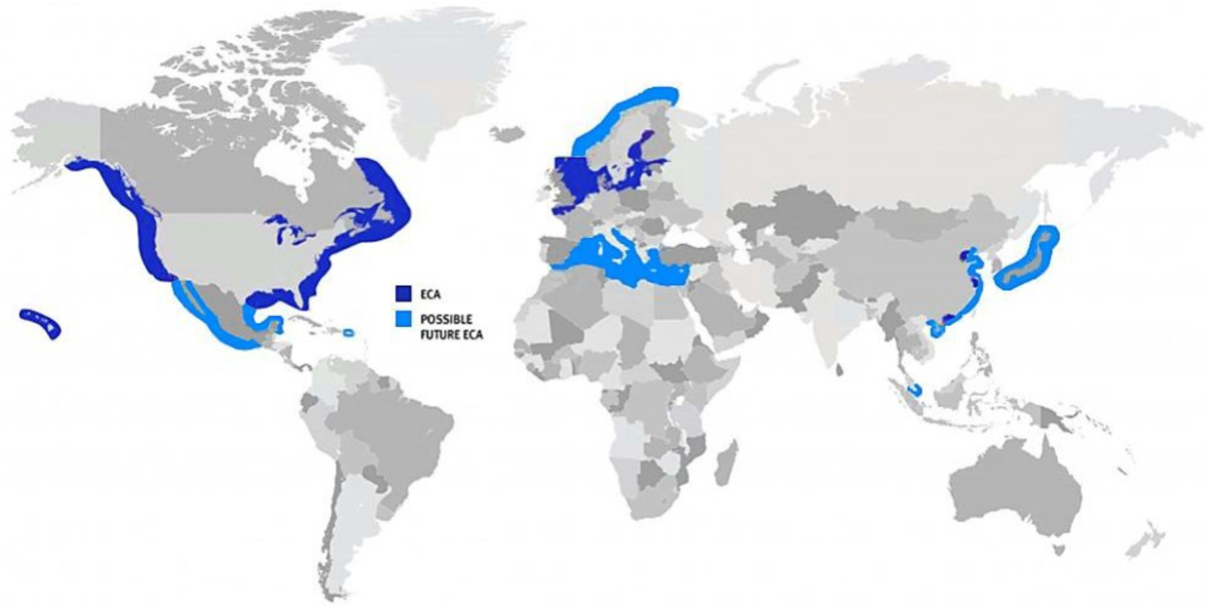

Figure 2.5: Worldwide ECAs.

With regard to greenhouse gas emissions, the IMO's Marine Environment Protection Committee (MEPC) finalized a revised strategy in July 2023. The following indicative targets have been established by the updated framework (using 2008 as the baseline year). The following targets have been set out for 2030, 2040 and 2050 respectively :

- A reduction in Well-to-Wake (WtW) greenhouse gas (GHG) emissions of at least 20%, with a target of 30%;
- A reduction of at least 70%, with a target of 80%, by 2040;
- The achievement of net-zero emissions "by or around" 2050;
- At least 5%, with a target of 10%, of energy used in international shipping to come from zero or near-zero greenhouse gas emission fuels and technologies by 2030.

To support these objectives, the IMO has introduced a set of measures, which have been categorised into the following three timeframes: short-, mid- and long-term actions.

Short-term measures primarily concentrate on enhancing energy efficiency. These include the Carbon Intensity Indicator (CII), the Energy Efficiency Existing Ship Index (EEXI), and the Ship Energy Efficiency Management Plan (SEEMP). The objective of these instruments is to enhance operational and technical efficiency without prescribing specific fuel choices [9].

The mid-term measures currently under development consist of a combination of technical and economic instruments. The technical component involves the introduction of a goal-based marine fuel standard, designed to progressively reduce the GHG intensity of marine fuels. It is anticipated that the economic component will encompass a maritime GHG pricing mechanism, which may be associated with fuel intensity regulations. A number of additional measures are currently under consideration, including the implementation of guidelines for lifecycle assessment (LCA), the establishment of mechanisms to gather feedback on implementation, and the introduction of incentives to encourage the adoption of innovative technologies.

The long-term measures are yet to be defined, with the objective of ensuring alignment with the net-zero emissions target by 2050.

Chapter 3
Optimisation Algorithms

The existing literature offers a wide range of methodologies for modelling optimisation problems, spanning from linear to highly nonlinear formulations. Dispatch problems may therefore be classified as linear or nonlinear, depending on how accurately the physical behaviour of the system is represented and on the degree of modelling complexity adopted. Nonlinear models generally allow for a more detailed description of component performance, start-up dynamics, efficiency curves, and operational constraints. However, this increased level of detail often results in non-convex formulations, higher computational burden, and the risk of convergence to local optima.

The objective of this chapter is to provide a comparative analysis of the various optimisation approaches implemented in MATLAB [10–13], with a view to identifying the most suitable mathematical framework for dispatch applications. The analysis demonstrates that a highly detailed nonlinear formulation, while more faithful to the physical behaviour of the system, may result in suboptimal economic outcomes due to numerical instability, sensitivity to initial conditions, or convergence issues. Conversely, a properly structured simplified formulation, such as a linear or Mixed-Integer Linear Program (MILP) model, can provide more robust and globally optimal solutions while preserving the essential operational constraints of the generators. The findings indicate that meticulous abstraction of nonlinearities, in conjunction with effective optimisation management, facilitates the derivation of operating schedules that are not only computationally efficient but also economically more advantageous across diverse generations of technologies.

3.1 Linear Programming (LP)

Linear programming (LP) is a widely used method in the field of dispatch modelling problems, as it allows for the optimal allocation of resources while satisfying a set of operational constraints. In energy system dispatch applications, the objective is generally to ascertain the most profitable operational schedule for generation units and storage systems over a specified timeframe, with a view to optimising economic profit or minimising operational costs. In an LP formulation, the objective function and all constraints are linear with respect to the decision variables, which generally represent quantities such as power output, energy flows, or charging and discharging levels of storage systems. The constraints delineate the physical and operational limits of the system, encompassing power balance requirements, generation limits, ramping limits, and capacity constraints. Linear programming is a particularly advantageous technique due to its computational efficiency and the fact that it guarantees convergence to a global optimum, provided that the problem remains linear and convex. For this reason, LP-based approaches are commonly adopted in electricity market modelling and short-term dispatch optimisation, especially when system behaviour can be reasonably approximated using linear relationships. However, when nonlinear phenomena such as efficiency curves, startup costs, or complex operational dynamics are included, the problem formulation may require more advanced techniques such as nonlinear or mixed-integer optimisation methods. Please refer to Eq.3.1 below for the mathematical formulation of the linear problem [14–16].

$$\min_{x} f(x) \; constrained \; at \begin{cases} A \cdot x \leq b \\ A_{eq} \cdot x = b_{eq} \\ lb \leq x \leq ub \end{cases} \qquad 3.1$$

As previously stated, given that this is a highly simplified representation of engineering problems, there is no in-depth discussion of comparing algorithms. Instead, there is a focus on a more comprehensive methodology, Mixed-Integer Linear Programming (MILP), that allows for the inclusion of complex and nonlinear physics behaviour of real engineering application problems through various linearisation techniques.

3.2 Mixed Integer Linear Programming (MILP)

Mixed-Integer Linear Programming (MILP) is a widely used tool in the field of dispatch optimisation. It allows the inclusion of both continuous and integer decision variables while maintaining a linear formulation of the objective function and constraints. In the field of dispatch modelling, continuous variables commonly represent quantities such as power generation levels or energy flows. Conversely, integer or binary variables are used to model discrete operational decisions, such as unit commitment, start-up and shutdown states, or charging/discharging conditions of storage systems. Equation 3.2 below presents the mathematical formulation of the optimisation problem, accounting for both continuous and binary variables.

$$\min_{x} f^T x \text{ subject to } \begin{cases} x(intcon) \text{ are integers or extended integers} \\ A \cdot x \leq b \\ A_{eq} \cdot x = b_{eq} \\ lb \leq x \leq ub \end{cases} \qquad 3.2$$

In MATLAB, MILP problems can be solved using the *intlinprog* solver, which implements a combination of preprocessing techniques, cutting planes, heuristics, and a branch-and-bound search strategy. The algorithm first performs a preprocessing phase to simplify the optimisation problem by eliminating redundant constraints, tightening variable bounds, and improving the numerical structure of the model. After the preliminary processing stage, the solver performs a linear programming relaxation of the MILP. In this process, the integer constraints are temporarily removed to obtain an initial bound on the objective function. To enhance the quality of this relaxation, the solver generates additional linear constraints, known as cuts. These include Gomory cuts, clique cuts and mixed-integer rounding cuts. The purpose of the cuts is to reduce the feasible region and to push the solution closer to integer feasibility. Heuristic procedures are also applied to swiftly identify feasible integer solutions that can provide improved bounds for the optimal solution. Finally, the solver applies a branch-and-bound algorithm that systematically partitions the problem into smaller subproblems by imposing additional bounds on integer variables. Each subproblem is solved through LP relaxation, producing upper and lower bounds on the objective function. The algorithm continues to explore and prune branches of the search tree until the optimal integer solution is found or a predefined convergence tolerance is satisfied. This combination of techniques allows MILP solvers to efficiently handle complex dispatch optimisation problems with discrete operational decisions while guaranteeing convergence to the global optimum for linear formulations [17–19].

In addition to the solvers available in MATLAB, several commercial optimisation solvers are widely used for solving MILP problems in dispatch optimisation. These solvers are specifically designed to handle large-scale optimisation problems with thousands or even millions of variables and constraints, which commonly arise in energy system dispatch and unit commitment models. The following commercial solvers are among the most widely adopted: Gurobi Optimiser, IBM ILOG CPLEX, FICO Xpress and MOSEK.

These solvers implement highly advanced MILP algorithms based on branch-and-bound and branch-and-cut frameworks, combined with sophisticated preprocessing techniques, cutting-plane generation, primal heuristics, and parallel computing capabilities. In comparison to general-purpose open solvers, commercial MILP solvers generally offer substantial performance enhancements, especially in the context of complex dispatch problems that incorporate binary variables to represent unit commitment decisions, start-up and shutdown states, and operational constraints. In addition, they incorporate advanced features such as automatic scaling, presolve reductions and warm-start capabilities. These features can significantly reduce computational time when solving large scheduling problems over extended time horizons. For this reason, commercial MILP solvers are frequently adopted in industrial energy planning tools, electricity market simulations, and power system operation studies. In such contexts, the tools must be both highly computationally efficient and reliable. During the optimisation comparison phase, it was decided to use only those implemented in MATLAB. During the MEDO Tool development phase, however, the commercial software Gurobi was used, thanks to its very high computational capabilities.

3.3 Non-linear Programming (NLP)

Nonlinear Programming (NLP) is the minimisation or maximisation of an objective function subject to a set of equality and inequality constraints, at least one of which is nonlinear. In the context of energy system dispatch modelling, the objective function typically maximises economic profit or minimises operational costs. Concurrently, the constraints describe the technical and operational limits of the system, including minimum and maximum power output, ramp rates, operational states, and energy balances.

Nonlinear optimisation techniques have been identified as particularly effective for modelling energy systems. In such systems, efficiency curves, operating limits, and cost functions frequently give rise to nonlinear relationships. Consequently, several algorithms for solving nonlinear problems implemented in the MATLAB Optimisation Toolbox and the Global Optimisation Toolbox have been considered in addressing the dispatch optimisation problem. Optimisation is the process of identifying the minimum point of a function. The distinction between relative minima and global minima needs clarification. It can be demonstrated that a relative minimum of $f(x)$ is characterised by a point x_0 such that, within its neighbourhood *I*, $f(x_0)$ is less than or equal to $f(x)$ calculated at any point belonging to *I*. This condition is expressed in Eq. 3.3. Conversely, a global minimum is defined as a specific point, designated x_0, where $f(x_0)$ is less than or equal to the value $f(x)$ ascertained at all other admissible points within the specified domain, *D*. The necessary condition can be found in Eq. 3.4.

$$x_0 \ local \ minimum \ if \ \exists \ I_{x_0}: \forall x \in I_{x_0} \cap D \ \rightarrow f(x_0) \leq f(x) \tag{3.3}$$

$$x_0 \ global \ minimum \ if: \forall x \in D \ \rightarrow f(x_0) \leq f(x) \tag{3.4}$$

For all optimisers implemented in Matlab suitable for the dispatching problems, the problem formulation is defined by Eq. 3.5. This equation represents the general formulation of the optimisation problem. Within Eq. 3.5 several terms are introduced briefly here. The left-hand side of the equation represents the objective function to be minimised. The terms positioned on the right-hand side of the bracket represent the constraints that can be imposed on the solution.

$$\min_x f(x) \ constrained \ at \begin{cases} A \cdot x \leq b \\ A_{eq} \cdot x = b_{eq} \\ lb \leq x \leq ub \\ c_{eq}(x) = 0 \\ c(x) \leq 0 \end{cases} \tag{3.5}$$

In accordance with the established sequence, the initial set of constraints pertains to linear inequality constraints. In this context, A denotes the matrix of coefficients associated with the aforementioned inequality constraints, given by the following expressions. It is imperative to note that the number of columns of matrix A must be equal to the number of decision variables in the optimisation problem. In contrast, the number of rows represents the number of inequality constraints. This number must correspond to the number of rows of b, which contains the bounds associated with the linear inequality constraints. Each row of the matrix A represents a single inequality constraint. A similar structure applies to the linear equality constraints, as represented by the second row of the formulation. In this particular instance, A_{eq} denotes the matrix containing the coefficients associated with the equality constraints, whilst b_{eq} signifies the corresponding equality constraint values. The third set of constraints delineates the limits on the decision variables. The aforementioned limits ensure that the values of the unknown variables remain within a specified range. In particular, *lb* represents the lower bounds and *ub* represents the upper bounds. The dimensions of *lb* and *ub* must equal the number of decision variables in the optimisation problem. To avoid numerical issues, most solvers do not accept unconstrained variables.

Furthermore, the presence of nonlinear constraints cannot be discounted. The non-linear constraints are provided to the optimisation algorithm via the function *c(x)*. In a similar manner to the linear case, nonlinear constraints can also be expressed as inequality or equality constraints [10,12,13].

For this stage of the analysis, the only algorithm considered from the Optimisation Toolbox is *fmincon*. This solver has been developed to address constrained nonlinear optimisation problems. This process enables minimising a nonlinear objective function subject to both equality and inequality constraints. There are a number of algorithms that can be selected within *fmincon* for the purpose of optimisation [13].

- Interior Point algorithm, [20–22]
- Trust Region Reflective algorithm, [23]
- Sequential Quadratic Programming (SQP) algorithm, [24,25]
- legacy SQP algorithm, [25]
- Active Set algorithm, [16,26,27]

One constraint of fmincon is the requirement to specify an initial point. Consequently, the obtained optimum may be significantly influenced by the initial solution, potentially leading the solver to converge to different local minima. This issue becomes particularly important as the complexity of the optimisation problem increases.

Within the Global Optimisation Toolbox [12], four algorithms were considered:

A Genetic Algorithm (GA) is a method for solving optimisation problems, both constrained and unconstrained, based on a process of natural selection that mimics biological evolution. The algorithm repeatedly modifies a population of candidate solutions. At each iteration, individuals are randomly selected from the population and used as parents to generate the next generation. Over successive generations, the population evolves towards an optimal solution. Genetic algorithms are particularly suitable for problems that are difficult to solve using standard optimisation techniques, such as those with discontinuous, non-differentiable, stochastic, or highly nonlinear objective functions [28–30].

The Surrogate Optimisation (surrogateopt) algorithm uses a surrogate function to approximate the original objective function. The surrogate model is a valuable tool that allows for rapid evaluation of the original function. Therefore, the optimiser performs the search by minimising the surrogate function instead of the computationally expensive original function. Surrogate optimisation is a suitable approach for problems where the objective function requires substantial computational effort to evaluate. The objective function need not be smooth, but the algorithm performs better when it is continuous. The optimisation process commences with a set of points, which are either randomly generated or supplied by the user. The optimiser then evaluates the objective function at these points and constructs an initial surrogate model through interpolation or fitting. At each iteration, the algorithm generates multiple candidate points and evaluates them using a merit function. The most suitable candidate is then evaluated using the original objective function, and the obtained value is used to update the surrogate model [31,32].

Patternsearch is a direct search method for finding the minimum of a function that need not be differentiable, stochastic, or even continuous. In contrast to conventional optimisation techniques that depend on gradient or higher-order derivative data, pattern search algorithms rely solely on objective function evaluations. The algorithm generates a sequence of points that progressively approach the optimal solution. At each step, the algorithm explores a set of points, known as a mesh, around the current point. The mesh is generated by adding scalar multiples of a fixed set of vectors, called pattern vectors, to the current point. If a point within the mesh yields a lower objective value than the current point, that point becomes the new current point for the next iteration [30,33].

The Pareto search algorithm is somewhat unconventional in this study, as it is generally designed for multi-objective optimisation problems. Such problems are common in engineering practice, especially when evaluating trade-offs between conflicting objectives, such as profit maximisation and emission minimisation. A Pareto improvement is a new solution that is created using an initial solution as a foundation. This new solution improves at least one objective without worsening any other objective. A solution is said to be Pareto-dominated if there exists a Pareto improvement. A solution is deemed Pareto-optimal or Pareto-efficient if no further Pareto improvements are possible. The set of all Pareto-efficient solutions is known as the Pareto front. In this thesis, only one objective function was considered. Therefore, it can be concluded that the Pareto front degenerates into a single optimal point [34,35].

3.4 Why MILP is preferable for dispatching problems

To identify the most appropriate optimisation algorithm, a dedicated sensitivity analysis was performed on two case studies representative of distinct technological paradigms: a conventional Combined Cycle Gas Turbine (CCGT) unit and a Battery Energy Storage (BES) system. These two applications capture fundamentally different operational characteristics: continuous thermal generation with commitment constraints in the case of CCGT, and intertemporal energy arbitrage with state-of-charge coupling in the case of BES. Thus, they provide a comprehensive benchmark for dispatch optimisation problems.

The objective of this comparative evaluation is to ascertain the most appropriate methodological framework for dispatch applications across heterogeneous technologies. To ensure consistency and fairness in the evaluation process, all tested algorithms were formulated using the same objective function and identical operational constraints. Consequently, any observed disparities in performance can be ascribed exclusively to the intrinsic characteristics of the optimisation methods, such as convergence properties, sensitivity to initial conditions, and computational efficiency, rather than to structural discrepancies in the problem formulation.

3.4.1 Objective function for CCGT case study

An accurate representation of the CCGT is essential to reliably describe its real operating behaviour within the dispatch optimisation framework. The electrical power output and overall efficiency of the unit are primarily influenced by two key variables: the degree of opening of the Inlet Guide Vanes (IGV), which regulate the gas turbine load by controlling the air mass flow rate, and the inlet air temperature, which exerts a significant influence on thermodynamic performance. To maintain simplicity in the comparison of algorithms, the operating condition is expressed in terms of CCGT load. This is defined as the ratio of the actual power output to the maximum power achievable at the corresponding ambient temperature. This normalised representation facilitates the integration of performance characteristics into the optimisation model.

The relationships delineating power output and efficiency as functions of load are derived through second-order polynomial regressions based on results from a detailed GateCycle thermodynamic simulation model. The reference model represents a 400 MW Ansaldo Energia F-class gas turbine (V94.3A) operating in a combined-cycle configuration. The GateCycle model has undergone rigorous validation to ensure its alignment with real plant performance data, thereby ensuring the preservation of the essential nonlinear behaviour of the CCGT while facilitating the implementation within the optimisation framework. With regard to the nominal data, a power Pnom of 400 MW and an efficiency ηnom of 55% were assumed (referring to 100% load and a turbine air inlet temperature T of 15°C). The Minimum Environmental Load (MEL) has been set at 45%. A further reduction in the IGV would result in carbon monoxide CO concentrations at the stack exceeding the Emission Limit Value (ELV) [36].

The combined cycle model was employed to quantify the Operational Profits (OP) associated with generator dispatch, as formalised in Eq. 3.6, which constitutes the objective function of the optimisation problem. In this study, the operational profit at each time step t is defined as the difference between revenues obtained from electricity sales and total operating costs incurred. The costs encompass both the initial establishment of the power plant, which is calculated to include fuel consumption and the thermal stress associated with unit ignition, and the Cost of Electricity (COE). Zonal Price (ZP) is the Day-Ahead price for the specific market

$$\mathrm{obj_{CCGT}} = \sum_{t=1}^{T} \mathrm{OP_{CCGT_t}} = \sum_{t=1}^{T} (\mathrm{ZP_t} - \mathrm{COE_t}) \cdot \mathrm{P_{act_t}} \cdot \Delta t - \mathrm{C_{SU_t}} \tag{3.6}$$

The COE is defined as the specific production cost, expressed in €/MWh, required to generate one unit of electrical energy, Eq. 3.7. The COE consists of three main components. The initial term is responsible for the calculation of fuel expenditure, and is determined by the ratio between the electrical energy generated and the cycle efficiency. This ratio is used to establish the necessary fuel input. The second term signifies the financial burden associated with CO2 emissions, which is proportional to the quantity of gas consumed. The third term captures the costs associated with variable O&M, which are hypothesised to be proportional to the energy produced. The operation of a gas turbine entails progressive component degradation, ultimately requiring scheduled maintenance outages that represent a significant economic burden from the plant owner's perspective. In particular, the cost associated with a Hot Gas Path Inspection (HGPI) is assumed in this case study to be €31.5 million [37,38].

$$\mathrm{COE_t} = \frac{\mathrm{C_{Gas_t}} + \mathrm{e} \cdot \mathrm{C_{CO2}}}{\eta_{\text{™}_t}(\mathrm{T_t}, \mathrm{x_t})} + \mathrm{C_{O\&M}} \tag{3.7}$$

The objective function is defined as the real economic margin of plant operation, which is calculated by subtracting start-up costs, as defined in Eq. 3.8, and generation costs from market revenues. The optimisation algorithm should be able to determine whether and when dispatching the CCGT is economically advantageous under given market conditions.

$$C_{SU_t} = \cdot Gas_{SU_t}(ST_t) \cdot \left(C_{Gas_t} + C_{CO_2} \cdot e\right) - E_{SU_t}(ST_t) \cdot \frac{\sum_t^{t-Hours_{SU}(ST_t)} ZP_t}{Hours_{SU}(ST_t)} + C_{O\&M} \cdot EOH_{SU} \cdot (ST_t) \cdot \mathrm{P_{nom}} \quad 3.8$$

All model parameters are defined on an hourly basis (Δt = 1 h), consistent with the time resolution of the electricity market under consideration. The variable t_t denotes time, T_t the ambient temperature and ZP_t the zonal price at which electricity sales bids are remunerated in the Italian day-ahead wholesale market analysed in this study.

The gas price is assumed to be equivalent to the daily closing price observed on the spot market [39,40]. The emission factor, e, which represents the CO_2 emissions per unit of fuel burned, has been set at 0.2013 kg_{CO_2}/kWh_{gas} [41]. The carbon allowance cost was assumed as the annual average price of the EU Emissions Trading System (EU-ETS) [42]. In conclusion, the hourly ambient temperature T_t is derived from historical datasets [43], as it exerts a direct influence on the achievable power output and efficiency of the combined cycle.

3.4.2 Objective function for BES case study

The electrochemical storage system has been modelled using a simplified yet representative approach, which captures its essential operational characteristics, namely its energy capacity and maximum current rate. The total storage capacity, E_{max}, is set to 10 MWh, while the maximum *C-rate* is limited to 0.2C, corresponding to a maximum charge and discharge power, P_{max}, of 2 MW. This constraint guarantees that a full charge or discharge cycle necessitates a minimum of five hours. Furthermore, the battery is constrained to retain a minimum state of charge of 20%, thereby limiting the maximum Depth of Discharge (DoD_{max}) to 80%. This is done in order to preserve the service life of the battery and to prevent excessive cycling costs. The DoD limit is a critical factor in this analysis, as it is used to calculate the total number of cycles over the battery's lifespan. This is assumed to be 7,500 cycles [44]. The round-trip efficiency (RTE) is calculated from both the charge and discharge efficiencies, each set at 90%, resulting in an overall RTE of 0.81.

The maintenance and investment model assumes the battery is replaced at the end of its operational life, once the maximum cycle count is reached. A specific investment cost of €100/kWh is adopted for a large-scale battery, corresponding to a total capital expenditure CAPEX of 1 M€[45,46]. This indicates a cost of 133.3 € per complete charge-discharge cycle, or €8.3/MWh for energy either extracted from or introduced into the grid.

In the context of dispatch optimisation, the battery's SoC is identified as the pivotal decision variable. Eq. 3.10 and Eq. 3.11 provide a model for the costs and revenues associated with battery operation. An increasing SoC_t indicates charging, as the battery consumes electricity from the grid at the Single National Electricity Price (PUN). Conversely, a decreasing SoC_t indicates discharge, with energy sold to the grid at the zonal price, effectively operating as a generator. It is imperative to note that an operational constraint exists that prevents simultaneous charging and discharging. This constraint is fundamental in preserving physical realism within the operational dispatch model. In both costs and revenues, the cost per cycle is evident, accounting for the fraction of the cycle corresponding to the difference between SoC_t and SoC_{t-1}. This dispatching formula is predicated on the maintenance model, as it ensures that the batteries' CAPEX is allocated over the entire operating period.

$$\mathrm{obj_{BES}} = \sum_{t=1}^{T} \mathrm{OP_{BES_t}} = \sum_{t=1}^{T} \left(\mathrm{Revenue_{Disch_t}} - \mathrm{C_{Ch_t}}\right) \tag{3.9}$$

$$Revenue_{\,Disch_t}(ZP_t) = |SoC_t - SoC_{t-1}| \cdot E_{max} \cdot \left(ZP_t \cdot \eta_{disch} - \frac{C_{cycle}}{2 \cdot DoD_{max} \cdot E_{max}}\right) \tag{3.10}$$

$$C_{Ch_t}(PUN_t) = (SoC_t - SoC_{t-1}) \cdot E_{max} \cdot \left(\frac{PUN_t}{\eta_{ch}} + \frac{C_{cycle}}{2 \cdot DoD_{max} \cdot E_{max}}\right) \tag{3.11}$$

3.4.3 The impact of the initial solution on the optimum

The pattern-search process, along with the various algorithms implemented by the *fmincon* in MATLAB, which are part of nonlinear modelling, requires an initial solution, designated x_0, on which to initiate the optimisation process [10,47,48]. It was observed that the value of x_0 significantly affects the optimal value found. To ensure a fair comparison of algorithms for the same type of optimised problem, under their optimal operating conditions, it is imperative to conduct a thorough analysis to determine the most suitable criteria for setting x_0. A common objective function has been defined for both linear models based on MILP and non-linear models, ensuring the consistency of the two approaches. To facilitate comparison across different resolution models, two simple case studies have been defined. The first of these involves CCGT dispatching, whilst the second concerns BES system arbitrage; the objective functions are defined in Eq. 3.6 and Eq. 3.11.

As illustrated in Figure 3.1 and Figure 3.2, the findings of this investigation are reported for CCGT and BES, respectively. The investigation spans two months, during which the energy market experiences contrasting scenarios. In the spring of 2020, which was characterised by the generation of VRE and a consequent extremely low demand for electricity due to the effects of the pandemic caused by the novel severe acute respiratory syndrome (SARS-CoV-2) (Figure 3.1 (a) and Figure 3.2 (a)), the month of May was notable for its low demand for electricity. It is evident from Figure 3.1 (b) and Figure 3.2 (b) that August 2022 was the month when energy prices reached their peak during the ongoing energy crisis.

Two divergent strategies can be adopted. The first of these is to provide a random, yet feasible x_0 that satisfies all imposed constraints, for each algorithm. The experiment involved the generation of 25 instances and the execution of an equal number of dispatch optimisations, implemented through the utilisation of these four distinct algorithms. The second approach necessitates the constant setting of x_0 for all hours. In the case of the CCGT, four constant x_0 are considered. The initial correspondence is attributed to the power plant being deactivated, or functioning at a medium load (72.5%) or at maximum capacity. In relation to the BES, the constant x_0 is generated as four quasi-constant SoC (20%, i.e. the minimum SoC, two intermediate SoC, 40% and 80%, and finally the full charge status of 100%). The definition of x_0 as quasi-constant is that during the initial hours of charging or discharging, the imposed constant value is reached from the initial state.

As illustrated in Figure 3.1, the impact of varying x_0 on the achieved optimum for CCGT, as defined by Eq. 3.6, is demonstrated. The optimal distribution, as ascertained by the utilisation of random initial solutions, is illustrated by boxplots. Conversely, red markers denote the optimal distribution as determined by the imposition of an always-off initial solution. Green markers signify the Minimum Environmental Load (MEL), while blue markers denote intermediate load, and light blue indicates full load x_0.

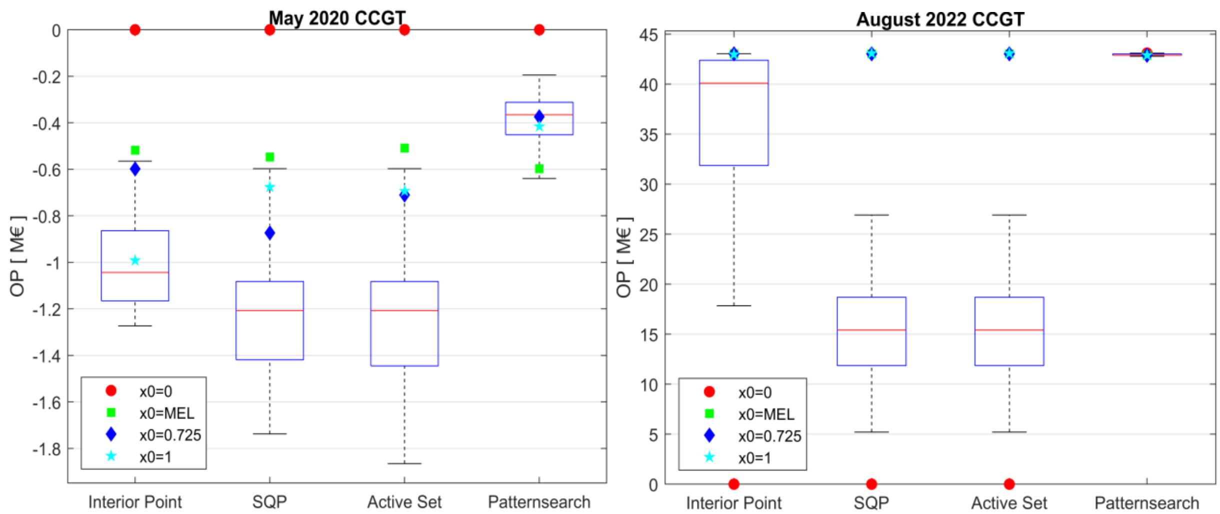

(a) (b)

Figure 3.1: Initial solution impact on the CCGT dispatch optimisation [49]

Firstly, it can be observed that SQP and Active Set algorithms function significantly more effectively with constant x_0; the optimum found is considerably higher than for random x_0. It is also interesting to note that often, for an x_0 constant equal to 0, both algorithms give an optimum equal to zero. This means that, in this non-favourable condition (i.e., May 2020), the best-identified dispatch by these algorithms is to maintain the power plant off. It is important to note that the considerations for interior point and pattern search are similar, even though the differences in the identified optimum are less significant.

Nevertheless, the most salient issue is to emphasise the repercussions of the prevailing market scenario. In market scenarios where the decision is made to operate the power plant (as was the case in August 2022), the optimal point is identified by the x_0 value corresponding to a constant full load. Conversely, during periods of non-profitability (such as May 2020), the most prudent course of action would be to initiate the optimiser with x_0 equal to 0. Failure to do so would result in operational inefficiencies, leading to economic losses. It has been demonstrated that, in general, the optimisers are incapable of deactivating the CCGT in May 2020, thereby minimising the loss if a non-zero initial condition has been established. However, the implementation of a zero initial condition has the potential to render all algorithms ineffective, even in a profitable state, for instance, in August 2022. In the final case, it is demonstrated that Patternsearch is the only method capable of converging to the optimum under every initial condition, thus resulting in a robust solution for the generator case. Consequently, for CCGTs, the following criterion is adopted to set the algorithm's initial solution on the basis of the average Clean Spark Spread (CSS) on the optimisation period, as defined by Eq. 3.12. CSS represents the profitability margin for generating and selling electricity for a CCGT. If CSS is higher than zero, the initial solution is set at full load; zero otherwise.

$$\overline{CSS} = \frac{\sum_{t=1}^{SW} CSS_t}{SW} = \frac{\sum_{t=1}^{SW} PZ_t - COE_t}{SW} \tag{3.12}$$

Figure 3.2 reports the analysis conducted to assess the impact of the initial solution on the optimum found of the BES system, in different market scenarios.

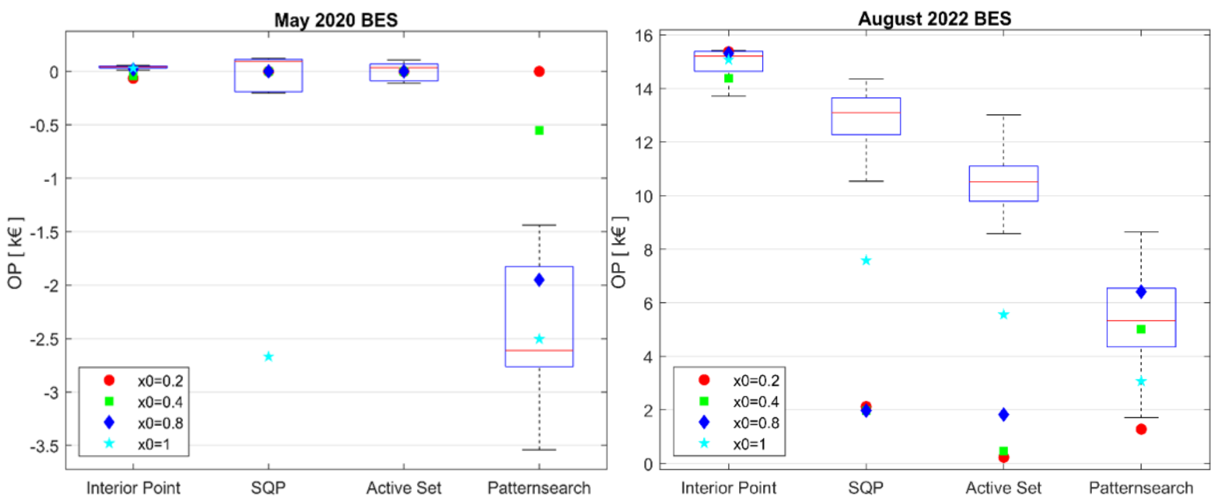

(a) (b)

Figure 3.2: Initial solution impact on the BES dispatch optimisation [49]

In contrast, the Interior Point algorithm demonstrates significantly lower sensitivity to the choice of initial solution. The discrepancy between random and constant approaches is substantially reduced, indicating greater robustness of the solver. In low-price conditions (Figure 3.2 (a)), where daily variability is limited, a random initialisation performs marginally better. However, as both price levels and volatility increase, a constant may offer certain advantages. Following a thorough evaluation, it has been determined that the Interior Point method is the most stable algorithm with respect to the initial solution settings.

With regard to the Patternsearch algorithm, its performance indicators are generally lower compared to the other three optimisation methods, as will be further discussed in the subsequent section. With regard to the selection of the initial solution, in low-price scenarios with limited variability (Figure 3.2 (a)), the only configuration capable of identifying the standstill solution consists of setting x_0 equal to the minimum admissible SoC. However, this choice becomes less than optimal in periods of rising prices and market volatility. In such cases, it is challenging to ascertain the initial value that will yield optimal performance. Consequently, random initialisation emerges as a rational and pragmatic approach. To summarise, when defining an initial solution for BES optimisation, a randomly generated x_0 that complies with operational constraints, such as the initial SoC at t=0 and the maximum allowable C-rate, represents the most effective choice for SQP and Active Set methods. The same approach is adopted for the Interior Point algorithm due to its limited sensitivity to initialisation. However, for the Patternsearch algorithm, the x0 is assigned, as per the condition reported in Eq. 3.13.

$$x_0 = \begin{cases} 1 - DoD_{max}, & \eta_{disch} \cdot \max(PZ) - \dfrac{\min(PUN)}{\eta_{ch}} < C_{cycle} \cdot C_{rate_{max}} \\ random, & otherwise \end{cases} \quad 3.13$$

This analysis was essential for comparing different types of solvers under optimal conditions in the next section 3.4.4. It is evident that generalising the choice of initial conditions is challenging, and this reduces the robustness of the solution defined, as it is highly subject to variation.

3.4.4 The impact of the problem size on the optimum

The subsequent section will evaluate the impact of the complexity of the problem. Complexity is measured in terms of the number of hours that are optimised simultaneously. The varied parameter is the Simulation Window (SW). For a more in-depth discussion of this parameter, please refer to Section 4.2.2. The optimisation assessment is carried out on the basis of the following Key Performance Indicators (KPIs).

The optimum identified value of the objective function (i.e. operational profits including O&M) is, of course, the main indicator. Secondly, the optimisation time is considered, and finally, the variability of these two parameters is taken into account to account for the robustness of solver performance.

The variation in the identified optimum is attributable to the stochastic components inherent in the optimisation process. Stochasticity can arise from x_0 when it is set randomly (in accordance with the criteria defined in Section 3.4.3) or from the process itself, as observed in surrogate optimisation or genetic algorithms. The same stochasticity may result in variability in the time taken to optimise, being added to minor fluctuations in computer performance. In the following sections, variability values of both the identified optimum and optimisation time are assumed as the range between the 10th and 90th percentiles. The following section will present an algorithm comparison performed across a range of market scenarios. Despite the presence of distinct operational behaviours observed during periods of low and high prices, the merit order of the algorithms remains unaltered. For the sake of synthesis, the focus is restricted to the two previously analysed months, which represent extreme market conditions. The trends observed under these opposite scenarios confirm the results discussed in Section 3.4.3, allowing for their generalisation. In order to evaluate the impact of the Simulation Window (SW) width, three configurations, 24 h, 36 h, and 48 h, are tested for each algorithm. Furthermore, in order to assess performance variability, ten optimisation runs are executed for every combination of algorithm and software.

Figure 3.3 and Figure 3.4 present the optimisation time (in seconds) on the x-axis using a logarithmic scale, with the intention of accentuating the disparities in performance. Meanwhile, the y-axis (linear scale) reports the identified optimal operational profits (OP), with the exclusion of fixed O&M costs, which remain constant across various algorithms. The utilisation of solid markers (circle for SW = 24 h, square for 36 h, and rhombus for 48 h) serves to denote average values, whilst error bars are employed to illustrate variability.

Figure 3.3 presents a comparison of the CCGT dispatch optimisation in May 2020 and August 2022 (see Figure 3.3 (a) and Figure 3.3 (b), respectively). MILP, Active-Set, SQP, and Interior Point emerge as the most competitive algorithms in terms of computational efficiency, with the capability to solve the one-month problem in less than one second. Among the aforementioned methods, MILP attains the optimal objective values, while SQP, Interior Point, and Active-Set yield results that are marginally lower but comparable. During periods of low prices (Figure 3.3 (a)), a limited number of time intervals are economically viable for operation. The MILP successfully identifies these profitable windows, operating the CCGT selectively and keeping it offline otherwise. Conversely, the remaining fast algorithms converge to the always-switched-off configuration, corresponding to zero operational profit, which coincides with the initial solution defined in Section 3.4.3. In periods where prices are high (see Figure 3.3 (b)), the performance discrepancy is reduced, with Interior Point displaying only a slight variation in comparison to the other fast solvers.

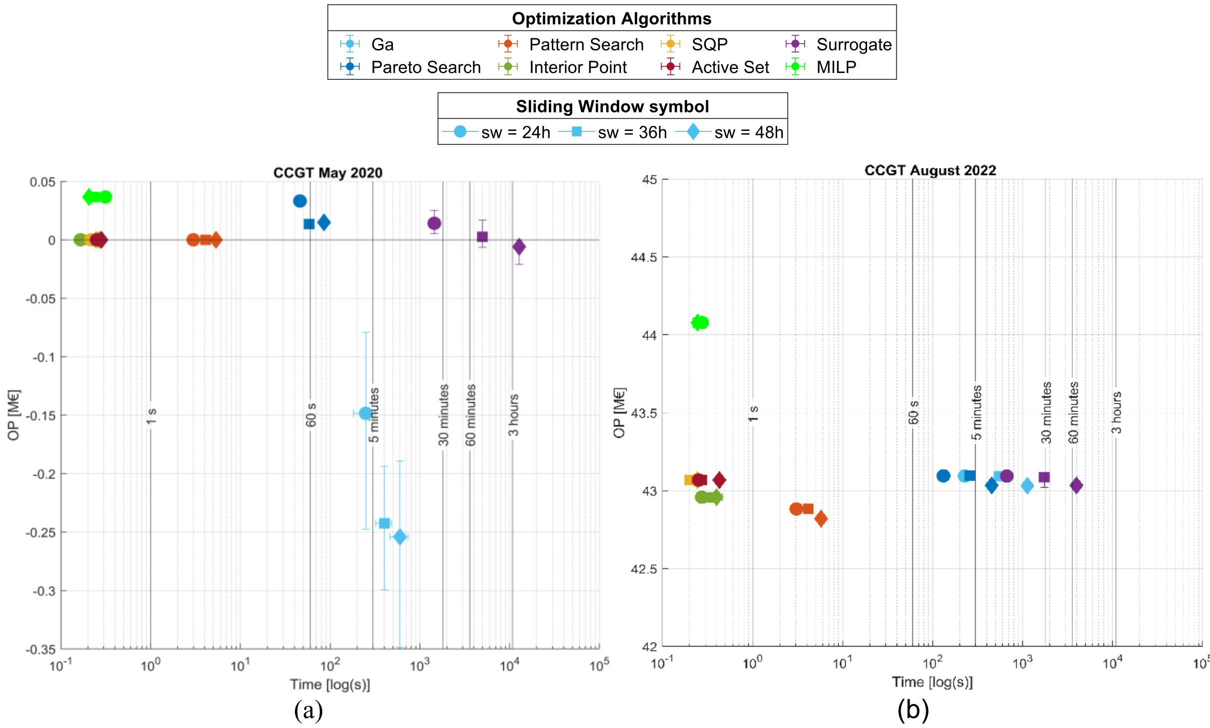

Figure 3.3: Simulation Window (SW) impact on the CCGT optimum schedule [49].

It is important to note that, to accommodate extended computation times, Patternsearch can take several seconds, whereas Paretosearch and Genetic Algorithms (GA) can take on the order of minutes. It is important to note that surrogate optimisation can take up to 3 hours, particularly when larger SW values are used. In terms of optimality, Paretosearch remains competitive in low-price scenarios, while in high-price scenarios, all heuristic methods identify solutions approximately 2.3% lower than those obtained with MILP. It is evident that, overall, MILP demonstrates consistent superiority in performance compared to the available alternatives. Notably, variability is evident only in the context of GA and Surrogate optimisation, a phenomenon indicative of their inherently stochastic nature. As demonstrated in Figure 3.3 (a) and Figure 3.3 (b), there appears to be no discernible advantage to be gained from increasing the SW width. This is because May 2020 is characterised by persistently low prices and August 2022 by persistently high prices; consequently, extending the time horizon does not enable advantageous coupling across consecutive days of operation. This phenomenon is examined in greater detail in Section 4.2.2. With the exception of MILP, increasing the width of the search space (and consequently the number of decision variables) generally degrades performance due to increased problem complexity.

Figure 3.4 presents an analogous comparison for the BES dispatch optimisation. In this instance, MILP has been demonstrated to exhibit superior performance with regard to optimality and computational time. The BES problem manifests itself as being significantly more complex for a considerable number of algorithms, which frequently fail to identify feasible solutions that outperform the standstill option. This results in potential arbitrage opportunities being missed. It is noteworthy that MILP is the sole method capable of solving the one-month BES dispatch problem in less than one second.

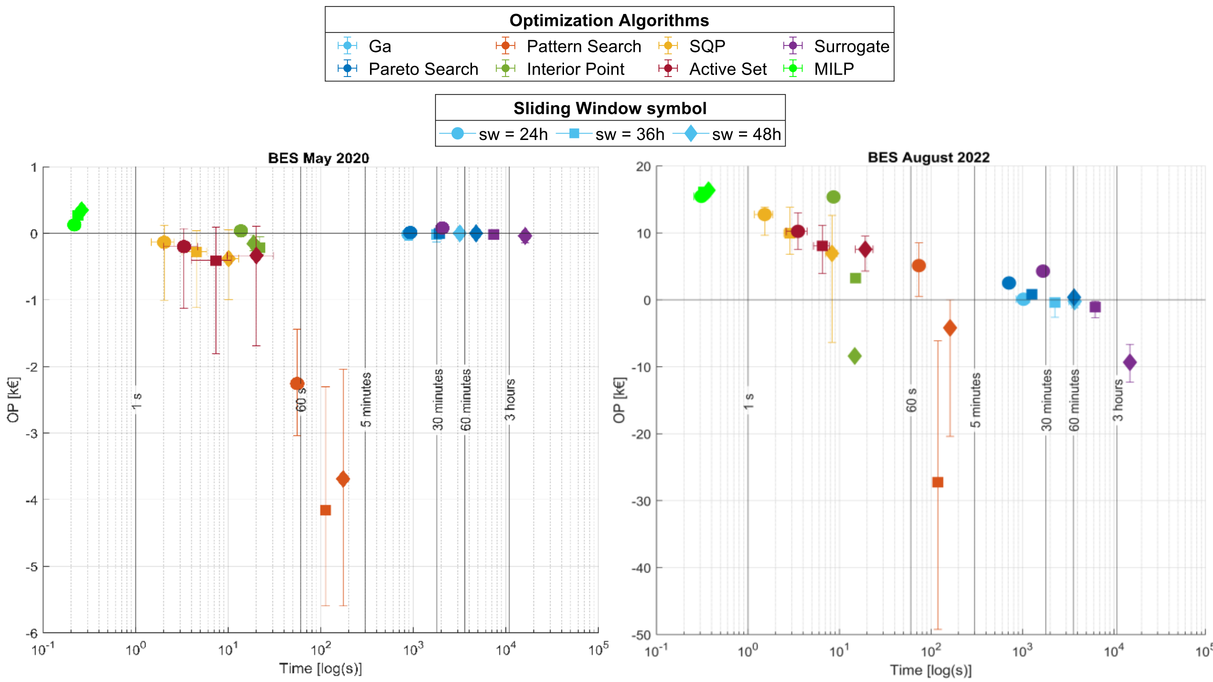

(a) (b)

Figure 3.4: Simulation Window (SW) impact on the BES optimum schedule [49].

In contrast to the CCGT case, Figure 3.4 demonstrates that increasing the SW width results in elevated levels of identified profits. The transition from a 24-hour to a 36-hour timeframe has been observed to result in a substantial increase in profit, with a 108% growth recorded in May 2020 and a 4.2% increase in August 2022. In absolute terms, these figures correspond to gains of €138 and €649, respectively. A more detailed interpretation of this effect is provided in Section 4.2.2.

The Mixed Integer Linear Programming (MILP) formulation has been selected as the best modelling solution, on the basis that it provides the optimal balance between modelling accuracy, computational efficiency, and solution robustness for the class of dispatch problems under consideration. The operational scheduling of CCGT units and Battery Energy Storage Systems inherently involves both continuous variables (e.g. power output, state of charge) and discrete decisions (e.g. unit commitment, on/off status, charge/discharge logic), which naturally lead to a mixed-integer structure. Concurrently, the technical constraints and cost functions of the system can be expressed with linear relationships or linear approximations without significant loss of accuracy. In Section 4.2, the technique to handle non-linearities of the objective function is presented and discussed. In such circumstances, MILP ensures global optimality for convex linear problems and benefits from highly mature and efficient commercial solvers capable of handling large-scale instances within very short computation times.

In comparison with nonlinear programming (NLP) approaches, MILP reduce the risk of convergence to a local optimum and does not necessitate gradient continuity, thereby enhancing its robustness. In contrast to metaheuristic or stochastic methods (e.g., genetic algorithms, surrogate optimisation), MILP does not rely on random search mechanisms, thereby ensuring repeatability of results and significantly lower variability in both objective value and computation time. Furthermore, the efficacy of MILP is enhanced by its ability to scale effectively with increasing time horizons, such as wider SW, thereby ensuring the maintenance of solution quality in scenarios where approaches may encounter challenges due to the proliferation of decision variables. For these reasons, the MILP framework is considered the most reliable and computationally efficient solution to the deterministic dispatch optimisation problems analysed in this work. This analysis proved instrumental in determining the most appropriate mathematical model for developing a Tool capable of adapting to different energy system layouts. The subsequent Section MEDO Tool is dedicated to the presentation of the tool that has been developed for the purpose of managing a variety of demand, market and hybrid-driven problems. The tool developed has the advantage of being able to adapt to different types of problems while maintaining a robust mathematical structure.

Chapter 4

MEDO Tool

The objective of this chapter is to present the Multi Energy Dispatch Optimiser (MEDO) tool that was developed during the PhD. The tool aims to provide a solid basis for the techno-economic analysis of different engineering solutions. For this reason, the structure has been designed to be modular, to ensure energy and mass balances are respected. This approach ensures the tool's high versatility and adaptability to diverse evaluation requirements. MEDO is based on Mixed Integer Linear Programming (MILP), which has previously been shown to be best suited to the purpose of dispatching problems, with the introduction of linearization techniques to manage the complex physical aspects of each technology.

4.1 Domain of application

There are three main categories of energy management problems: demand-driven, market-driven, and hybrid-driven approaches. Each approach uses distinct objective functions and constraints to manage energy resources, such as microgrids, multi-energy systems (MES), and energy storage. This categorisation is very useful to generalise various operational problems in the field of engineering. Problems in the naval sector or on remote islands often fall into the first category, Demand Driven. In such cases, the objective is to define the operating profile of generators to minimise generation costs. In the following subsections, the three types of problems are presented and discussed. The developed MEDO tool is capable of managing different types of energy sources (electrical, thermal) or managing different fluids such as hydrogen, water, natural gas, etc. For the sake of clarity, the energy layout in the following subsections has been simplified and does not show interconnections between buses. However, the tool can easily manage different interconnected buses with Net Transmission Capacities (NTC) limits. Before the characterisation of specific components, three techniques for managing the nonlinearity and complexity of the dispatching optimisation problem are presented and discussed.

4.1.1 Demand-driven problems (Production Cost Minimisation)

In demand-driven energy management, the primary goal of the optimisation software is to satisfy a specific energy demand at the minimum possible operational cost [50,51]. Figure 4.1 reports an energy system layout for the demand-driven problems. The following energy system layout is composed of an internal combustion engine and a gas turbine as electric generators, converting chemical fuel energy, from which it’s also possible to recover thermal energy from exhaust gases through the process of thermal energy recovery. The electrical storage is essential to manage the peak shaving, which serves to minimise the operating cost of the energy system by shifting periods of overproduction from VRE technologies.

The demand-driven problem objective is designed to minimise the sum of startup costs, minimum load costs and variable fuel costs for generators. In more complex multi-energy systems, this also includes the cost of fuel and electricity inputs from the grid. This can be applied to an island scenario where, beyond the demand requirements, there are also grid stability requirements that have to be matched [52]. For instance, a security-constrained unit commitment model aims to find a schedule that minimises costs while ensuring system security and meeting network flow. Generally, for the naval application, the objective of onboard energy management in maritime vessels is to optimise the use of available energy resources in order to improve overall efficiency, reduce fuel consumption, and enhance economic performance while maintaining operational reliability [53]. In this context, energy management seeks to dynamically coordinate power generation, thermal flows, and waste heat recovery technologies to match the vessel’s variable mechanical, electrical, heating, and cooling demands throughout the voyage. The energy production system must satisfy hourly variable load demands (electricity, heat, cooling) during the entire operation period, to ensure the internal security requirements [54].

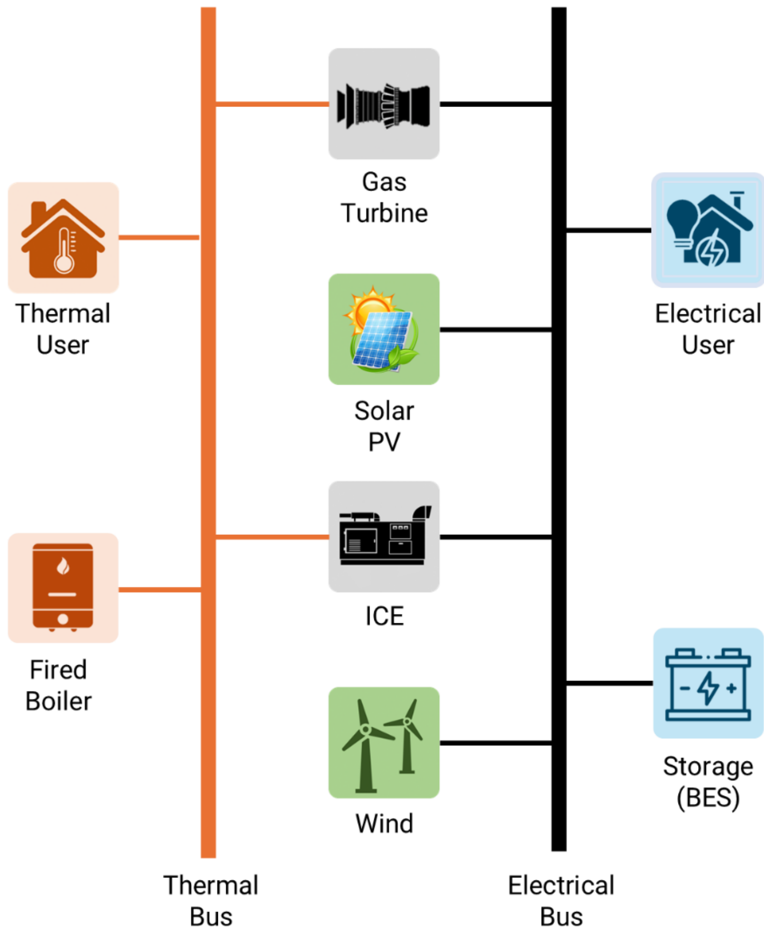

Figure 4.1: Demand-driven energy system configuration.

4.1.2 Market-driven problems

Market-driven problems are characterised by the prioritisation of optimising the economic returns of energy system operations, typically within the context of wholesale or real-time markets [55]. These types of problems are of particular interest to the power plant managers. In the context of traditional generators, optimisation assumes paramount importance. The neglect of certain costs, such as maintenance expenses, can result in a substantial diminution of revenues [49]. Consequently, for conventional generators, the primary challenge lies in accurately incorporating all operational expenses related to the system's functioning. For CCGT, the main issues are linked with the start-up and shut-down costs that include both gas consumption and maintenance costs [56]. The spark-spread ratio may inform operational decisions, the difference between the market price of electricity and the variable cost of producing it, to ensure profit-oriented dispatch for traditional generators. In the context of storage systems, such as lithium-ion batteries or compressed air storage with a post burner during the discharging process [57] it is imperative to consider not only operating costs but also to identify market opportunities, given their correlation with daily spreads and the electricity price profile. Storage devices are optimised to maximise arbitrage profits by acquiring and storing electricity when prices are low (off-peak) and subsequently selling it back to the grid when prices are high (on-peak).

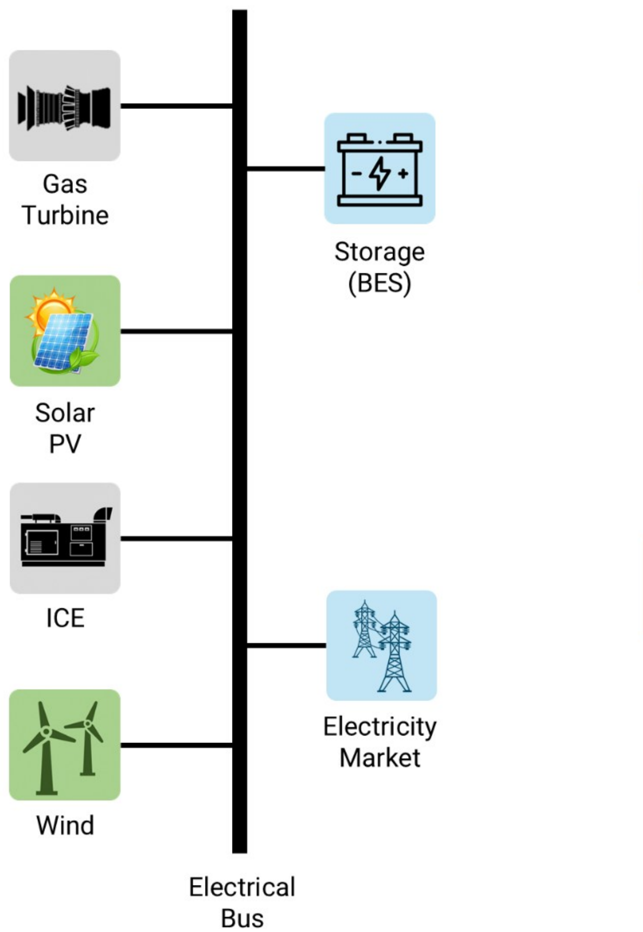

Figure 4.2: Market-driven energy system configuration.

As illustrated in Figure 4.2, the system comprises programmable generators, VRE generators, and a storage facility. In such cases, the optimisation algorithm endeavours to identify the optimal operating profile, to enhance revenues associated with the system's operation, whilst adhering to the technical constraints imposed by each system. In a multitude of scenarios, the network connection constraint assumes paramount importance, as it signifies the transmission limit that generators are capable of achieving towards the network. This is a pivotal aspect in interconnected networks, where the objective is to avert congestion at network points and subsequent overload.

4.1.3 Hybrid-driven problems

Problems with hybrid-driven energy management are caused by the need to simultaneously satisfy internal energy demand and increase system profitability by taking advantage of external market opportunities [50,52]. Hybrid optimisation frameworks differ from traditional approaches in that they seek to balance cost minimisation and revenue maximisation within a unified operational strategy. In practice, the EMS must ensure the reliable supply of local energy needs, such as electricity, heating and cooling. It must do this while responding quickly to market signals, including time-varying tariffs, day-ahead prices and flexibility incentives. This creates a continuous trade-off between using locally generated energy for self-consumption to reduce operating costs and exporting or strategically scheduling resources to capture economic value from the market.

Such problems are typically formulated as multi-objective optimisation models, often based on Mixed Integer Linear Programming (MILP), where internal system operation and external economic interaction are explicitly coupled. In small grids and microgrids with auto-generation profiles, this approach enables coordinated scheduling of distributed assets such as batteries, CHP units, and renewable sources. This allows the system to shift energy across time and energy vectors in response to both technical constraints and economic signals. As discussed in the context of multi-energy systems, hybrid optimisation enhances financial performance by aligning operational decisions with market conditions without compromising local reliability [50].

Furthermore, hybrid EMS frameworks underpin aggregation paradigms such as Virtual Power Plants, where distributed resources are coordinated to meet internal demand efficiently while collectively participating in electricity markets. This is particularly relevant in renewable-rich systems, where local generation is prioritised to serve flexible demand and external market exchanges are used strategically when internal resources are insufficient. In essence, hybrid-driven optimisation shifts the focus of energy management from purely operational efficiency to value-oriented system coordination. This enables decentralised energy systems to minimise costs, unlock new revenue streams and improve overall resilience.

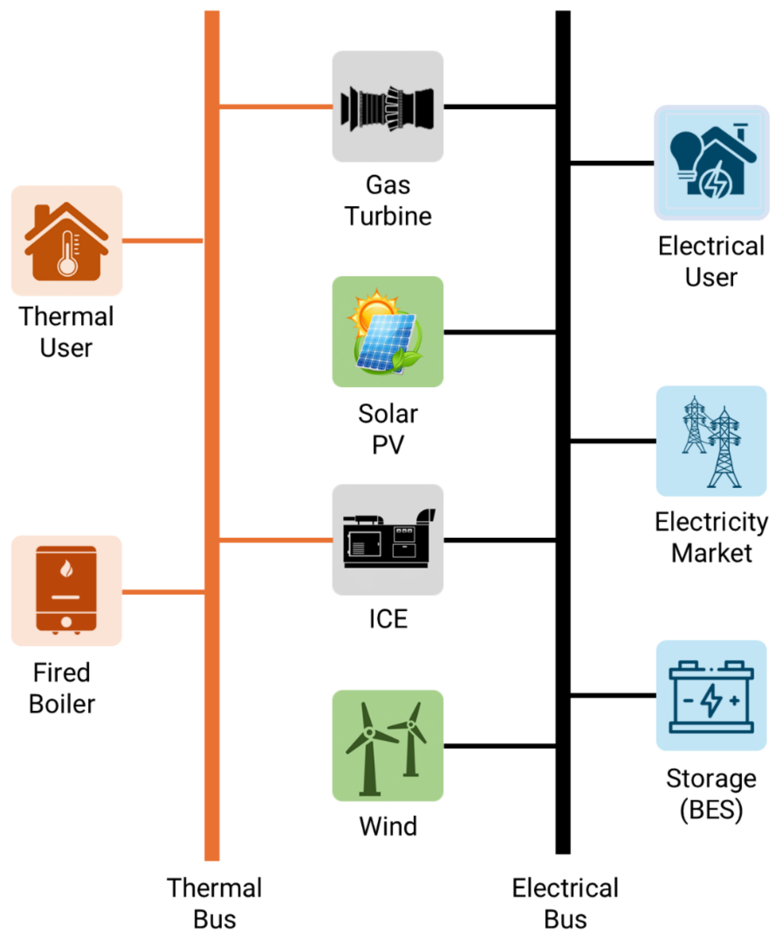

Figure 4.3: Hybrid-driven energy system configuration

4.2 Deployed optimisation techniques

In the following chapter, the objective is to present the three fundamental methodologies that were applied during the development of MEDO. Firstly, the complexity associated with the nonlinear behaviour of the characteristic curves of the technologies was handled using piecewise linearization and Big-M. Secondly, the complexity associated with the time dimension was addressed, thought the Rolling Horizon technique.

4.2.1 Piecewise Linearisation (PWL)

Piecewise linearisation is a standard technique used to approximate non-linear functions within Mixed Integer Linear Programming (MILP) models [58,59]. The fundamental concept underpinning this approach involves the substitution of a non-linear function with a series of linear segments, delineated over a designated set of breakpoints within its domain. In the context of univariate functions, the domain is segmented into intervals, and the function is estimated through linear interpolation between consecutive breakpoints using convex combinations. This approach can be extended to functions of two variables by discretising both dimensions and approximating the function over a grid of sampled points. The one-dimensional approach involves the application of linear interpolation along one axis while discretising the other. The triangle method, which involves the partitioning of each rectangular cell of the grid into two triangles and the performance of interpolation using convex combinations of the triangle vertices. The rectangle method improves the one-dimensional approach by introducing a correction term along the second dimension. These formulations can be embedded into MILP models by introducing continuous variables for convex combinations and binary variables to ensure that only the appropriate breakpoints are active. Piecewise linearisation facilitates the efficient handling of non-linear relationships by MILP solvers, thereby offering a practical trade-off between model accuracy and computational tractability. As illustrated in Figure 4.4, the performance curve of an ICE engine is displayed, along with the linearisation process. It is imperative to acknowledge that the variable linearised as a function of power does not denote efficiency but rather fuel consumption, as demonstrated in Figure 4.5. For illustration, two linearisation solutions are hereby proposed. The first of these has a single linear section, with a mean absolute percentage error (MAPE) of 0.95% and MAE of 1.1 kg. This solution already provides a satisfactory degree of linearisation approximation. Increasing the number of discretised sections to 4 (purple line in Figure 4.4) results in a mean absolute percentage error (MAPE) of 0.06% and a mean absolute error (MAE) of 0.074 kg. The number of optimised segments must always be evaluated based on the MAPE error that is acceptable for the approximation during the optimisation phase. The linearised variable is not the efficiency, but rather the fuel consumption reported in Figure 4.5. In the optimisation phase, the objective is to minimise the fuel cost as a function of the power output. The subsequent figures have been employed exclusively for the purpose of illustrating the general approach of the linearisation methodology. This process can be employed for a variety of conditions, e.g., a non-linear start-up cost contingent on the initial conditions.

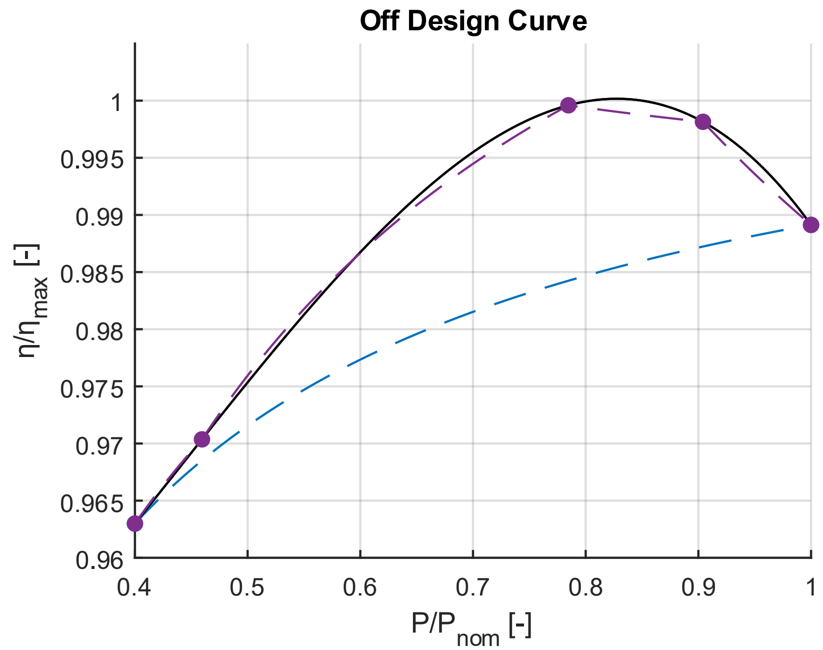

Figure 4.4: Internal Combustion Engine (ICE) off-design performance curve [60].

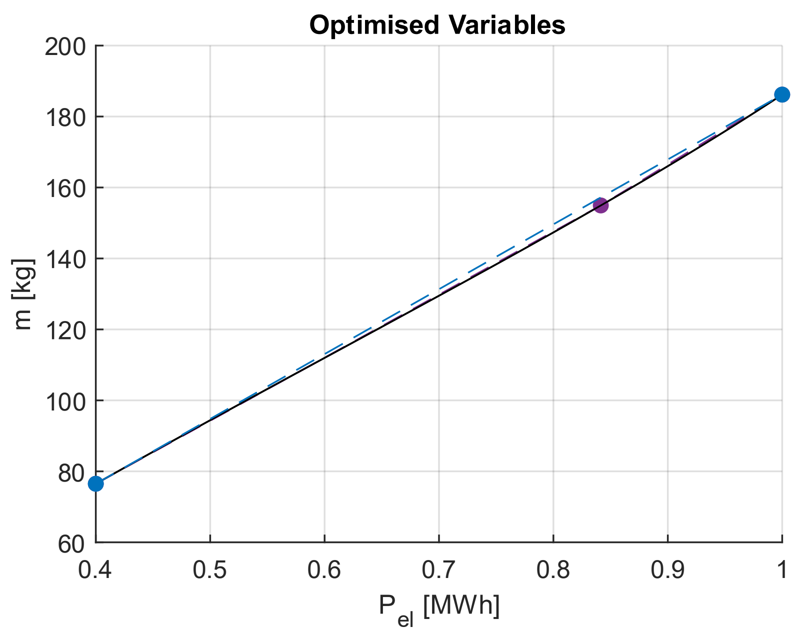

Figure 4.5: Fuel consumption as a function of the generated energy by the ICE [60].

Equations 4.1-4.6 are essential to describe the linearisation process for non-linear MILP problems. The utilisation of binary variables is imperative to ensure the physical consistency of the system.

In all formulas, the index *i* is representative of the linearised segment, while h is utilised to denote the time dimension. Equation 4.1 is utilised to delineate the limits of the linearised segments for the optimised variable. It is imperative to note that the values x_{min} and x_{max} represent the limits of the linear segments, which are independent of time. In contrast, the variable *onoff* has the same physical dimension as the optimised variable, since consistency must be guaranteed at every optimised time instant. Equation 4.2 formally represents the dependent variable as a function of the optimised variable, ensuring the accuracy of the limits, i.e. x_{min} and x_{max}, of the linearised segments and adherence to the actual relationship between the variables.

$$x_{min}(i) \cdot onoff(h,i) \leq x_{opt}(h,i) \leq x_{max}(i) \cdot onoff(h,i) \qquad 4.1$$

$$y = f(x), \qquad to\ calulate\ y_{max}\ and\ y_{min} \qquad 4.2$$

The linearisation coefficients are calculated using Eqs. 4.3-4.4. Equation 4.3 is utilised for the calculation of the angular coefficient of the linearised segment, whereas Eq. 4.4 is employed for the calculation of the entire linearised segment.

$$\alpha(i) = \frac{y_{max}(i) - y_{min}(i)}{x_{max}(i) - x_{min}(i)} \qquad 4.3$$

$$\beta(i) = y_{max}(i) - \alpha(i) \cdot x_{max}(i) \qquad 4.4$$

Equations 4.5 and 4.6 represent the constraints that must be incorporated into the MILP model to deploy piecewise linearisation. Equation 4.5 delineates the correlation between the optimised variables. It is important to note that the intercept is multiplied by the binary variable, *onoff*, thereby cancelling out the constant contribution of the linearised segment that was not selected at that particular time interval. Equation 4.6 is pivotal in guaranteeing physical consistency by constraining the system's operation to a particular time frame to an operating mode described by the linearised segment.

$$y_{opt}(h,i) = \alpha(i) \cdot x_{opt}(h,i) + \beta(h,i) \cdot onoff(h,i), \qquad \forall\ h \in H \qquad 4.5$$

$$\sum_{i=1}^{I} onoff(h,i) \leq 1, \qquad \forall\, h\, \in H \tag{4.6}$$

The methodology and mathematics underpinning the delineation of the limits of the linearised segments are founded upon the minimisation of the MAE error. In the case of a single linearised segment, there is no requirement to optimise the position of the limits; however, the maximum and minimum values of the optimised variable are taken as default. For two linearised segments in order to define the specific position from the linearisation intervals, it is necessary to perform an optimisation, the number of optimised variables can be calculated according to Eq. 4.7, where $n_{segments}$ is the number of linearise segments. In light of the non-linear nature of the problem, Eq. 4.8 and Eq. 4.9, the *fmincon* function can be utilised, a standard algorithm can be used as interior-point, as it is capable of solving non-linear problems whilst respecting certain linear constraints. For this minimisation problem, the lower and upper constraints are delineated in Eq. 4.9 and signify the minimum and maximum values of the optimised variables.

$$n_{opt_{varibales}} = \left(n_{segments} + 1\right) - 2 \tag{4.7}$$

$$MAE = \frac{\sum_{i=1}^{N} |y - \hat{y}|}{N} \tag{4.8}$$

$$\min_{x} MAE(x)\ with\ \ respect\ to, \{\ lb \leq x \leq ub \tag{4.9}$$

4.2.2 Rolling Horizon (RH)

The Rolling Horizon (RH) technique is a decomposition-based strategy employed to address large-scale, dynamic, or stochastic optimisation problems over extended planning horizons [61–63]. In lieu of undertaking the optimisation process over the entire time horizon in a single step, the decision-maker resolves a sequence of smaller optimisation problems over a shorter, finite planning window. This phenomenon can be attributed to the fact that the optimisation times are contingent on the number of variables that are being optimised, with an exponential relationship. Consequently, for small MILP problems, the solving time is really fast, while for problems involving multiple constraints and variables, the utilisation of RH is of fundamental importance to manage the solving time and computational performance. At each Simulation Window (SW), an optimisation model is formulated for the current state of the system over a limited future horizon; only the decisions for the first period (or first few periods) are optimised, then just a part of the simulation window is saved (SP), the difference between SW and SP represents the overlap between two consecutive simulations. The temporal position of the horizon is then advanced, the system state is revised in accordance with actual information (e.g. demand, prices, disturbances), and the optimisation is recalculated for the new time interval. This iterative process is continued until the conclusion of the overall time horizon.

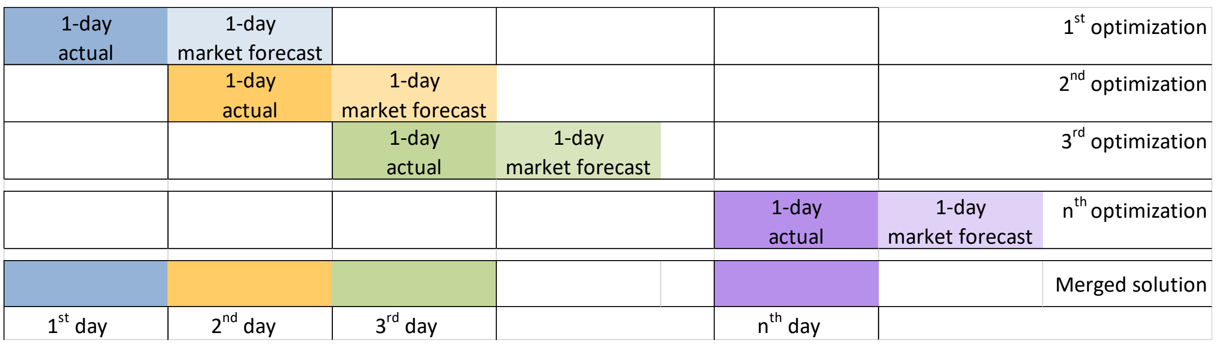

Figure 4.6: Rolling Horizon technique for long horizon optimisation periods [49,61,64].

From a practical perspective, as illustrated in Figure 4.6, n optimisations will be performed over a period of n days, and the solution will be merged afterwards, retaining only the first 24 hours of each optimisation (see the dark shaded parts of Figure 4.6). From the 25th hour onwards, the solution is cut because that period is optimised again by the subsequent optimiser run. The optimiser must operate on the entire period using a Simulation Window (SW) whose width constitutes a fundamental parameter that must be set. As outlined before, a key parameters to set are SW and SP. The following analysis aims to quantify the advantage of adopting the rolling horizon technique with overlap for CCGT and BES day-ahead dispatch scheduling [49,64].

As illustrated in Figure 4.7 and Figure 4.8, the increase in overlap is utilised to optimise the dispatch of the CCGT and BES. Figure 4.7 focuses on the CCGT, and the period between 5th and 6th January 2020 is considered. The power plant is scheduled to be activated at 8 a.m., as the period from 8 a.m. to 11 p.m. is characterised by a positive Clean Spark Spread (CSS), as defined in Eq. 4.10, and the associated cumulative profits are sufficient to pay back the start-up costs.

$$CSS = PZ_t - \left(\frac{C_{Gas_t} + e \cdot C_{CO2}}{\eta_t(T_t, Load_t)} + C_{O\&M} \right) \tag{4.10}$$

Figure 4.7: The impact on the optimal scheduling of the Rolling Horizon technique on CCGT.

However, at 24th hour the plant will be switched off in order to avoid financial loss during the final hour of the day. The CCGT will be started up again at 6 a.m. the following day, in order to exploit the profitable period until 11 p.m. However, with SP equal to 36, the optimiser will have the information until 12 p.m. on the following day to define the optimum scheduling. This will enable the assessment of losses between 5 January at 11 p.m. and 6 January at 6 a.m., which are expected to be less than start-up costs. It therefore follows that the most appropriate course of action would be to keep the power plant on during the night. In order to reduce expenditure during this period, the most effective strategy depends on CSS until 2 a.m. and between 5 a.m. and 6 p.m. CSS is marginally negative; therefore, the optimal approach is to maintain the full load, which will result in increased fuel consumption but ensure high efficiency. When CSS is lower, the most efficient option is to save fuel by running CCGT at the MEL with lower efficiency but with significantly lower losses. As illustrated in the third graph (representing cumulative earnings), there is a clear divergence between the two operating profiles at 11 a.m. on 6 January. The orange profile demonstrates a continuous decrease, while the blue profile maintains a constant value until the moment of start-up. At this point, the start-up cost is paid for, and there is a reversal between the two cumulative gain curves.

As illustrated in Figure 4.8, a similar behaviour is also present for BES on May 25 and 26, 2020. In order to generate a profit from the operation of the battery, it is essential to ensure that there is a minimum difference between the price at which the discharged energy is sold and the price at which energy is purchased during charging. As illustrated by Eq. 4.11, the required minimum selling price is contingent on the charging price and the cost of the cycle.

$$ZP_{disch} > \frac{C_{cycle}}{\eta_{disch}} + \frac{PUN_{ch}}{\eta_{disch}\eta_{ch}} \qquad 4.11$$

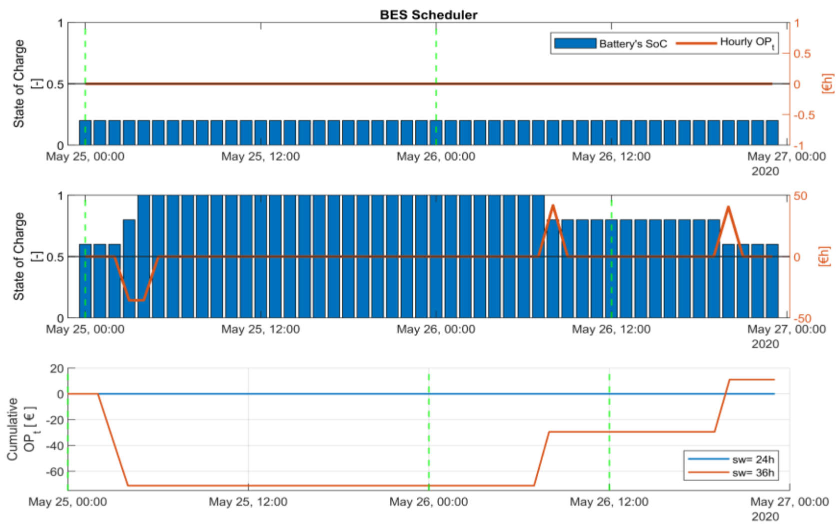

Figure 4.8: The impact on the optimal scheduling of the Rolling Horizon technique on BES.

As illustrated in Figure 4.8, if SW is set to the 24-hour condition, the BES system would not perform any cycles, as maximum price difference is not sufficient to cover the operational and cycling costs. Conversely, if SW is 36 hours, the battery will be charged on 25 May in the early morning, with a subsequent discharge planned during the predicted price peak for the following day late morning and evening. In this manner, under identical market conditions, the dispatch strategy change. To provide a more general overview of the advantages of the rolling horizon technique, various scenarios for CCGT and BES were analysed, as illustrated in Figure 4.9 and Figure 4.10.

Figure 4.9 refers to the CCGT annual Operational Profits (OP) in 2020 and 2021. For the CCGT, the importance of increased SW benefits is emphasised, particularly in less profitable conditions, such as low-price periods or periods of low nominal efficiency. In 2020, profits have the potential to increase by up to 17.3% if the price and temperature of the following 48 hours are known. A SW of up to 36 hours still allows for almost the maximum achievable benefit, an increase of up to 12.4%. Conversely, in the event of favourable market conditions, the 2021 parameters are illustrated by the dashed lines in Figure 4.9. Profits are capped at 1.8%, even with extremely long swaps exceeding 36 hours, and the lowest nominal efficiency is taken into consideration. No further benefits are observed.

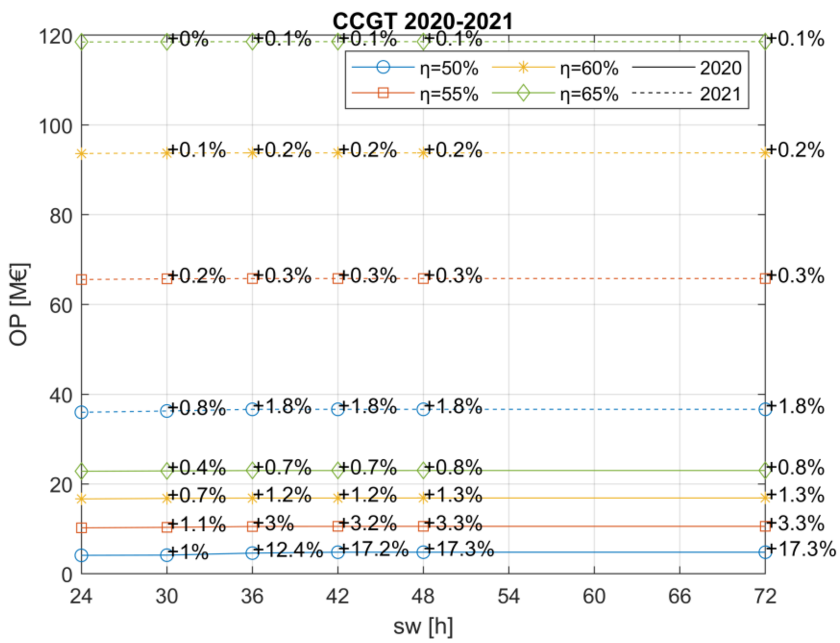

Figure 4.9: Influence of SW on the best dispatch for CCGT, for different market and efficiency scenarios.

Taking the absolute variation of OP into consideration for 2020, an increase in SW up to 36 hours results in a rise between €507,000 and €164,000 compared to SW=24 hours. For 2021, the increase ranges from €663,000 to €68,000. The lower and upper limits of this range correspond respectively to the cases of minimum and maximum nominal efficiency (i.e. 50% and 65%). The observed trend can be explained by reference to the hours leading up to the evening. In the event of high efficiency, the final hours of the day prove to be profitable, and as a result, the optimiser maintains plant operations. In this manner, the optimisation for the following day starts from the plant condition of “on”, as observed in the case of SW equal to 36, thereby diminishing the impact of the sliding window. The maximum attainable gain is approximately €0.5 million for both years. This increase indicates that the maximum benefit in terms of profits will be of a similar order, providing a more accurate indication of the actual benefit that the increased SW can deliver for different markets and efficiency scenarios.

In summary, under average positive CSS conditions (high efficiency and 2021 prices), the effect of the increased forecast capability is reduced to below 1% and is fully expressed with a 36-hour SW. Therefore, the introduction of at least an overnight forecast leads to better results, particularly in less profitable market conditions. In situations where conditions are unfavourable (low efficiency or 2020 prices), it is advantageous to enhance the SW by up to 48 hours. The primary incremental benefit is realised between 36 and 42 hours.

In Figure 4.10, the impact of SW on the optimal BES dispatch is illustrated.

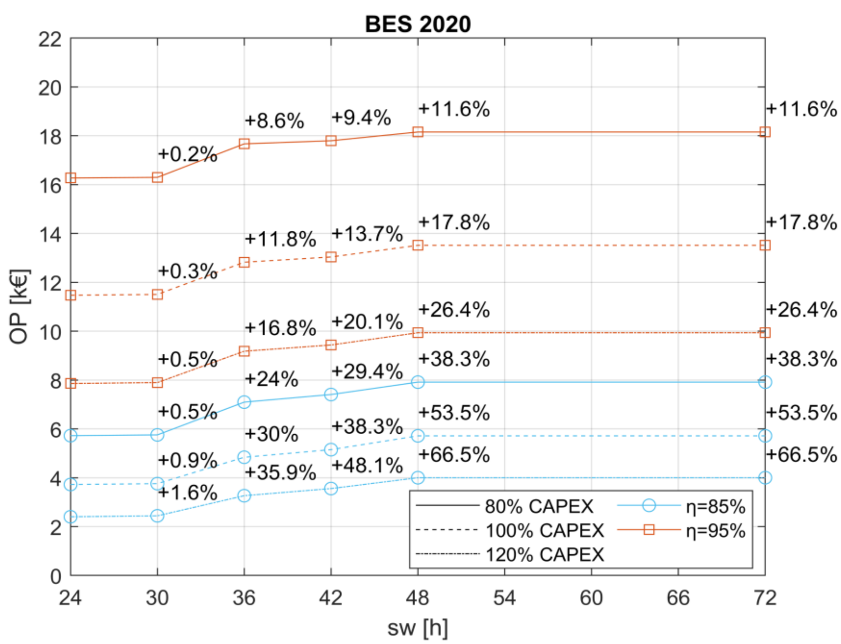

Figure 4.10: Influence of SW on the best dispatch for BES, for different efficiency and CAPEX scenarios.

As the period of optimisation progresses, the probability of Eq. 4.11 being satisfied also increases. As with the CCGT case, a significant increase in SW=24h occurs when SW is extended up to 36h, including the price peak that typically occurs in the following late morning. The ability to forecast prices up to 36 hours in advance has been shown to lead to a potential increase in profits of up to 35%. It is noteworthy that this advantage is most significant in critical situations, i.e. those involving high capital expenditure and low efficiency.

In favourable circumstances, the impact of the sliding-window width is negligible. This effect is due to the fact that BES has the capacity to complete a full charge and discharge cycle within a 24-hour period. This operating condition is facilitated by charging during the middle hours, which are characterised by a low price due to the energy produced from renewable sources, and discharging during the pre-evening hours, which are characterised by a high price due to the absence of renewable sources.

Following a thorough review of the different scenarios, it can be concluded that SW equal to 36h is the recommended value to adopt for CCGT and BES, as this represents the optimum trade-off between achievable profits and optimisation time. For storage periods of up to 48 hours, higher values can result in a substantial increase in profits and should be given due consideration in particularly critical market scenarios.

4.2.3 Big-M methodology

The Big-M technique is a fundamental method used in mathematical modelling to transform non-linear constraints or logical disjunctions (either-or conditions) into a Mixed-Integer Linear Programming (MILP) formulation. It involves the use of an arbitrarily large positive number, denoted as *M*, which is paired with binary variables to activate or deactivate specific constraints within an optimisation problem. In the seminal work by Heragu and Kusiak (1991) [65], the Big-M technique was utilised to develop efficient models for the facility layout problem. Their work is notable for presenting linear mixed-integer models that required fewer integer variables than existing formulations at the time. The actual core challenge in facility layout is ensuring that no two facilities overlap in a given space. Originally, this is expressed as a non-linear absolute value constraint, Eq.4.12:

$$\left|x_i - x_j\right| \geq \frac{1}{2} \cdot \left(l_i + l_j\right) + d_{ij} \qquad 4.12$$

Heragu and Kusiak used the Big-M technique to transform this into linear constraints (Model M1a) by introducing a binary variable z_{ij} as explained in Eq. 4.13 and Eq. 4.14 [65].

$$x_i - x_j + M \cdot z_{ij} \geq \frac{1}{2} \cdot \left(l_i + l_j\right) + d_{ij} \qquad 4.13$$

$$-(x_i - x_j) + M \cdot (1 - z_{ij}) \geq \frac{1}{2} \cdot (l_i + l_j) + d_{ij} \qquad 4.14$$

If z_{ij} is equal to 0, the first constraint is active, forcing facility *I* to be positioned at a specific distance from facility *j*.

If z_{ij} is equal to 1, the first constraint becomes redundant because the large value of *M* ensures the inequality is always satisfied regardless of the facilities' positions. Simultaneously, the second constraint becomes active. This either-or logic allows a linear solver to choose the optimal relative positioning of facilities without needing non-linear absolute value functions.

Beyond the facility layout models proposed in [65], the sources highlight several critical applications in modern engineering [66–68]. The technique is used to transform complex microgrid portfolio management minimax (min-max) robust optimisation problems into a single-level linear maximisation problem. This allows microgrid operators to calculate the minimum cost of balancing power while considering the worst-case scenarios of uncertain renewable energy generation and consumption [69].

In the field of process safety, in chemical plant safety and facility siting, Big-M is used to model separation distance constraints between hazardous units (like storage tanks) and occupied buildings (like control rooms). It enables the optimisation of plant layouts to minimise property damage from potential fires or explosions while remaining within a linear computational framework [66].

In general MILP problems, it is the standard method for modelling disjunctive programming, where the solver must choose between multiple available sets of constraints. While the Big-M technique makes nonlinear problems solvable by commercial linear solvers, it has notable challenges: the value of M must be large enough to render constraints redundant, but setting M too high can lead to numerical instability and significantly slower solver performance. Introducing the binary variables required for Big-M increases the number of integer variables, which can make large-scale problems difficult to solve optimally within a reasonable time. The general approach to defining the start-up cost does not require the Big-M method. This method is typically necessary when the technology's start-up cost depends on an optimisation variable. For instance, the start-up gas of the CCGT is typically a function of the bottoming cycle temperature [70]. To activate the start-up cost, for which Eqs. 4.15 to 4.18 are essential. M_{SU} is the maximum start-up cost, but this value is not generally essential for modelling purposes, as it does not directly affect the objective function, as explained. However, this value must be sufficiently high to avoid the solution being unfeasible, as per Eq. 4.17. To understand the functionality of this set of constraints, the condition with xSU equal to 1 is discussed, where xSU is the binary variable indicating the start-up event. It can be seen from Eq. 4.15 and Eq. 4.16 that the condition. $C_{SU_{opt}}$equal to C_{SU} is necessary for feasibility. The remaining two Eq. 4.17 and Eq. 4.18 are satisfied when the expression becomes strictly greater than zero and remains below the arbitrarily large upper limit imposed by the Big-M parameter. Variable $C_{SU_{opt}}$ is the cost contribution that is considered in the objective function and therefore only activates when start-up occurs. Variable C_{SU} is a continuous variable that calculates the start-up cost at any given moment based on the system conditions, but does not directly enter into the objective function.

$$C_{SU_{opt}}(t) \leq C_{SU}(t) + M_{SU} \cdot (1 - x_{SU}(t)) \tag{4.15}$$

$$C_{SU_{opt}}(t) \geq C_{SU}(t) - M_{SU} \cdot \left(1 - x_{SU}(t)\right) \tag{4.16}$$

$$C_{SU_{opt}}(t) \leq M_{SU} \cdot x_{SU}(t) \tag{4.17}$$

$$C_{SU_{opt}}(t) \geq 0 \tag{4.18}$$

4.3 Main structure

The model's fundamental structure is based on the conceptualisation of buses, each characterised by specific physical properties. These buses may represent either electrical nodes (terminals) or nodes associated with various energy carriers, such as natural gas, hydrogen, water, ammonia, and others.

To ensure the modularity of the tool, it is essential to define the interactions among the different components through appropriate correlations. This approach enables the entire system to be configured via a single input file, currently implemented in Excel format, thereby providing a high degree of flexibility in both modelling and the integration of additional components.

For each bus and at every time step, the fundamental balance equations, namely the conservation of power, energy, and mass must be satisfied. The following sections provide detailed descriptions of the developed modules, with the aim of supporting the modelling and management of complex energy systems.

4.4 Generator Modules

This section presents the modelling of the Generator Modules component. The objective of this section is to illustrate the operational behaviour and performance of the different generation units within the dispatch optimisation framework. Specifically, the developed models delineate the relationship between fuel consumption, electrical power output, and the operational limits of the generation units. These models include relevant technical constraints such as minimum and maximum power output, conversion efficiencies, and other operational conditions required for plant operation. The modelling approach aims to capture the key physical and economic characteristics of each generation technology while maintaining a level of detail compatible with the optimisation framework adopted for the dispatch problem. By accurately representing the performance and constraints of the generation units, the MEDO tool enables evaluation of their contribution to overall electricity production and supports identification of the optimal operating strategy under different market conditions and resource availability. Generators are grouped by the type of energy produced (thermal or electrical) or the type of energy carrier. The subsequent sections present tables containing the parameters used to characterise the specific component and establish interconnections between different buses. Generators can be viewed as converters of various energy sources, subject to efficiency curve limitations.

4.4.1 Electrical power generators

Electrical power generators are energy conversion systems that convert the chemical energy stored in fuels into electrical energy, producing thermal energy as a by-product. These technologies play a central role in the development of the MEDO tool, as they represent the main controllable assets within the dispatch optimisation framework.

This category includes both generators operating on conventional fossil fuels, such as natural gas, heavy fuel oil (HFO), and marine diesel oil (MDO), as well as emerging technologies capable of using alternative, low-carbon fuels, such as hydrogen (H_2). It is therefore essential to accurately model these systems to capture their operational flexibility, performance characteristics, and technical constraints within the optimisation environment.

From a modelling perspective, it is essential to represent fuel-based power generation technologies through relationships that link fuel consumption, electrical power output, conversion efficiency, and operational constraints. Such constraints may include minimum and maximum load levels, ramping capabilities, and operational stability limits. These relationships enable the dispatch optimisation model to determine the most suitable operating point for each generation unit under different economic and system conditions.

Within this framework, several representative fuel-based electricity generation technologies are analysed in this section, including Internal Combustion Engines (ICE), Gas Turbines (GT), Combined Cycle Gas Turbines (CCGT), and Fuel Cells (FC). It is worth noting that these technologies exhibit distinct thermodynamic behaviours, efficiency levels, and operational characteristics. To ensure a realistic representation of the energy system, these factors must be appropriately captured in the dispatch model's mathematical formulation.

In contrast, electricity generation from renewable energy sources is generally treated as an exogenous input in dispatch optimisation models. The available generation from renewable resources is usually determined outside the optimisation framework, based on either measured field data or the processing of environmental resource data, such as solar irradiation, wind speed, or other site-specific indicators. Consequently, the dispatch model incorporates renewable generation as a predefined input profile rather than explicitly modelling the internal physical behaviour of the corresponding technologies.

4.4.1.1 ICE – Internal Combustion Engine

This section introduces the model developed for the internal combustion engine module. Firstly, Table 4.1 is presented that summarises all the parameters necessary to characterise the component's operation and its interconnections with other elements. The table is divided into four sections. The first section includes general information and the component's identification number in the system. The identification name always consists of the first part, which is the identification code of the electrical bus to which it is connected, followed by the component type and a sequential number. The second section contains all the technical information about the component. The third section provides detailed information on the various interconnections with the different buses. Finally, the last section includes general economic operating information, which is primarily related to the system's maintenance costs. Equations 4.19-4.32 are used to characterise the component's operation and model constraints. The values listed in the table should not be regarded as examples of existing technologies, but are intended to illustrate how they should be entered into the input file for the MEDO tool's core code.

Table 4.1: List of input parameters for the Internal Combustion Engine module.

Variable Name	**Acronyms**	**Unite**	**Type**	**Example**
ID Number	*ID Number*	-	string	EL_B1_ICE1
Main fuel type	*Fuel_Type1*	-	string	LNG
Nominal power	*P_nom*	*kW*	double	3500
Load	*Load*	-	vector	0.0;0.75;1
Efficiency	*Eta*	-	vector	0.36;0.38;0.38
Thermal recovery coefficient	*Th_exhaust*	-	vector	0.5;0.48;0.46
Exhaust gas temperature	*T_exhaust*	C°	double	250
Logical dual fuel	*dual_fuel*	-	string	YES/NO
Min mass fraction	*min_fraction*	-	double	0
Max mass fraction	*max_fraction*	-	double	0.1
Max increasing load	*load_var_up*	-	double	1
Max decreasing load	*load_var_down*	-	double	1
Logical on-off condition	*continous_run*	-	string	YES/NO
Second fuel type	*Fuel_Type2*	-	string	CH2_350
Fuel BUS reference	*Fuel_BUS2*	-	string	H2_B1
Electrical BUS ID number	*el_BUS*	-	string	El_B1
Security requirements type 1	*SR1*	-	string	YES/NO

Security requirements type 2	*SR2*	-	string	YES/NO
Logical for thermal recovery	*Th_recovery*	-	string	YES/NO
Thermal BUS ID number	*th_BUS*	-	string	Th_B1
Logical for Start-up cost	*Logical_SU_cost*	-	string	NO
Start-up cost	*SU_Cost*	€/SU	double	N/A
Variable O&M	*OnM_Var*	€/kWh	double	0

As outlined in Section 4.2.1, the PWL technique was employed to model the nonlinear behaviour of the internal combustion engine's off-design curve. Equation 4.19 defines the linearisation limits for the component's power; the limit values are entered via the load defined in the Table 4.1. The number of linearised steps is equivalent to the number of elements in the load vector minus one. For correctness, the efficiency must also have the same dimension; otherwise, the code generates an error. Equations 4.22-4.24 are required to account for the following: start-up costs, if applicable and variable maintenance costs, which are proportional to the energy generated Once defined, the limits are then used to calculate the required chemical power input, Eq. 4.25, which is the variable that is actually linearised. The linearization coefficients α and β are calculated in Eq. 4.26 and Eq. 4.27. Once the coefficients have been calculated, it is necessary to define the constraint for linearising the hourly optimised chemical power in function of the electrical power, Eq. 4.28. Fuel consumption is typically defined as the sum of two contributions. However, if the *dual_fuel* equal to NO option is selected, the model will consider only the primary fluid in the balance, Eq. 4.29 and Eq. 4.30. The relationship between the total flow rate and the required chemical power is defined, and finally, the maximum mass ratios that the mixture can have during operation are defined in Eq. 4.31.

Eq. 4.32 is intended for verification purposes, specifically to assess the error introduced during the linearisation phase.

$$P_{actual}(j) \cdot onoff(t,j) \leq \mathrm{P}(t,j) \leq P_{actual}(j+1) \cdot onoff(t,j) \qquad 4.19$$

$$\Delta load \leq \frac{\sum_{j=1}^{J} |\mathrm{P}(t,j) - \mathrm{P}(t+1,j)|}{P_{nom}} \leq \Delta load \qquad 4.20$$

$$\sum_{j=1}^{J} onoff(t,j) \leq 1 \tag{4.21}$$

$$\sum_{j=1}^{J} (onoff(t-1,j) - onoff(t,j)) + x_{SU}(t) \leq 1 \tag{4.22}$$

$$C_{SU}(t) = x_{SU}(t) \cdot c_{SU} \tag{4.23}$$

$$C_{O\&M}(t) = P(t) \cdot c_{O\&M} \tag{4.24}$$

$$P_{chemical}(j) = \frac{P_{actual}(j)}{\eta_{actual}(j)} \tag{4.25}$$

$$\alpha(j) = \frac{P_{chemical}(j) - P_{chemical}(j+1)}{P_{actual}(j) - P_{actual}(j+1)};\ \forall\ t \in T \tag{4.26}$$

$$\beta(j) = P_{chemical}(j) -\ \alpha(j) \cdot P_{actual}(j);\ \forall\ t \in T \tag{4.27}$$

$$P_{chemical_{opt}}(t,j) = \alpha(j) \cdot P(t,j) + \beta(j) \cdot onoff(t,j) \tag{4.28}$$

$$\sum_{j=1}^{J} P_{chemical_{opt}}(t,j) =\ m_{f1}(t) \cdot LHV_1 + m_{f2}(t) \cdot LHV_2 \tag{4.29}$$

$$m_{tot}(t) = m_{f1}(t) + m_{f2}(t) \tag{4.30}$$

$$fraction_{min} \cdot\ \ m_{tot}(t) \leq m_{f2}(t) \leq fraction_{max} \cdot\ \ m_{tot}(t) \tag{4.31}$$

$$\eta_{model}(i,j) = \frac{P(i,j)}{P_{chemical_{opt}}(i,j)} = \frac{P(t,j)}{\alpha(j) \cdot P(t,j) + \beta(j)} \tag{4.32}$$

4.4.1.2 GT – Gas Turbine

A gas turbine is a power generation technology in which compressed air is mixed with fuel and combusted in a combustion chamber. The high-temperature gases produced by this process expand through a turbine, thereby generating mechanical power that drives an electric generator.

A critical operational consideration is peak firing, which occurs when the turbine operates above its nominal firing temperature to temporarily increase the power output. While this operating mode can provide additional generation during periods of high demand, it does increase thermal stress on components such as turbine blades. Consequently, peak firing accelerates component degradation and leads to higher maintenance requirements and reduced component lifetime. This must be considered when evaluating dispatch strategies [70–72]. From a mathematical standpoint, the techno-economic model of the gas turbine is very similar to the model already developed for the ICE, in terms of the operational aspect and the linearisation process. However, what needs to be added, and has not yet been done in this case, are the Shut-Down costs ,SD , associated with short cycles that limit the plant's lifespan. These require the introduction of the Big-M technique to perform the constraint linearisation process. Furthermore, in addition to linearising the required chemical power, it is also necessary to linearise the Fired Hours, FH, hours as a function of the turbine's load, since their behaviour is linear up to the nominal load and then becomes exponential for higher loads. Please refer to Table 4.2 for a comprehensive overview of all the parameters necessary for the automated generation of the gas turbine model. This approach offers a wide range of modelling options, as it allows for the capture of numerous technical constraints related to gas turbine operation. The values listed in the table should not be regarded as examples of existing technologies, but are intended to illustrate how they should be entered into the input file for the MEDO tool's core code.

Table 4.2: List of input parameters for the Gas Turbine module.

Variable Name	**Acronyms**	**Unite**	**Type**	**Example**
ID Number	*ID Number*	-	string	EL_B1_GT
Main fluid type	*Fuel_Type1*	-	string	Natural Gas
Nominal power	*P_nom*	*kW*	double	3500
Load	*Load*	-	vector	0.0;0.75;1
Efficiency	*Eta*	-	vector	0.39;0.40;0.41
Thermal recovery coefficient	*Th_exhaust*	-	vector	0.5;0.48;0.46
Exhaust gas temperature	*T_exhaust*	C°	double	500
Min mass fraction	*min_fraction*	-	double	0
Max mass fraction	*max_fraction*	-	double	0.1
Max increasing load	*load_var_up*	-	double	1

Max decreasing load	*load_var_down*	-	double	1
Logical on-off condition	*continuous_run*	-	string	YES/NO
Logical dual fuel	*dual_fuel*	-	string	YES/NO
Second fluid type	*Fuel_Type2*	-	string	CH2_350
Fuel BUS reference	*Fuel_BUS2*	-	string	H2_B1
Electrical BUS ID number	*el_BUS*	-	string	El_B1
Security requirements type 1	*SR1*	-	string	YES/NO
Security requirements type 2	*SR2*	-	string	YES/NO
Logical for thermal recovery	*Th_recovery*	-	string	YES/NO
Thermal BUS ID number	*th_BUS*	-	string	Th_B1
Cost of Hot Gas Path Inspection	*HGPI_Cost*	M€	double	31.5
Number of equivalent FH before HGPI	*FH_max_f*	h	double	24000
Can be constant or variable FH	*logic_OnM*	-	string	FH type
FH function of load	*FH_factored*	h	double	1;1;197;3.1
Logical for Fired Hours	*logic_FH*	-	string	YES/NO
Logical for start-up cost	*logic_SU*	-	string	YES/NO
Gas consumed during start-up	*SU_net_GAS*	MWh/SU	double	120
Equivalent FH for start-up	*SU_EOH_eq*	h/SU	double	10
Logical for shut-down cost	*logic_SD*	-	string	YES/NO
Limit for shut-down hours	*SD_FH_limit*	h	double	30

The subsequent section details the extra equations required to describe the turbine's operation; the linearisation of chemical power, load variation and constant startup costs can be modelled in the same manner as for an internal combustion engine Eq. 4.19-4.32. The following equations demonstrate the calculation of variable maintenance costs based on fired hours and the shutdown cost when the turbine is shut down before reaching the minimum operating hour threshold. The Eq. 4.33-4.35 are used to define the linear dependency of FH_f with Power.

$$\alpha_{FH\,j} = \frac{FH_{f\,j} - FH_{f\,j+1}}{P_j - P_{j+1}};\ \forall\, t \in T \tag{4.33}$$

$$\beta_{FH\,j} = FH_{f\,j} - P_j \cdot \alpha_{FH\,j};\ \forall\, t \in T \tag{4.34}$$

$$FH_{opt}(t,j) = \alpha_{FH\,j} \cdot P(t,j) + \beta_{FH\,j} \cdot onoff(t,j) \tag{4.35}$$

The Eq. 4.36 and Eq. 4.37 are essential to define the binary variables. x_{SU} and x_{SD} which are used to include the start-up and shut-down costs, i.e. C_{SU} and C_{SD}, in the objective functions. This binary variables are essential for the Big-M formulation.

$$\sum_{j=1}^{J} x_{P_{opt}}(t,j) = \sum_{j=1}^{J} x_{P_{opt}}(t-1,j) + x_{SU}(t) - x_{SD}(t);\ \forall\, t \in T \tag{4.36}$$

$$x_{SU}(t) + x_{SD}(t) \leq 1;\ \forall\, t \in T \tag{4.37}$$

The equations 4.38 and 4.39 are used to calculate the penalty hours that have to be paid as the plant operates below the limits of fired hours for startup, $c_{O\&M}$ is a specific cost that is calculated dividing the HGPI cost by the maximum number of factored FH.

$$FH_{SD_{pen}}(t) = \begin{cases} FH_{f_{\lim}} - FH_{run}(t), & FH_{\lim} - FH_{run}(t) > 0 \\ 0, & x \geq 0 \end{cases} \tag{4.38}$$

$$C_{SD}(t) = FH_{SD_{pen}}(t) \cdot c_{O\&M} \tag{4.39}$$

The equations from 4.40 to 4.43 are essential to activate the C_{SD} when the short period shut-down occurs. M_{SU} is the maximum shut-down cost, but generally this value is not essential for the modelling purpose as it's not affecting the objective function directly, but this value should be high enough to avoid the non-feasibility of the solution, considering Eq. 4.42. To understand how this set of constraints operates. With x_{SD} =1 the first two Eq. 4.40 and 4.41 are satisfied only when the equality between $C_{SD_{opt}}$ and C_{SD} holds. The remaining two Eq. 4.42 and 4.43 are satisfied, as the expression becomes strictly greater than zero and remaining below the arbitrarily large upper bound imposed by the Big-M parameter.

$$C_{SD_{opt}}(t) \leq C_{SD}(t) + M_{SD} \cdot (1 - x_{SD}(t)) \tag{4.40}$$

$$C_{SD_{opt}}(t) \geq C_{SD}(t) - M_{SD} \cdot (1 - x_{SD}(t)) \tag{4.41}$$

$$C_{SD_{opt}}(t) \leq M_{SD} \cdot x_{SD}(t) \tag{4.42}$$

$$C_{SD_{opt}}(t) \geq 0 \tag{4.43}$$

4.4.1.3 CCGT – Combined Cycle Gas Turbine

A Combined Cycle Gas Turbine (CCGT) represents a highly efficient power generation technology, integrating both gas and steam turbine cycles to optimise energy conversion. In a combined-cycle gas turbine (CCGT) plant, natural gas is combusted in a gas turbine to produce electricity, while the high-temperature exhaust gases are recovered and used to generate steam in a heat recovery steam generator (HRSG). The steam thus generated drives a steam turbine, thereby producing additional electricity without any increase in fuel consumption. It is evident that the dual-cycle configuration employed in CCGT plants enables these facilities to attain efficiencies that surpass 60%, thereby demonstrating a substantial enhancement in comparison to conventional single-cycle plants. The model developed for the gas turbine incorporates startup costs as constant values, while for CCGT the startup costs are dependent on the temperature of the cylinder body in the bottoming cycle. Temperature parameter is of significant importance, as it facilitates the incorporation of the thermal variable within the optimisation model, thereby exerting an influence on the value of the objective function. For the decay of the Steam Turbine Rotor Temperature over time, a simple exponential model was considered, as employed in the previous study [70].

$$T_{rot} = T_{amb} + (T_{rot_d} - T_{amb}) \cdot e^{\frac{-t}{\tau_{rot}}} \tag{4.44}$$

The rotor temperature decay model was estimated on the basis of operating data and modelled as a first-order delay Eq. 4.44, where T_{rot_d} represents the rotor design temperature, i.e. 600°C, and T_{amb} is 25°C, while τ_{rot} = 32 h; the time, t, is expressed in hours. In this stage, the effect of the Stand Still on the drum pressure was not modelled in detail; instead, a 2 MW sparging system was assumed. Furthermore, the modelling of the HRSG temperature decay was not considered at this stage. With regard to the MILP modelling, the Start-Up Net Energy Consumption (NEC) reported in Figure 4.11 is considered to take into account the gas consumption for the overall SU. The figure delineates the initiation of Net Energy Consumption and the rotor temperature decay as a function of Stand-Still Hours.

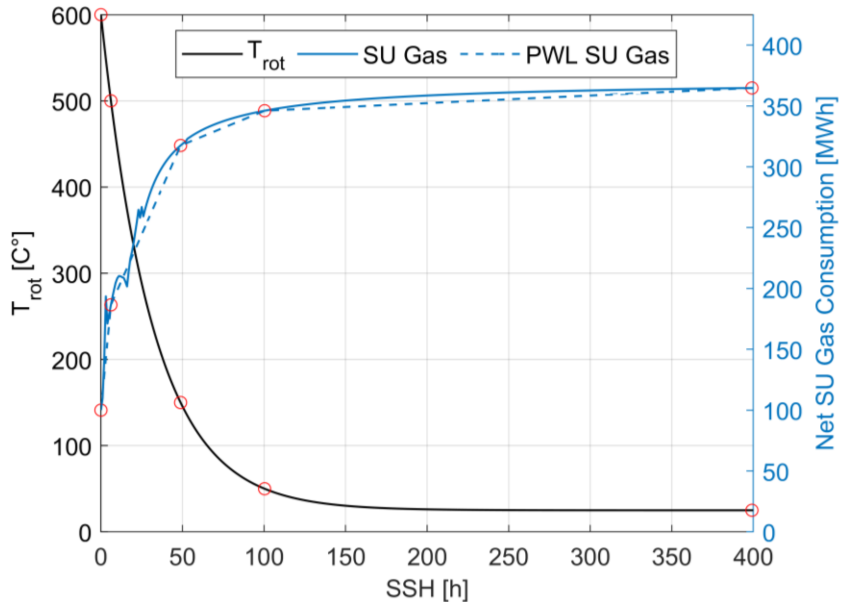

Figure 4.11: Steam Turbine Temperature decay and Start-Up Net Energy Consumption (NEC), in function of Stand Still hours (SSH).

The following Table 4.3 enumerates the various parameters that must be included in order to characterise the CCGT module. It is important to note that the start-up cost is modelled in the same way as peak firing costs. Firstly, a linearisation process of fuel consumption is performed, as demonstrated in Figure 4.11. Secondly, the Big-M technique must be used to activate the start-up cost at the moment it occurs. Moreover, it is evident that startup costs bear a close relationship to rotor temperature. Consequently, it is feasible to keep warm the bottoming cycle trough the utilisation of the EH. In order to calculate the temperature decay function, it is necessary to obtain information regarding the UA and mc_p values of the cylinder body, as well as the EH specifications.

Table 4.3: List of input parameters for the CCGT module

Variable Name	**Acronyms**	**Unite**	**Type**	**Example**
ID Number	*ID Number*	-	string	EL_B1_ICE1
Main fluid type	*Fuel_Type1*	-	string	Natural Gas

Nominal power	*P_nom*	*kW*	double	420000
Load	*Load*	-	vector	0.0;0.75;1
Efficiency	*Eta*	-	vector	0.36;0.38;0.38
Thermal recovery coefficient	*Th_exhaust*	-	vector	0.5;0.48;0.46
Exhaust gas temperature	*T_exhaust*	C°	double	250
Min mass fraction	*min_fraction*	-	double	0
Max mass fraction	*max_fraction*	-	double	0.1
Max increasing load	*load_var_up*	-	double	1
Max decreasing load	*load_var_down*	-	double	1
Mass and specifc heat coefficent	*m_cp*	kW/°K	double	48.8
Heat coefficent and area	*UA*	kW/°K	double	1.5
External temperature for BC	*T_amb*	°C	double	25
Logical on-off condition	*continuous_run*	-	string	YES/NO
Logical dual fuel	*dual_fuel*	-	string	YES/NO
Second fluid type	*Fuel_Type2*	-	string	CH2_350
Fuel BUS reference	*Fuel_BUS2*	-	string	H2_B1
Electrical BUS ID number	*el_BUS*	-	string	El_B1
Security requirements type 1	*SR1*	-	string	YES/NO
Security requirements type 2	*SR2*	-	string	YES/NO
Logical for thermal recovery	*Th_recovery*	-	string	YES/NO
Thermal BUS ID number	*th_BUS*	-	string	Th_B1
Cost of Hot Gas Path Inspection	*HGPI_Cost*	M€	double	31.5
Number of equivalent FH before HGPI	*FH_max_f*	h	double	24000
Can be constant or variable FH	*logic_OnM*	-	string	FH type
FH function of load	*FH_factored*	h	double	1;1;197;3.1
Logical for Fired Hours	*logic_FH*	-	string	YES/NO
Logical for start-up cost	*logic_SU*	-	string	YES/NO
BC temperature range	*T_limits_SU*	°C	vector	25; 150;370;600

Gas consumed during start-up	*SU_net_GAS*	MWh/SU	vector	364.7;346;317.5;100
Equivalent FH for start-up	*SU_EOH_eq*	h/SU	double	10
Logical for shut-down cost	*logic_SD*	-	string	YES/NO
Limit for shut-down hours	*SD_FH_limit*	h	double	30
Logical for Warm Keeping BC	*logic_WK*	-	string	YES/NO
Power EH for WK	*P_EH*	kW	double	2000
Efficiency EH for WK	*eta_EH*	-	double	0.95

4.4.1.4 FC – Fuel Cell

Fuel cells are electrochemical devices that convert the chemical energy of a fuel directly into electrical energy through a reaction with an oxidising agent, typically oxygen from air, without combustion. In contrast to conventional thermal power generation technologies, fuel cells generate electricity through an electrochemical process, enabling higher efficiencies and reduced emissions, particularly when hydrogen is used as the fuel. A standard fuel cell system comprises an anode, a cathode and an electrolyte. At the anode, the fuel (typically hydrogen or a hydrogen-rich gas) is oxidised, releasing electrons and ions. The electrons flow through an external circuit, generating electricity, while the ions migrate through the electrolyte to the cathode, where they react with oxygen to form water and release heat. This mechanism enables fuel cells to deliver high electrical efficiency even at partial load, making them a viable option for distributed generation and energy system optimisation.

There are a number of different types of fuel cells that have been developed. Each type is characterised by the type of electrolyte used and the operating temperature. The most common technologies include the Proton Exchange Membrane Fuel Cell, Solid Oxide Fuel Cell, Molten Carbonate Fuel Cell, and Phosphoric Acid Fuel Cell. Low-temperature fuel cells, such as PEM fuel cells, typically operate below 100 °C and are characterised by fast dynamic response and rapid start-up, making them suitable for applications where frequent power variations occur. High-temperature fuel cells, such as SOFCs and MCFCs, operate at temperatures ranging from approximately 600 °C to 1000 °C. These systems generally exhibit higher electrical efficiencies and the capability to internally reform hydrocarbon fuels, but they have slower start-up times and greater thermal inertia [73,74].

In the context of dispatch optimisation, it is essential to represent the operational characteristics of fuel cells through appropriate constraints and performance models. The decision variables generally correspond to the power output of the fuel cell over time, while constraints define the minimum and maximum operating power, ramping limitations, fuel consumption relationships, and possible start-up or shutdown conditions depending on the technology considered. For instance, high-temperature fuel cells such as SOFC systems are usually modelled as baseload or slowly varying generators, since frequent start-ups and rapid load variations can reduce system lifetime and efficiency. Conversely, PEM fuel cells can be operated more flexibly due to their faster dynamic response. In many dispatch models, the fuel consumption is linked to the electrical output through an efficiency curve or linearized fuel consumption function, which allows the technology to be incorporated into linear or mixed-integer optimisation formulations. Please refer to The values listed in the table should not be regarded as examples of existing technologies, but are intended to illustrate how they should be entered into the input file for the MEDO tool's core code.

Table 4.4, which details all the parameters required to characterise the module in the developed system. The values listed in the table should not be regarded as examples of existing technologies, but are intended to illustrate how they should be entered into the input file for the MEDO tool's core code.

Table 4.4: List of input parameters for the Fuel Cell module.

Variable Name	**Acronyms**	**Unite**	**Type**	**Example**
ID Number	*ID Number*	-	string	EL_B1_FC1
Fuel type	Fuel_Type	-	string	CH2_350
Nominal power	P_nom	kW	double	1200
Load	Load	-	vector	0.0;0.75;1
Efficiency	Eta	-	vector	0.74;0.66;0.64
Thermal recovery coefficient	Th_exhaust	-	vector	0.18;0.16;0.27
Exhaust gas temperature	T_exhaust	C°	double	200

Max increasing load	load_variation_up	-	double	1
Max decreasing load	load_variation_down	-	double	1
Logical on-off condition	continuous_run	-	string	YES/NO
Electrical BUS ID number	*el_BUS*	-	string	El_B1
Security requirements type 1	*SR1*	-	string	YES/NO
Security requirements type 2	*SR2*	-	string	YES/NO
Logical for thermal recovery	*Th_recovery*	-	string	YES/NO
Thermal BUS ID number	*th_BUS*	-	string	Th_B1
Logical for Start-up cost	*Logical_SU_cost*	-	string	NO
Start-up cost	*SU_Cost*	€/SU	double	N/A
Variable O&M	*OnM_Var*	€/kWh	double	0

To describe the cell's operation, we must refer to the equations 4.19-4.32 defined for the ICE, with a single variation represented by the linearization variable, i.e., hydrogen consumption as defined in Eq. 4.45. Once the fuel consumption associated with the cell's operating conditions has been calculated, the α and β coefficients are then calculated in the same way as for an internal combustion engine. In this calculation, the chemical power must be substituted for the fuel consumption in the equation. The constraints required to define dual-fuel operation are not necessary. The key parameter that characterises different cells is represented by Eq. 4.20, which constrains load variations between two consecutive time instants. For cells with longer startup times, i.e. SOC, this value will be lower, while for more flexible cells, i.e. PEM, the value will be higher.

$$m_{H2}(j) = \frac{P_{actual}(j)}{LHV \cdot \eta_{actual}(j)} \tag{4.45}$$

4.4.2 Thermal power generators

Thermal generators are of paramount importance in onboard energy systems in the naval sector, where the reliable supply of heat is essential to ensure both operational functionality and passenger comfort. On board ships, thermal demand is derived from a variety of applications, including space heating, domestic hot water production, fuel preheating, and a range of auxiliary processes. It is evident that electric heaters and fired boilers are among the most commonly adopted thermal generation technologies.

However, it is important to note that each of these technologies offers specific advantages depending on the operational context. This components are also important in the industrial sectors some innovative solutions can be investigated such as High Temperature Heat Pumps [75]. In this work the modelling strategi for the heat pump has been omitted for the seek of simplicity.

Electric heaters represent a straightforward and highly responsive solution, converting electrical energy into heat with near-unity efficiency. These systems are of particular value in hybrid or electrified ship systems, where they can utilise surplus electrical power – potentially generated from low-emission sources or energy storage systems – to meet thermal demand. Conversely, fired boilers depend on fuel combustion to generate heat and are generally employed to ensure reliability and high thermal output, particularly in instances where waste heat recovery is inadequate.

The integration and optimal management of these technologies are fundamental to improving overall system efficiency, reducing fuel consumption, and lowering emissions in modern naval energy systems. In the following chapter the modelling approach has been discussed.

4.4.2.1 EH – Electric Heater

An electric heater is a device that converts electrical energy into thermal energy through resistive heating, typically achieving near 100% conversion efficiency at the point of use. The operation of the device is facilitated by the application of an electric current to a resistive element, which, in accordance with Joule's law, results in the generation of heat. Electric heaters are extensively utilised in residential, industrial, and energy system applications due to their simplicity, reliability, and rapid response time.

In the field of energy system modelling, electric heaters are frequently categorised as flexible loads that can be readily regulated to align with thermal demand. In the context of systems characterised by a high degree of renewable energy penetration, these systems have been shown to be particularly advantageous. Their functionality entails the absorption of surplus electricity, with subsequent conversion into heat. This process serves to mitigate the issue of curtailment. However, the economic performance of these systems is found to be contingent upon the cost of electricity, rendering them particularly advantageous in scenarios characterised by low-cost or excess renewable generation. The modelling of the component is a relatively straightforward process, as it necessitates only piecewise linearisation. For the sake of simplicity, the equations are not shown here, but the same ICE equations 4.19-4.32 can be used by substituting the appropriate primary energy source, which in this case is electrical energy. The following Table 4.5 provides a comprehensive list of all the parameters required to characterise the EH component in the MEDO tool.

Table 4.5: List of input parameters for the Electric Heater module.

Variable Name	Acronyms	Unite	Type	Example
ID Number	*ID Number*	-	string	Th_B1_EH1
Nominal power	*P_nom*	*kW*	double	1000
Load	*Load*	-	vector	0.0;0.75;1
Efficiency	Eta	-	vector	0.94;0.95;0.96
Electrical BUS ID number	*el_BUS*	-	string	El_B1
Thermal BUS ID number	*th_BUS*	-	string	Th_B1
Variable O&M	*OnM_Var*	€/kWh	double	0

4.4.2.2 FB – Fired Boiler

A fired boiler is defined as a thermal generation unit that produces heat by combusting fuel, typically marine diesel oil or natural gas, with the purpose of generating hot water or steam. In the domain of naval systems, fired boilers play a pivotal role in ensuring a reliable supply of thermal energy. This energy is essential for meeting diverse demands within these systems, including space heating, domestic hot water provision, fuel treatment, and auxiliary processes. These systems are of particular importance as backup systems when waste heat recovery from main engines is insufficient, such as during low-load operation or port stays.

Fired boilers have been demonstrated to offer high thermal output and operational reliability. However, it should be noted that their utilisation is associated with additional fuel consumption and emissions, including CO_2 and other pollutants. Consequently, contemporary energy management strategies endeavour to minimise operational demands by prioritising more efficient solutions, such as waste heat recovery systems. Nevertheless, fired boilers remain a critical component in ensuring system flexibility and meeting peak thermal demand under all operating conditions. In accordance with the guidelines established for the EH module, the FB component can be formulated using the same methodology as that employed for the ICE. In this scenario, the chemical energy present in the fuel is converted into thermal energy. Finally, please refer to Table 4.4, which outlines the parameters required to initiate the component modelling process.

Table 4.6: List of input parameters for the Fired Boiler module.

Variable Name	**Acronyms**	**Unite**	**Type**	**Example**
ID Number	*ID Number*	-	string	Th_B1_EH1
Nominal power	*P_nom*	*kW*	double	1000
Load	*Load*	-	vector	0.0;0.75;1
Efficiency	Eta	-	vector	0.96;0.97;0.99
Fuel Type	*Fuel_Type*	-	string	Natural Gas
Thermal BUS ID number	*th_BUS*	-	string	Th_B1
Variable O&M	*OnM_Var*	€/kWh	double	0

4.4.3 Hydrogen Generators

Hydrogen generation technologies are gaining increased attention as a key enabler of low-carbon energy systems due to hydrogen's versatility as both an energy carrier and a storage medium. Among the available technologies, water electrolysis is the most relevant for sustainable applications, as it produces hydrogen by splitting water into hydrogen and oxygen using electricity. When powered by renewable energy sources, this process enables the production of "green hydrogen" with near-zero emissions. The main electrolysis technologies include Alkaline Electrolysers (AEL), Proton Exchange Membrane (PEM), and Solid Oxide Cells (SOC). Each of these technologies has different efficiency levels, operating conditions, and dynamic response capabilities [76,77].

Hydrogen has a variety of uses, including power generation through fuel cells, long-term energy storage, and as a fuel for transport or industrial processes. In integrated energy systems, hydrogen plays a crucial role in balancing supply and demand. It does this by storing excess renewable energy and enabling sector coupling between electricity, heat, and mobility.

4.4.3.1 EC – Electrolyser

In MILP-based optimisation frameworks, electrolyser systems are typically modelled through a simplified yet representative formulation that captures their main operational characteristics while preserving computational tractability. The core decision variable is the electrical power input to the electrolyser, which is directly linked to hydrogen production through an efficiency parameter. This relationship can be expressed as either a constant efficiency or, more accurately, through a piecewise linear approximation to represent performance variations under part-load conditions.

Operational constraints are introduced to reflect technical limits, including minimum and maximum power input, ramping capabilities, and start-up/shutdown conditions when required. In more advanced formulations, binary variables are used to model the on/off status of the electrolyser, enabling the representation of minimum load thresholds and avoiding unrealistic partial operation. The hydrogen is then accumulated over time and can be linked to storage systems or downstream applications such as fuel cells or industrial demand. The linearization process utilises the same equations as defined for the internal combustion engine; the only adjustment required is to modify the variables being linearized. In this instance, the model linearises hydrogen production as a function of the electrical power absorbed by the electrolyzer. Please find below the Table 4.7 with a list of all the parameters required to characterise the component, as per usual.

Table 4.7: List of input parameters for the Electrolyser module.

Variable Name	**Acronyms**	**Unite**	**Type**	**Example**
ID Number	*ID_number*	-	string	EL_B1_EC1
Fuel type	*Fuel_Type*	-	string	CH2_350
Nominal power	*P_nom*	*kW*	double	1000
Load	*Load*	-	vector	0.0;0.75;1
Efficiency	*Eta*	-	vector	0.38;0.64;0.72
Thermal recovery coefficient	*Th_exhaust*	-	vector	0.5;0.32;0.25
Exhaust gas temperature	*T_exhaust*	C°	double	150
Max increasing load	*load_var_up*	-	double	1
Max decreasing load	*load_var_down*	-	double	1

Logical on-off condition	*continuous_run*	-	string	YES/NO
Electrical BUS ID number	*el_BUS*	-	string	El_B1
Logical for thermal recovery	*Th_recovery*	-	string	YES/NO
Thermal BUS ID number	*th_BUS*	-	string	Th_B1
Logical for Start-up cost	*logic_SU*	-	string	NO
Start-up cost	*SU_Cost*	€/SU	double	N/A
Variable O&M	*OnM_Var*	€/kWh	double	0

4.4.4 Feed water generators

Feed water generators constitute essential auxiliary systems in thermal and marine energy plants, responsible for supplying high-quality water to boilers, steam cycles, or hydrogen production units. The primary function of these systems is to ensure a continuous and reliable provision of treated water with appropriate chemical and physical properties, such as low salinity, low dissolved gases, and controlled temperature [78]. These technologies can be categorised into two main groups based on their separation mechanisms: Thermal (Phase-Change) Processes and Membrane Processes [79].

Thermal distillation is a process that involves the application of heat to saline water to induce evaporation. The vapour that results from this process is then condensed into fresh water. The dominant commercial configurations include Multi-Stage Flash (MSF), Multi-Effect Distillation (MED), and Vapor Compression (VC). Conversely, membrane processes such as Reverse Osmosis (RO) and Electrodialysis (ED) utilise semi-permeable barriers or ion-selective media to achieve separation. Energy inputs for these systems are distinct. Membrane processes require high-grade electrical energy to power pumps and maintain electrode polarity. Thermal processes are dual-energy consumers: they require substantial low-temperature heat (low-grade energy) for the phase change and a smaller fraction of electricity for auxiliary pumping. Mechanical Vapor Compression (MVC) is a notable exception, operating as an entirely electricity-driven thermal process.

In the context of naval applications, the production of feed water through desalination processes, such as evaporators or reverse osmosis systems, is often a necessity, given the limited availability of freshwater on board vessels. The generated water is then subjected to further treatment, typically involving deaeration and chemical conditioning, prior to its supply to boilers or other thermal systems. Feed water generators are required to function under conditions of variable load, adapting to fluctuations in thermal demand and system operation.

From a modelling perspective, feed water generators are usually represented through mass and energy balances, thereby linking water production to energy consumption and system demand. In multi-energy systems, where water, heat, and energy flows are strongly interconnected, the integration of these systems is of particular importance. As will be demonstrated in the following chapters, water production plays a fundamental role not only in the maritime sector but also on remote, poorly connected islands in arid climates. These technologies ensure a constant supply of potable water.

4.4.4.1 TPCP – Thermal Phase Change Process

As illustrated below, thermal processes can be categorised into three primary processes.

- Multi-Stage Flash (MSF) Distillation:

  MSF is a robust, though energy-intensive, solution comprising 4 to 40 stages. The process utilises successive stages of decreasing pressure to induce "flashing." Feed seawater is preheated through heat exchangers in each stage before reaching the Top Brine Temperature (TBT), typically between 90°C and 110°C, via an external heat input (e.g., bleed steam from a power plant). The heated brine then enters the first flash chamber at reduced pressure; the resulting vapor condenses on the tube bundles, transferring its latent heat to the incoming feed water [80,81].

- Multi-Effect Distillation (MED)

  MED operates through a series of effects (2 to 16) at decreasing pressure and temperature levels. In contrast to MSF, which relies on sensible heat, MED employs the latent heat of vapor from one effect to evaporate brine in the next. MED is currently experiencing a resurgence in market share, overtaking MSF as a result of its advanced operational TBT (64°C to 70°C), which significantly reduces scaling tendencies and facilitates the use of lower-grade waste heat. Mechanical designs typically adopt two primary configurations. Vertical Tube: seawater boils as a thin film that flows down the inside of the tubes, with vapour condensing on the outer surface. Horizontal Tube: seawater is sprayed onto the exterior surface of horizontal tubes, while vapour condenses internally [82].

- Vapor Compression (VC)

  VC technologies improve efficiency by increasing the temperature of the generated vapour, thereby creating a heat source for the system. Mechanical Vapor Compression (MVC): It utilises an electricity-driven mechanical compressor. It is perfectly suited to small-to-medium applications (100–3,000 m^3/day).

  Thermal Vapor Compression (TVC): The device utilises a steam jet (ejector) to create a vacuum and entrain vapor. TVC can achieve much higher capacities, reaching up to 30,000 m^3/day [83].

As outlined in Table 4.8, the report provides a comprehensive overview of the production systems' characteristics. This facilitates the selection of the most appropriate system for specific application types.

Table 4.8: Operational Parameters of Thermal Processes [79].

Process	**Typical Capacity (m^3/day)**	**TBT Range (°C)**	**Thermal Energy MJ/m^3**	**Electrical Energy kWh/m^3**
MFS	*50’000-70’000*	*90-110*	*190-282*	*2.5-5*
MED	*5’00-15’000*	*64-70*	*145-230*	*2-2.5*
MVC	*100-3’000*	*max 74*	-	*7-12*
TVC	*10’000-30’000*	*63-70*	*220-230*	*1.6-1.8*

As illustrated in Table 4.9, in order to characterise various components for H_2O production, it is necessary to enter specific parameters into the model. It should be noted that, in the case of TPCP processes, in addition to thermal energy, electrical energy may be a requisite. In such conditions, it is possible to define the connection to an electrical bus by using the *el_BUS* variable. . It is possible to define the behaviour of electrical energy consumption as a function of produced water by utilising the *aux* parameter. As with other components, specific coefficients can be used to characterize off-design behaviour if it is not linear.

Table 4.9: List of input parameters for the Thermal Phase Change Process (TPCP) module.

Variable Name	Acronyms	Unite	Type	Example
ID Number	*ID_number*	-	string	H2O_B1_TPCP1
Nominal power	*P_nom*	*kW*	double	1000
Load	*Load*	-	vector	0.0;1
Production for unite of thermal power	*Specific_prod*	m^3/kW_{th}	vector	0.016;0.016
Electrical aux consumption	*aux*	kW/m^3	vector	2.5;2.5
Thermal BUS ID number	*th_BUS*	-	string	Th_B1
Electrical BUS ID number	*el_BUS*	-	string	El_B1
H2O BUS ID number	*H2O_BUS*	-	string	H2O_B1

4.4.4.2 MP – Membrane Process

With regard to the membrane process, there are currently two main techniques that are most widely used, as described below.

- Reverse Osmosis (RO)

  Reverse osmosis is a pressurised filtration process where a semi-permeable membrane acts as the barrier, allowing water molecules to pass while retaining dissolved salts. In order to overcome natural osmotic pressure, significant mechanical energy is required, typically provided by high-pressure pumps. A standard reverse osmosis (RO) installation integrates four critical subsystems. Pre-treatment: This stage is of paramount importance in the process, and involves filtration, sterilisation and chemical dosing to prevent membrane scaling and biofouling. High-Pressure Pump: This component supplies the requisite energy to facilitate the process, with pressures ranging from 17 to 27 bars for brackish water and 55 to 82 bars for seawater applications. Membrane Assembly: The core of the separation is typically composed of spiral-wound or hollow fine fibre configurations. Post-treatment: The ultimate phase of the water quality stabilisation process pertains to the modulation of the pH level and the elimination of dissolved gases, including hydrogen sulphide [84].

- Electrodialysis (ED) and Electrodialysis Reversal (EDR)

Electrodialysis (ED) is an electrochemical separation process operating at atmospheric pressure. ED differs from RO in that it uses a direct electrical current (DC) to move salt ions selectively through ion-permeable membranes, unlike RO, which uses a membrane to move water. The process utilises alternating stacks of cation-permeable and anion-permeable membranes to create alternating channels of concentrated brine and diluted product water. Electrodialysis Reversal (EDR) enhances this process by periodically switching the electrode polarity. This reversal changes the direction of ion movement, effectively converting the concentrate stream into the feed stream and vice-versa. This mechanism serves an automated self-cleaning function, preventing the build-up of precipitants on the membrane surfaces. This, in turn, extends membrane life and maintains process efficiency [85].

As illustrated in Table 4.10, the production capacity and the electrical energy required to produce one cubic metre of water are outlined. SWRO denotes the reverse osmosis process using seawater, while BWRO denotes the same process with brine water; as expected, the specific energy consumption of the RO process is higher when filtering seawater.

Table 4.10: Operational Parameters of Thermal Processes [79].

Process	**Typical Capacity (m^3/day)**	**Electrical Energy kWh/m^3**
SWRO	*Up to 128,000*	*4-6*
BWRO	*Up to 98,000*	*1.5-2.5*
ED	*2-145,000*	*2.64-5.5*

Table 4.11details all the information required to characterise the MP module. Please note that the off-design behaviour of the technology can be defined using the *Specific_prod* parameter when field values are available.

Table 4.11: List of input parameters for the Membrane Process module.

Variable Name	Acronyms	Unite	Type	Example
ID Number	*ID_number*	-	string	H2O_B1_MP1
Nominal power	*P_nom*	*kW*	double	1000
Load	*Load*	-	vector	0.0;1
Water production from an electrical power unit	*Specific_prod*	m3/kW	vector	0.016;0.016
Electrical BUS ID number	*el_BUS*	-	string	El_B1
H2O BUS ID number	*H2O_BUS*	-	string	H2O_B1

4.5 Storage Modules

Energy storage technologies have been identified as playing a fundamental role in contemporary energy systems, particularly in supporting the integration of renewable energy sources and enhancing system flexibility. It is evident that among the most widely adopted solutions are Battery Energy Storage Systems (BES) and Pumped Hydro Storage (PHS), which operate on different principles and time scales.

Battery Energy Storage Systems (BES) are defined by their capacity to store electrical energy in the form of electrochemical energy, a process which is characterised by high efficiency, fast response time, and modularity. These systems are especially well-suited for short-term applications, including peak shaving, frequency regulation, and energy arbitrage. BES have been demonstrated to possess the capability of rapidly alternating between states of charge and discharge. This property renders them particularly well-suited to the management of sudden fluctuations in renewable energy generation and demand. However, their storage capacity is typically limited, and their lifetime is affected by the number of charge-discharge cycles [86,87].

Conversely, Pumped Hydro Storage (PHS) represents a well-established and large-scale storage technology that utilises gravitational potential energy. The operational mechanism entails the transfer of water from a lower reservoir to an upper reservoir during periods of surplus electricity generation. Subsequently, the water is released through turbines, thereby facilitating the generation of power when demand is high. PHS systems offer substantial storage capacities and extended discharge durations, rendering them well-suited for medium- to long-term energy balancing. Despite the necessity for specific geographical conditions and a high initial investment, these systems offer high reliability, a long lifetime, and relatively low operational costs [88,89].

4.5.1 BES – Battery Energy Storage

Battery Energy Storage (BES) represent a key enabling technology for addressing temporal imbalances between electricity generation and demand, particularly in modern power systems characterised by high penetration of variable renewable energy sources. From an architectural perspective, BES typically consist of electrochemical storage units, most commonly lithium-ion and lead-acid batteries, integrated with power conversion systems and advanced control layers. Lead-acid technologies remain attractive for large-scale applications due to their maturity, cost-effectiveness and high recyclability [90]. Recent advancements, such as carbon-enhanced electrodes and hybrid configurations (e.g., Ultra Battery), have improved performance under partial state-of-charge conditions. In contrast, lithium-ion batteries are the preferred option due to their superior energy density and efficiency, although sophisticated battery management systems are required to ensure safe operation and to monitor key parameters such as state of charge (SOC) and state of health (SOH). BES provide a broad range of energy management services, including frequency regulation through rapid power injection or absorption to stabilise grid frequency, voltage support via reactive power control, and energy arbitrage by shifting energy from low-demand to peak-demand periods. Furthermore, they contribute to system resilience by facilitating backup supply and black start capabilities. Their effectiveness is further increased by integrating them with renewable generation assets, such as photovoltaic and wind systems. In these cases, they mitigate intermittency and reduce curtailment. Hybrid Energy Storage Systems (HESS) combine complementary technologies (e.g. batteries and supercapacitors) and aggregated or virtual storage configurations, including distributed residential batteries and electric vehicle fleets. This further expands the operational flexibility of BES [91].

From an operational perspective, performance and longevity are evaluated through metrics such as usage frequency, usage intensity, and, most crucially, state of health, which reflects battery degradation over time. These parameters are essential for optimising both the technical performance and economic viability of BES deployments in increasingly dynamic and decarbonised energy systems. This technology is highly relevant in today's world, both in terms of grid and the management of onboard loads. Consequently, the degradation behaviour of these systems has been analysed, as well as the correlation between this degradation and cycling or idle costs, and how this type of cost can be included in the MILP modelling process. A more exhaustive examination of these aspects is available in the Chapter 5.

As illustrated in Table 4.12, the inputs employed for the characterisation of the BES module are enumerated. In accordance with standard practice, the linearisation process is executed through the utilisation of vectors defined for the c-rate and efficiency. This enables the power flows to be connected in a manner that is consistent with the power drawn from or fed into the system by the battery.

Table 4.12: List of input parameters for the Battery Energy Storage module.

Variable Name	**Acronyms**	**Unite**	**Type**	**Example**
ID Number	*ID_number*	-	string	EL_B1_EC1
Capacity	*Capacity*	*kWh*	double	1000
Minimum State of Charge	*min_SoC*	-	double	0.2
Charging C-rate	*Crate_ch*	-	vector	0.0;0.75;1
Discharghing C-rate	*Crate_disch*	-	vector	0.0;0.75;1
Charging efficency	*eta_ch*	-	vector	0.65;0.89;0.92
Discharging efficency	*eta_disch*	-	vector	0.65;0.89;0.92
Iniziatial State of Charge	*SoC_i*	-	double	1
Electrical BUS ID number	*el_BUS*	-	string	El_B1
Security requirements type 1	*SR1*	-	string	YES/NO
Security requirements type 2	*SR2*	-	string	YES/NO

4.5.2 PHS- Pumped Hydro Storage

Pumped Hydroelectric Storage (PHS) is the global leader in bulk electrical energy storage, accounting for approximately 96% of total storage power capacity and 99% of energy storage volume worldwide. The technology functions on the principle of gravitational potential energy. It employs surplus electricity, typically during periods of high renewable generation or low demand, to facilitate the transfer of water from a lower reservoir to an elevated upper reservoir. In circumstances where supply falls short of demand, stored energy is recovered by releasing water through turbines, thereby facilitating electricity generation. The PHS is distinguished by its high round-trip efficiencies of 70–85% and an exceptional operational lifespan that often exceeds 50-100 years. It provides essential ancillary services to the grid, including frequency regulation, black-start capability, and critical rotational inertia. Although initially developed to complement inflexible nuclear baseload generation, modern PHS is increasingly vital for mitigating the variability inherent in substantial solar and wind deployments. This is because these renewable energy sources lack the inherent energy storage of traditional fossil fuels. Emerging developmental trends are shifting towards closed-loop, off-river systems in order to bypass the environmental and social constraints of traditional river-based projects. Global surveys have identified over 616,000 potential off-river sites, representing 150 times the capacity required to support a 100% renewable global electricity system. Notwithstanding the aforementioned advantages, new deployment in liberalised markets is frequently impeded by the elevated capital intensity of projects and "split incentive" issues, wherein the manifold systemic benefits proffered by storage are not invariably directly remunerated by prevailing market revenue mechanisms [88,89].

PHS systems are of vital importance, especially for power grids with limited interconnection and a high installed capacity of renewable energy sources [92]. Consequently, effective management strategies to minimise curtailment can yield substantial benefits in terms of cost reduction and emissions reduction. As with all other components, the necessary modules have been developed to characterise this technology. In this case, however, the system is more complex, as three main components of the plant can be identified: the pumping system, the power generation system (i.e. hydraulic turbines) and the storage reservoirs. Therefore, all three components have been modelled separately, ensuring maximum flexibility in the design of the pumping plant, even at multiple levels with different pumping and generation stations. Please find below the three tables used to characterise the components. As is customary, the operating curves were linearised using the piecewise technique; in this case, electrical power consumption or generation was linked to the required volumetric flow rate. The linearisation process is based on the same approach that has already been defined for the internal combustion engine in section 4.4.1.1.

Table 4.13: List of input parameters for the Hydro Pump module.

Variable Name	**Acronyms**	**Unite**	**Type**	**Example**
ID Number	*ID_number*	-	string	El_B1_HP1
Nominal power	*P_nom*	*kW*	double	1000
Load	*Load*	-	vector	0.0;1
Efficiency	*Eta*	-	vector	0.7;0.72
Geodetic potential	*delta_h*	m	double	

Lower Reservoir	*Reservoir_from*	-	string	HR_2
Upper Reservoir	*Reservoir_to*	-	string	HR_1
Electrical BUS ID number	*el_BUS*	-	string	El_B1

Table 4.14: List of input parameters for the Hydro Turbine module

Variable Name	Acronyms	Unite	Type	Example
ID Number	*ID_number*	-	string	El_B1_HT1
Nominal power	*P_nom*	*kW*	double	1000
Load	*Load*	-	vector	0.0;1
Efficency	*Eta*	-	vector	0.82;0.9
Geodetic potential	*delta_h*	m	double	
Lower Reservoir	*Reservoir_in*	-	string	HR_1
Upper Reservoir	*Reservoir_from*	-	string	HR_2
Security requirements type 1	*SR1*	-	string	YES/NO
Security requirements type 2	*SR2*	-	string	YES/NO
Electrical BUS ID number	*el_BUS*	-	string	El_B1

Table 4.15: : List of input parameters for the Hydro Reservoir module

Variable Name	Acronyms	Unite	Type	Example
ID Number	*ID_number*	-	string	HR_1
Capacity	*Capacity*	m^3	double	60000
Minimum State of Charge	*min_SoC*	-	double	0.1
Geodetic potential	*Initial_SoC*	-	double	0.5
Rainfall	*Rain_Profile*	m^3/time	string	Rain_1
Evaporation	*Evaporation_profile*	m^3/time	string	Eva_1
Waste	*Waste_profile*	m^3/time	string	Waste_1

Chapter 5

Advanced BES Degradation Modelling

The global transition towards low-carbon energy systems is not limited to the electricity sector alone; it is increasingly extending to the transport sector, where electrification and hybridisation are emerging as key strategies for reducing greenhouse gas emissions and dependence on fossil fuels. In particular, the maritime and naval sectors are undergoing a significant technological transformation driven by stricter environmental regulations, rising fuel costs, and the need for enhanced operational efficiency. These developments have established energy storage systems as a pivotal component in the evolution of contemporary naval power and propulsion architectures, thanks to the high RTE, normally in the range of 0.8-0.85 [87,93].

Naval and maritime vessels are distinguished by complex and highly dynamic power demand profiles, stemming from propulsion requirements, on-board auxiliary systems, and mission-specific operational constraints. While for the remote grid application, as for the isolated island grid, the role of BES is becoming crucial. The integration of renewable energy sources further amplifies the need for flexible and reliable energy storage solutions for both the naval and grid sectors. In the context of energy storage, Battery Energy Storage Systems (BESS) have been shown to play a critical role by enabling a number of functions. These include, but are not limited to, peak shaving, load levelling, frequency regulation, silent operations, and improved fuel efficiency in hybrid and fully electric vessels, increasing the grid security [94]

In the realm of storage technologies, lithium-ion batteries have emerged as a leading contender for naval applications, exhibiting a range of advantageous characteristics. These batteries possess high energy density, rapid response times, modular design, and technological maturity, making them a promising solution for naval operations. However, the operational environment of naval vessels, characterised by variable load cycles, frequent partial charge-discharge events, elevated current rates, and demanding thermal conditions, poses significant challenges for the management of battery lifetime. Consequently, degradation phenomena exert a direct influence on system reliability, safety, and lifecycle costs, rendering degradation-aware operational strategies imperative for sustainable deployment.

Battery degradation is the result of two main factors. Firstly, cycling ageing, which is linked to charge-discharge operations, and secondly, calendar ageing, which occurs during periods of idleness and during storage at varying states of charge and temperatures. Despite this, extant optimisation frameworks for battery dispatch – both in stationary grid applications and transport systems – have predominantly focused on cycling degradation, often neglecting the contribution of calendar ageing. It is imperative to review various degradation models and identify a methodology that can accommodate them in the context of dispatching problems.

This chapter focuses on a comprehensive review of lithium-ion battery ageing models relevant to both stationary and naval applications. The models take into account the influence of Depth of Discharge (*DoD*), State of Charge (*SoC*), Temperature (*T*), Current Rate (*C-rate*), number of cycles (N_{cycles}), and time (*t*) [95].

5.1 BES ageing process

The performance of a BES system is subject to deterioration over time due to the process of ageing, which results in a gradual decline of its nominal parameters. Among these effects, capacity fade, defined as the reduction in the maximum amount of energy that can be stored, has a significant impact on BES operating conditions. Conversely, power fade, which corresponds to the reduction of the maximum power achievable during the charging and discharging phases, is generally considered negligible for lithium-ion batteries [96]. The State of Health (SoH), in Equation 5.1, is defined as the ratio of rated capacity to the nominal value. In the case of most lithium-ion batteries for energy storage systems (BES) and applications such as daily energy arbitrage or integration in smart grids, the End-of-Life (EoL) is typically fixed at 20% of fade, SoH=80%. In instances where this threshold value is not met, the performance is inadequate for the continued operation of BES [87,97].

$$SoH = \frac{C_{rated}}{C_{nom}} \cdot 100\% = 100\% - C_{fade} \quad [\%] \tag{5.1}$$

$$C_{fade_{idling}} = g(SoC, T, t) \quad [\%] \qquad 5.2$$

As Stroe et. al have highlighted in their works [96,98], performing an experimental campaign on the degradation behaviour of LiFePO4/C/C. It has been demonstrated, in Figure 5.1, that the batteries utilised for Primary Frequency Regulation will, after a period of 10 years, have reached the EoL criterion, exhibiting a 20% reduction in capacity. Non-linear behaviour is evident, especially in the early years of the system's life, before becoming linear over time. A 3.5% reduction in maximum power is observed in Figure 5.2, which also demonstrates linear dependence over time.

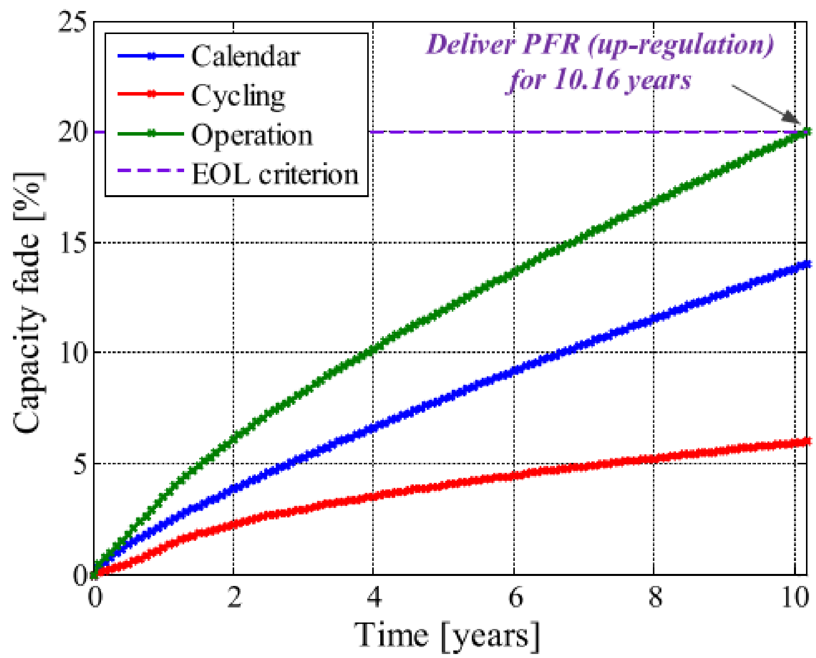

Figure 5.1: Capacity fade decrease of the LiFePO4/C battery cells subjected to the PFR mission profile [96,99].

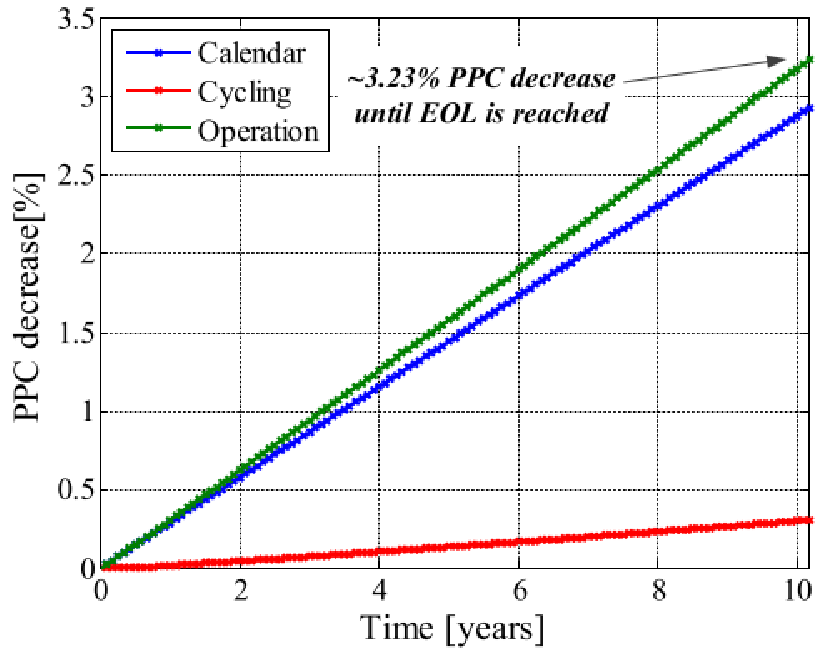

Figure 5.2: Power capability decrease of the LiFePO4/C battery cells subjected to the PFR mission profile [96,99].

The rated capacity of a lithium-ion BES is subject to a continuous decrease, attributable to two primary degradation mechanisms. The initial phenomenon is that of cycling ageing, which is associated with the repeated charge–discharge cycles experienced by the battery. The subsequent phenomenon is that of calendar ageing, which occurs during periods of inactivity, even in the absence of any battery usage. Both cycling and calendar ageing are influenced by several operational and environmental parameters, which affect the capacity degradation rate and ultimately reduce battery lifetime.

$$C_{fade_{cycling}} = f\left(DoD, C_{rate}, T, SoC_{avg}, n_{cycle}\right) \quad [\%] \qquad 5.3$$

$$C_{fade_{idling}} = g(SoC\ , T, t) \quad [\ \%\ ] \qquad 5.4$$

Equations 5.3 and 5.4 describe the parameters affecting calendar and cycling capacity fade, respectively. The functional relationships between degradation and these parameters (e.g. linear or exponential) are reported in Table 5.1 for cycling and Table 5.2 for calendar ageing parameters based on different literature sources. In sections 5.2 and

5.3, the impact and coefficients for the degradation functions are described for the models analysed, with the objective of generalising different models into a single syntax categorised by specific coefficients, for both cycling and calendar ageing models.

Table 5.1: The relationship of cycle ageing parameters on degradation models

		Cycling Ageing			
Reference Number	**DoD**	**n_{Cycle}**	**SoC_{avg}**	**T**	**C-rate**
[100]	exp	linear	-	hyperbolic	-
[101]	exp	linear	-	-	-
[96,98,99]	power	root-square	exp	exp	-
[95,102]	exp	exp	exp	exp	exp
[103,104]	poly	linear	-	poly	-
[105]	poly	linear	-	-	-
[44]	exp	linear	-	-	-

Table 5.2: The relationship of calendar ageing parameters on degradation models

	Calendar Ageing		
Reference Number	**SoC**	**T**	**time**
[100]	-	-	-
[101]	-	-	-
[96,98,99]	exp	exp	exp
[95,102]	exp	exp	exp
[103,104]	poly	poly	linear
[105]	poly	-	linear
[44]	-	-	-

The following Equations 5.5-5.9 are widely applicable in defining the cumulative degradation that a BES reaches after a specific number of operating or idle conditions.

$$EoL = \int_0^{N_{cycle_{max}}} f'(DoD, C_{rate}, T, SoC_{avg}) dn_{cycle} \quad [\%] \tag{5.5}$$

$$N_{cycle_{max}} = \frac{EoL}{f'(DoD, C_{rate}, T, SoC_{avg})} \tag{5.6}$$

$$EoL = \int_0^{t_{max}} g'(SoC\ ,T)dt \quad [\%] \tag{5.7}$$

$$t_{max} = \frac{EoL}{g'(SoC\ ,T)}\ [h] \tag{5.8}$$

$$DoD = SoC_{start} - SoC_{end} \tag{5.9}$$

Equation 5.5 provides a quantitative expression for the cumulative degradation of the BES before reaching the EoL criterion. In the event that *f* is found to be linearly dependent on the number of cycles, n_{cycle}, the maximum attainable value for N_{cycle} can be elucidated, as delineated in Equation 5.6. This is achieved by deriving the function *f'* from *f*, the derivative of *f* with respect to n_{cycle}. EoL can be assumed to be equal to 20% of capacity fade from the nominal condition. Analogously, Equation 5.7 defines t_{max}, the calendar lifespan of the battery after which the EoL is reached, even in the absence of any cycle. In the event of function *g* being linearly dependent on *t*, t_{max} can be explicated as in Equation 5.8, where *g'* is the derivative of *g* with respect to *t*. Finally the Equation 5.9 defines the DoD as the difference between the initial and final state of charge for a cycle.

5.2 Cycle ageing process

It has been established that, as a battery undergoes charging and discharging cycles, its electrodes gradually deteriorate and become less efficient at retaining and releasing energy. This process is known as cycling ageing. A considerable number of authors have conducted analyses of the factors that influence the process of cycling ageing [44,95,96,98–100,102–106]. All of the authors agree that the DoD is of primary importance in cycling degradation models. It has been determined that, given the presence of disparate dependencies within the models on the same operating parameters – for instance, polynomial or exponential – a uniform nomenclature must be implemented for all fitting coefficients of the various degradation functions. The table will facilitate enhanced comparison and comprehension of the diverse degradation models. The subscripts of the fitting coefficients are to be interpreted as referring to the operational parameter. For instance, a_{DoD} signifies the fitting coefficient with regard to the depth of discharge. Only Equation 5.12 has been presented with a specific discussion of the degradation parameters. This is due to the fact that it contains coefficients that are not easily generalisable, in contrast to those contained in other models. This is due to the fact that the proposed model considers the combination of the contributions of the two degradation mechanisms into a single degradation function [95,102].

The first work in the open literature that has been found, provided in 2011 by Zhou et al. [100] for V2G (Vehicle to Grid) applications, defines a degradation curve in which the relationship between the DoD and the admissible number of cycles $N_{cycle\ max}$ has been described. In this work, the impact of some parameters (temperature and DoD) is investigated for different battery energy storage types (Lithium-ion, lead-acid, and nickel metal hydride). Concerning the temperature, Zhou suggests using a hyperbolic correlation, resulting from the Arrhenius equation [107]. Meanwhile, the DoD dependence is logarithmic; thus, the number of cycles exponentially increases as the DoD decreases.

Mallon et al. [101] proposed new coefficients for the equation reported by Zhou in order to describe the DoD influence on the number of cycles. In this work, the temperature dependence was not mentioned. The proposed equations were utilised in heavy-duty electric powertrain applications, with the objective of assessing the impact of the installation of solar panels on the bus's roof and sides on the battery's lifespan.

$$C_{fade_{cycling}} = a_{DoD} \cdot DoD^{b_{DoD}} \cdot \mathrm{e}^{\left(c_{DoD} \cdot (1-DoD)\right)} \cdot n_{cycle} \tag{5.10}$$

Equation 5.10 provides a description of the ageing relationship that was previously proposed by Zhou et al. and subsequently adopted and revised by Mallon.

Stroe et al. [96,98,99] have analysed in detail the influence of more, with respect to Zhou, operating and idling parameters, developing models not only for the battery capacity fade but also for the battery power degradation, for specific lithium-ion phosphate/graphite batteries ($LiFePO_4$ or LFP). An equivalent electrical circuit performance-degradation modelling approach was adopted for the development of the lifetime models, with consideration given to both cycling and calendar processes. The calendar ageing model will be discussed in Section 5.3. The initial application for which they were tasked with developing a degradation model was for an integrated wind power plant, with the aim of compensating for the stochastic nature of wind energy [98].

$$C_{fade_{cycling}} = a \cdot \left(a_{DoD} \cdot DoD^{b_{DoD}} \right) \cdot \mathrm{e}^{\left(a_{SoC} \cdot SoC_{avg}\right)} \cdot n_{cycle}^{a_n} \cdot \left(a_T \cdot \mathrm{e}^{b_T \cdot T}\right) \tag{5.11}$$

In Equation 5.11, the dependence on the number of cycles is polynomial (degree 0.5), while to quantify the dependence on the DoD. An exponential function describes the temperature impact on capacity fade. Stroe's analysis concludes with a consideration of the average State of Charge (SoC_{avg}), which exhibits an exponential decrease. A high average SoC has been shown to exert a favourable influence on the degradation rate, thereby extending the lifespan.

Xu et al. [95] analyse both ageing processes, taking into consideration all operating and idling parameters. The model under scrutiny herein integrates theoretical considerations and empirical evidence in its analysis. The degradation model is predicated on two primary stress functions: calendar ageing and cycling ageing. The model was employed for the purpose of conducting a techno-economic analysis of Primary Frequency Regulation (PFR) and Dynamic Frequency Regulation (DFR) provision by storage. The models' fitting parameters were defined for Lithium Manganese Oxide (LMO). In contrast to the other proposed models, the calendar and cycling ageing do not linearly impact faded capacity, as illustrated in Equation 5.12.

$$C_{fade} = 1 - p_{sei} \cdot e^{-r_{sei} \cdot f_d} + (1 - p_{sei}) \cdot e^{-f_d} \tag{5.12}$$

Where:

p_{SEI} and r_{SEI} are two constants that characterise different BES technologies and are correlated with the formation of a combination of stress functions. While f_d is a combined degradation function consisting of two terms: $f_{cycling}$ is the contribution due to the cycling ageing process, and $f_{calendar}$ is the contribution due to the calendar ageing process. The following Equations 5.13-5.17 define the cycling contribution $f_{cycling}$, while the parameters impacting the calendar, $f_{calendar}$, will be discussed in the subsection Calendar ageing process.

$$f_{cycling} = f_{DoD}(DoD) \cdot f_{SoC}\left(SoC_{avg}\right) \cdot f_{C_{rate}}(C_{rate}) \cdot f_T(T) \cdot n_{cycle} \tag{5.13}$$

$$f_{DoD}(DoD) = \left(a_{DoD} \cdot DoD^{b_{DoD}} + c_{DoD}\right)^{-1} \tag{5.14}$$

$$f_{SoC}(SoC) = e^{a_{SoC} \cdot \left(SoC - SoC_{ref_{avg}}\right)^2} \tag{5.15}$$

$$f_{C_{rate}}(C_{rate}) = e^{a_{C_{rate}} \cdot \left(C_{rate} - C_{rate_{ref}}\right)} \tag{5.16}$$

$$f_T(T) = e^{a_T \cdot (T - T_{ref}) \cdot \frac{T_{ref}}{T}} \tag{5.17}$$

Equation 5.13 is the product of 4 functions describing the impact of the DoD, SoC, C-rate, and temperature. $f_{cycling}$ has a polynomial dependence on the DoD that plays the major role; the function can be observed in Equation 5.14. The other parameters have an exponential impact on $f_{cycling}$ when they deviate from the reference values, Equations 5.15-5.17. As posited by Stroe et al. [98], the extent of battery life is found to be diminished when the device is operating in a high SoC; conversely, a low SoC has been demonstrated to enhance battery life. In contrast, Xu et al. [95] observe a symmetrical trend with respect to the 50% state of charge, increasing the impact of extreme SoC. Xu et al. are the only researchers who have pointed out the dependence of the number of cycles with respect to C-rate (i.e., the current rate at which the charge and discharge phases occur, defined as a ratio between the charging/discharging power and the nominal capacity)

In a separate work, Xu et al. [102] have conducted a techno-economic analysis of PFR and DFR, encompassing various lithium-ion battery technologies, including Lithium Iron Phosphate (LFP), Lithium Nickel Manganese Cobalt Oxide (NMC), and Lithium Manganese Oxide (LMO).

Sayfutdinov et al. [103,104] presented a polynomial model to describe the dependence on both cycling and calendar ageing mechanisms. The model was employed to optimise the dimensions of the energy storage system, taking into account the impact of degradation over time. A comparative analysis was conducted on four distinct lithium-ion models, with the consideration of disparate fitting coefficients for each model. The following materials are of particular interest in this study: Lithium Iron Phosphate (LFP), Lithium Nickel Manganese Cobalt Oxide (NMC), Lithium Manganese Oxide (LMO) and Lithium-Titanium Oxide (LTO). In this study, the sole parameters given consideration are the DoD and the temperature. Utilising a quadratic function enables the impact on capacity degradation to be described.

Fallahifar et al. [105] employed Sayfutdinov et al. models to characterise the capacity degradation function for cycling and calendar fade, while defining the fitting coefficients for their specific batteries. The degradation model is applied to establish the optimal scheduling in microgrid applications, taking into account capacity fade. A range of lithium-ion technologies is under consideration, encompassing Lithium Iron Phosphate (LFP), Lithium Nickel Manganese Cobalt Oxide (NMC), Lithium Manganese Oxide (LMO), and Lithium-Titanium-Oxide (LTO).

$$C_{fade_{cycling}} = (a_{DoD} \cdot DoD^2 + b_{DoD} \cdot DoD) \cdot (a_T \cdot T^2 + b_T \cdot T + c_T) \cdot n_{cycle} \qquad 5.18$$

Equation 5.18 elucidates the relationship for Sayfutdinov et al. and Fallahifar et al., previously delineated. In this particular case study, the second-order polynomial employed to delineate the dependence on *T* is equivalent to 1, with the consequence that the temperature effect is disregarded.

Lee et al. [44] considered only the dependence of DoD on the capacity degradation, expressed by an exponential relationship. The proposed model was utilised to ascertain the most effective method for managing cycling costs in the context of scheduling issues. In the subsequent equation, Equation 5.19, the relationship previously delineated for the Lee et al. models can be observed.

$$C_{fade_{cycling}} = (a_{DoD} \cdot DoD^2 + b_{DoD} \cdot DoD) \cdot (a_T \cdot T^2 + b_T \cdot T + c_T) \cdot n_{cycle} \qquad 5.19$$

As illustrated in Table 5.3, the coefficients for the models under discussion are presented in order to facilitate a clearer and more straightforward comparison between the various models for the reader. It is imperative to carefully consider whether the coefficients reported in the different works have been calibrated for percentage DoD or for dimensional values.

Table 5.3: The fitting coefficient for each cycling ageing model

Constant	**[100]**	**[101]**	**[96,98,99]**	**[108]**	**[95,102,106]**	**[103,104]**	**[105]**	**[44]**
a	-	-	2.64e-2	2.4e-4	-	-	-	-
a_{DoD}	2.88e-1	7.3e-1	1.23e-2	2.982e-2	8.95e4	-4.72e-5	4.83e-4	5.2e-5
b_{DoD}	7.95e-1	6.79e-1	7.162e-1	4.904e-1	-4.86e-1	9.62e-5	2.38e-5	6.8e-1
c_{DoD}	0	-1.61e1	-	-	-7.28e-4	-	-	-1.6e1
a_{SoC}	-	-	-1.94e-2	-	1.04e1	-	-	-
a_{crate}	-	-	-	-	2.63e-1	-	-	-
a_T	-	-	4e-3	-	6.93e-2	3.62e-3	-	-

b_T	-	-	1.705e-2	2.717e-2	-	-1.05e-1	-	-
c_T	-	-	-		-	1.93	-	-
a_n	-	-	0.5e-1	0.5e-1	-	-	-	-

In Figure 5.3, the reviewed cycling ageing models are compared, calculating the maximum number of cycles $N_{cycle\ max}$ that a battery can perform before reaching the EoL criterion; all models' fitting coefficients for different batteries are considered for Li-ion technology. The primary models presented in this paragraph are distinguished by continuous lines with a distinct marker from the others [44,95,99,100,103], while the same marker distinguishes those based on these models, but proposing divergent fitting coefficients, with a dotted line [101,105]. The adoption of a logarithmic scale on the y-axis is of particular significance, given the substantial discrepancy in predictions observed among various models.

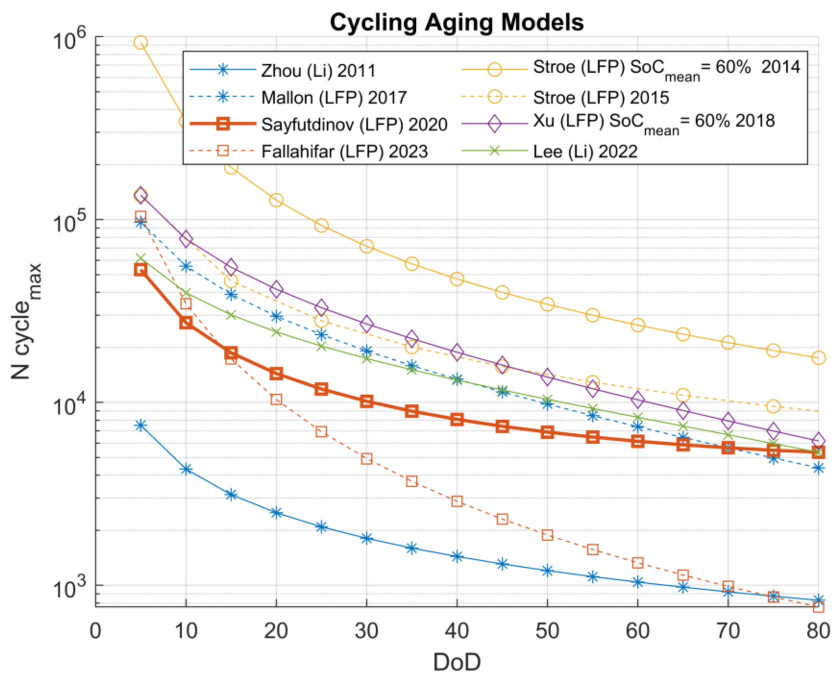

Figure 5.3: Maximum number of cycles at fixed operating conditions, as a function of the main operating parameter DoD.

Only for the Stroe et al. models [96,98,99], the progressive number of cycles has a nonlinear impact on degradation; that is, the first cycles have a higher degradation rate than the last cycles, which is not directly represented in the figure. To plot the relative curve, $N_{cycle\ max}$ is calculated numerically, through Equation 5.5, for different DoD assuming

C-rate equal to 1, temperature equal to 25 °C, and an intermediate value of SoC_{avg} equal to 60%. Xu et al., Stroe et al., Sayfutdinov et al., and Fallahifar et al. [103–105] also report an analysis of the calendar degradation model in the same work; these references allow for consistency of models as they refer to the same lithium-ion battery energy storage technology and are reviewed in detail by the subsequent section 5.3.

5.3 Calendar ageing process

The calendar ageing of the battery energy storage system is a natural consequence of the chemical degradation of its components. This phenomenon is attributable to collateral reactions that are initiated by the thermodynamic instability of the constituent materials [98]. The thermodynamic stability of the negative electrode is pivotal, given that graphite is not electrochemically stable when used with most electrolyte types. The investigation of calendar ageing in the open literature is, as a general rule, less extensive than that of cycling. Nevertheless, it is essential to incorporate this effect into a proper model if the BES is to be subjected to long periods of idling in order to assess the degree of capacity degradation.

Stroe et al., Sayfutdinov et al., and Fallahifar et al. posit that the key parameter is idling SoC, and concur that high SoC has a detrimental effect. The aforementioned points are summarised in Table 5.2. While Xu et al. [95,102] established that the capacity fade is dependent on the SoC, exhibiting a symmetrical exponential trend with respect to 50%. This suggests the presence of a non-monotonic trend, which implies an optimal SoC (50%) that minimises calendar ageing during idling periods.

In the context of the impact of temperature on calendar capacity fade, the research conducted by Stroe et al. [96,98,99] and Xu et al. [95,102] consistently demonstrates an exponential dependence. In contrast, Sayfutdinov et al. [103,104] and Fallahifar et al. [105] observe a second-order dependence. The proposed models differ in terms of their temporal dependency. While models [102,104,105] propose a linear relationship, the dependence indicated by Stroe [98] reports a power law dependence with an exponent equal to 0.8, thereby affirming that calendar degradation slows down progressively over time.

Equation 5.20 describes the Stroe et al. model, whilst Equation 5.21 offers a description of the Xu et al. model for the linearised time degradation function [95]. Finally, Equation 5.22 explains the Sayfutdinov et al. and Fallahifar et al. models [103,105].

$$C_{fade_{idling}} = (a_T \cdot e^{b_T \cdot T} + c_T) \cdot (a_{SoC} \cdot e^{b_{SoC} \cdot SoC} + c_{SoC}) \cdot t^{a_t} \tag{5.20}$$

$$f_{calendar} = a_t \cdot e^{a_{SoC} \cdot (SoC - SoC_{ref})^2} \cdot e^{a_T \cdot (T - T_{ref}) \cdot \frac{T_{ref}}{T}} \cdot t \tag{5.21}$$

$$C_{fade_{idling}} = (a_{SoC} \cdot SoC^2 + b_{SoC} \cdot SoC + c_{SoC}) \cdot (a_T \cdot T^2 + b_T \cdot T + c_T) \cdot t \tag{5.22}$$

Figure 5.4 illustrates the trends associated with the revised calendar ageing models. By calculating, fixing the temperature at 25°C, the maximum lifetime t_{max} that can be achieved before the battery reaches the EoL criterion, as outlined in Equation 5.7, the results can be determined.

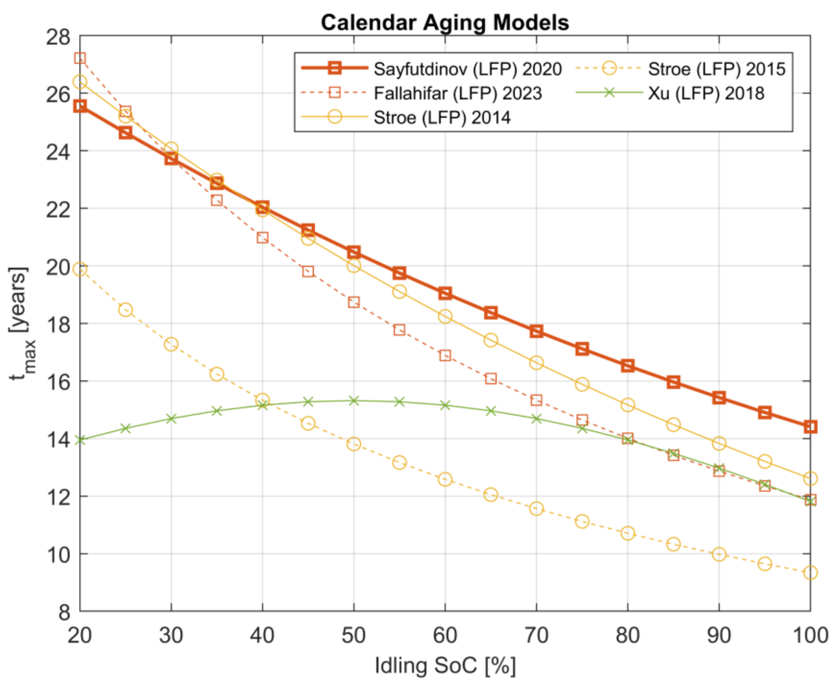

Figure 5.4: Lifespan at fixed idling conditions for the battery energy system, as a function of the idling State of Charge (SoC)

The x-axis, in Figure 5.4, displays the SoC at which the battery is maintained over the years. It can be observed that Xu et al. [95,102] have proposed a non-monotonic model, with a maximum for average SoC equal to 50%. Xu's model is comparable to the other models in that it exhibits a high average SoC idling period. However, for low SoC, it differs significantly, demonstrating a more cautious approach in terms of lifespan expectancy. In a manner analogous to the process of cycling ageing, the Xu curve t_{max} was evaluated for varying levels of SoC through numerical integration of Equation 5.7, with T set at 25°C.

As illustrated in Table 5.4, the coefficients for the models under discussion are presented, thus facilitating a more straightforward comparison between different models for the reader. It is imperative to consider whether the coefficients are fitted for percentage SoC or dimensional values in different works. As posited by the other models, it is always advisable to maintain the battery at a low state of charge in order to reduce the rate of degradation over time. With regard to the models of cycling, the same logic is employed to visualise the aforementioned models: continuous lines are used for the original models [44,95,98,100,103], while dotted lines are used for the same models but revised with different coefficients [101,105]. It is imperative to emphasise that the definition of models is subject to variation amongst authors, with different time units being utilised. This discrepancy can impede the process of comparing models, as it complicates the establishment of a uniform framework for evaluation. In this study, the objective is to facilitate a more robust comparison between the calendar capacity fade models and the hourly time unit. This approach enables the determination of the idle cost per hour.

Table 5.4:The fitting coefficient for each calendar ageing model

Constant	[95,102,106]	[96,98,99]	[108]	[103,104]	[105]
a_{SoC}	1.04e1	1.639e-1	1.9e-2	6.02e-6	4.34e-6
b_{SoC}	-	7.38e-3	8.23e-1	1.35e-5	2.73e-5
c_{SoC}	-	-	5.195e-1	1.85e-5	1.45e-5
a_T	6.93e-2	1.977e-11	3.258e-9	2.31e-3	-
b_T	-	7.51e-2	5.087	-4.01e-2	-
c_T	-	-	2.95e-1	-1.21	-
a_t	1	8e-1	8e-1	1	1

5.4 Advanced ageing cost functions

The purpose of this section is to illustrate how ageing and efficiency are considered within the optimisation stage. In order to take into account the degradation cost associated with capacity fade due to cycling and idling, ad hoc cost functions are defined. As demonstrated in Equations 5.23 and 5.24, these functions express the cost associated with each unit. That is to say, the cost is expressed in terms of a cycle for cycling ageing and an idling hour for calendar ageing. In order to provide a representation of the impact of the degradation model on costs, the cost of the system was simplified using the specific Capital Expenditure (CAPEX) cost.

$$Cost_{cycle}(DoD) = \frac{CAPEX}{N_{max}(DoD)} \quad \left[\frac{€}{cycle}\right] \qquad 5.23$$

$$Cost_{calendar}(SoC) = \frac{CAPEX}{t_{max}(SoC)} \quad \left[\frac{€}{hour}\right] \qquad 5.24$$

Figure 5.5 and Figure 5.6 illustrate non-linear cost functions for cycle cost and idle cost.

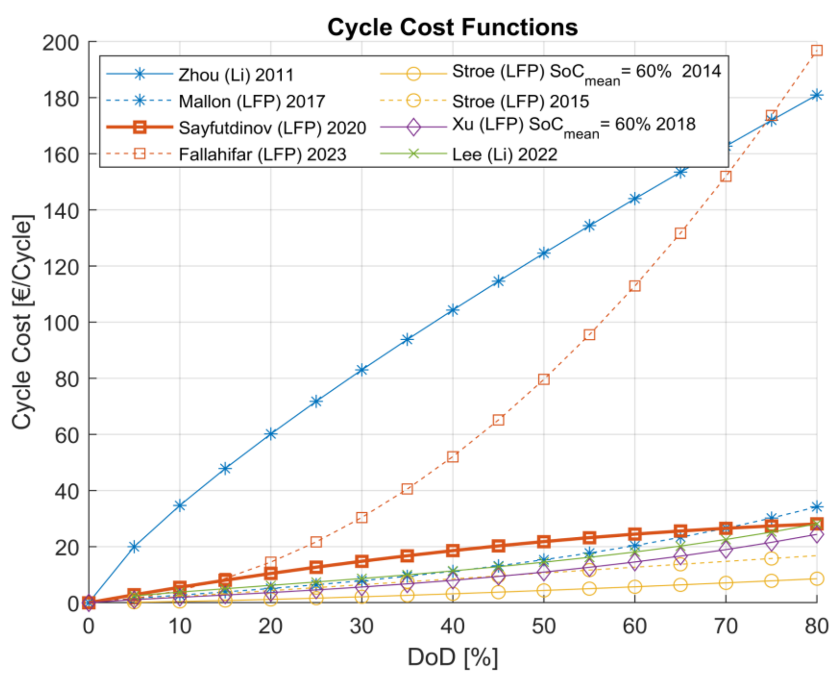

Figure 5.5: Cycle cost associated with each specific cycle [87].

In order to calculate the cycle cost and the calendar degradation cost, the CAPEX was considered to be equivalent to 150 k€/MWh [109] and the nominal capacity of 1 MWh.

As illustrated in Figure 5.5, the cycle cost is obtained according to the model reviewed in Section 5.2, utilising the same technical assumptions employed for the plotting of Figure 5.3. The Zhou et al. [100] and Fallahifar et al. [105] models are characterised by the highest cycle cost, indicating that the technology employed in the experimental campaign exhibits elevated levels of degradation performance.

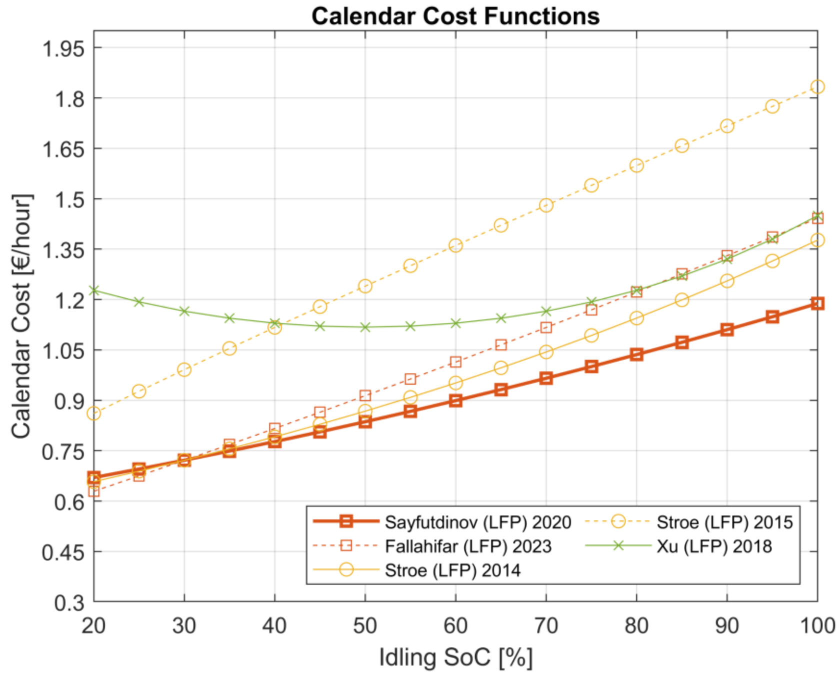

Figure 5.6: Calendar cost associated with each specific idle hour[87].

Analogously, in Figure 5.6. The calendar cost is expressed, for the models reviewed in Section 5.3, as a function of idling SoC, with the same technical assumptions made to plot Figure 5.6. The model proposed by Stroe et al. [96,99] has highlighted a greater impact of calendar degradation, having a higher idling cost.

It is evident that, given the non-linear nature of the cost functions in question, a rudimentary MILP model would be inadequate in handling them. However, by discretisation of the functions in question, it becomes possible to manage such problems with MILP methodology, particularly in the context of arbitrage. The operation of the battery is modelled through a discrete ΔSoC, where each time step allows one admissible transition between an initial and a final SoC. The transitions in question are represented in matrix form and selected through binary decision variables. The objective coefficients encompass operational profits, charging/discharging efficiencies, electricity prices, and degradation costs associated with each SoC variation and idle state. In order to achieve maximum profitability, it is imperative to incorporate these costs into the optimal dispatching strategy. However, the complexity of the situation is exacerbated when there is an absence of potential profit generation. This cost modelling approach carries with it the risk of limiting operations and reaching the system EoL criterion for calendar ageing[86,87].

Chapter 6

On Board EMS

The present chapter explores the expanding environmental repercussions of maritime transportation, which remains predominantly reliant on fossil-fuel-powered Internal Combustion Engines [110]. In recent decades, there has been a substantial increase in the emissions from shipping, including CO_2, NOx, SOx, and CO. According to the International Maritime Organisation (IMO), there is a potential for CO_2 emissions to rise by up to 130% by 2050 in comparison with 2008 levels [111]. In this context, the enhancement of onboard energy systems and the integration of low-carbon technologies have become imperative to reduce emissions and enhance overall efficiency [112,113].

The present study focuses on developing an optimisation framework to support the design and operation of ship energy systems. In particular, a MEDO tool can identify the most suitable combination of technologies to install on board and determine their optimal operating schedule. The optimisation is driven by demand, with the primary objective being to satisfy the vessel's electrical and thermal energy demands at minimum cost, while adhering to all technical and operational constraints.

The model encompasses both capital expenditures (CAPEX) and operational costs (OPEX), thereby facilitating a comprehensive techno-economic evaluation of disparate technology configurations. In the course of the analysis, particular attention is given to Battery Energy Storage Systems (BES), which have been demonstrated to play a key role in increasing system flexibility, enabling load shifting, and reducing fuel consumption and emissions [114–116]. The optimisation framework determines the optimal operational parameters for each component, including generators and storage systems, to ensure the most efficient and cost-effective utilisation of resources to meet demand.

The study is applied to a real case study of a cruise ship operating in the Baltic Sea, using realistic electrical and thermal demand profiles. This facilitates the evaluation of disparate technology combinations and operational strategies under pragmatic conditions. The work demonstrates how advanced optimisation tools can support the transition towards more sustainable maritime energy systems by enabling the integration of innovative technologies and improving onboard energy management.

6.1.1 Demands and energy system layout

The demand data under consideration refer to the thermal and electrical consumption of a real cruise ship sailing between Stockholm and the island of Åland in the Baltic Sea. The vessel was constructed in 2004 and possesses a passenger capacity of 1,800, a design speed of 21 knots, a length of 176.9 metres, a beam of 28.6 metres, and a draught of 6.5 metres [117]. The identification of five typical days was facilitated by comprehensive data analysis and energy-demand clustering. The period under consideration is considered representative of the electricity and heat demands of a ship of a similar size. The ship's mission profile was considered. The propulsive energy demand is incorporated into the electrical load, accounting for fully electric propulsion. As illustrated in Figure 6.2, the electrical and thermal loads for each typical day are represented. The typical day is observed on a recurring basis throughout the year, with the respective amounts documented in Table 6.1.

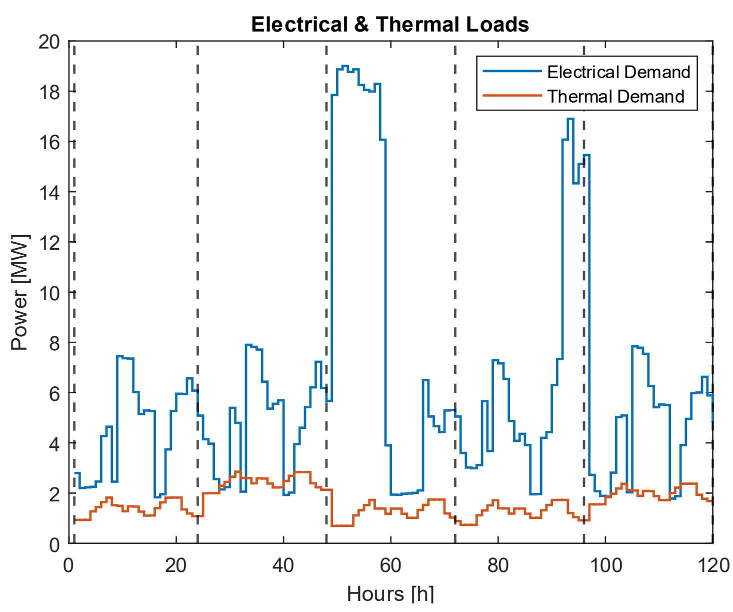

Figure 6.1: Electrical and thermal demands, for 5 clustered days [117].

The table reports the peak demands for electrical and thermal energy, along with the number of days on which they occur each year. The number of typical days is then used as a weight within the optimisation model defined in MEDO. The optimiser identifies the energy mix capable of satisfying these loads while minimising the objective function (overall costs, including capital expenditure, operational expenditure and carbon dioxide costs).

Table 6.1: Electrical and thermal demand characteristics.

	Max Electrical Demand [MW]	Max Thermal Demand [MW]	Number of days
Typical day 1	7.5	1.8	57
Typical day 2	7.9	2.9	19
Typical day 3	19	1.7	25
Typical day 4	17	1.7	148
Typical day 5	7.8	2.4	116

Figure 6.2 presents a simplified diagram illustrating the ship's onboard energy flow. This diagram has been simplified by omitting intermediate components such as electric motors and inverters, as they are considered part of the internal combustion engine's efficiency chain. To account for the overall energy transformation efficiency of 95% from mechanical to electrical power, the propulsive demand is adjusted accordingly. The objective of this optimisation model is to ensure compliance with the two constraints in order to meet energy demands.

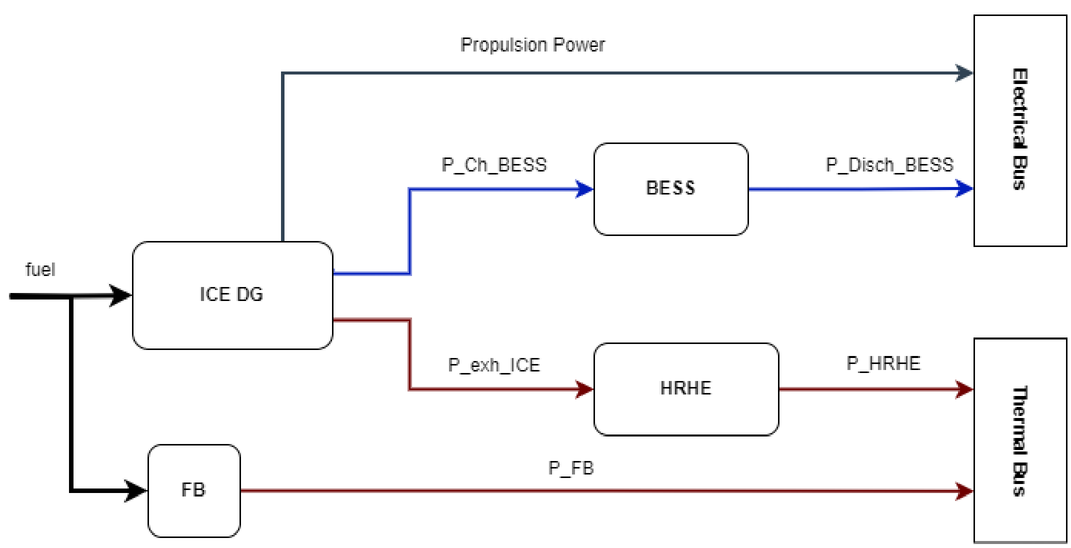

Figure 6.2: Power flow diagram for the case study HE cruise ship [118,119].

In order to ascertain the optimal solution, the optimiser takes the technologies reported in Table 6.2. Internal combustion engines (ICEs) provide both propulsion and electrical power, while heat recovery from exhaust gases (HRHEs) and fired boilers (FBs) meet the thermal demand by recovering waste heat from DG exhaust gases and producing heat via direct combustion, respectively. BESs are charged via ICE DGs and discharged on the ship's electrical bus as required.

Table 6.2: Characteristics of the power system components.

Component	ID of item	Max Power [kW] or Rated Capacity [kWh][a]	Efficiency [-]	Reference	No. of items installed (Selected by the optimiser)
ICE DG	A	7500	Variable with load (PWL)	[120]	2
	B	11930	Variable with load (PWL)	[120]	1
HRHE	A	1000	0.85	[121]	1
	B	1500	0.9	[121]	1
FB	A	1500	0.9	[122]	1
	B	970	0.9	[123]	1
BES	A	990[a]	0.95	[124]	1
	B	3725[a]	0.95	[125]	1
	C	1970[a]	0.94	[126]	1
	D	960[a]	0.93	[127]	0

6.1.2 Objective function

The calculation of both cost functions is based on the typical days presented in the section 6.1.1. The objective cost function, Ω, is to be minimised. It is reported as the sum of Ω_{TCE} (Eq. 6.1), Ω_{CO2} (Eq. 6.2) and Ω_{HFO} (Eq. 6.3).

The Ω_{TCE} (Total Cost of Equipment) comprises the capital expenditure required for the acquisition of each i_{th} energy system (CAPEX) and the cost of fuel consumed by it, C_{HFO}, over the year. The cost of HFO is thought to be 0.53 € per kilogram [33], and it is assumed to be constant throughout the year. The financial implications of CO_2 emissions in Ω_{CO2} are determined by an emission factor (EF_{HFO}), which is defined as the mean mass of carbon dioxide produced by the combustion of a unit quantity of HFO, multiplied by the fuel consumption m[128] and the prevailing carbon tax rate C_{CO2}. The EF for HFO is assumed to be 3.15 kg_{CO2}/kg_{HFO} [129] while the carbon tax is assumed to be 100 €/ton_{CO2} [130].

$$\Omega_{TCE} = \sum_{i=1}^{S} (CAPEX_i \, N_i) \tag{6.1}$$

$$\Omega_{CO2} = (\dot{m}_{HFO}^{tot} \, \Delta t \, C_{CO2}) \, EF_{HFO} * 1000 \tag{6.2}$$

$$\Omega_{HFO} = \dot{m}_{HFO}^{tot} \, \Delta t \, C_{HFO} \tag{6.3}$$

6.1.3 Results and discussion

In this chapter, the results of the MILP optimisation model are presented, demonstrating the effectiveness of the proposed approach in identifying a stable and reliable solution. The optimisation process converged within approximately 140 seconds, at which point a residual value lower than 0.3% was achieved. This confirmed the model's numerical robustness and accuracy. As illustrated in Figure 6.3, the optimal electrical dispatch schedule is required to meet the ship's energy demand.

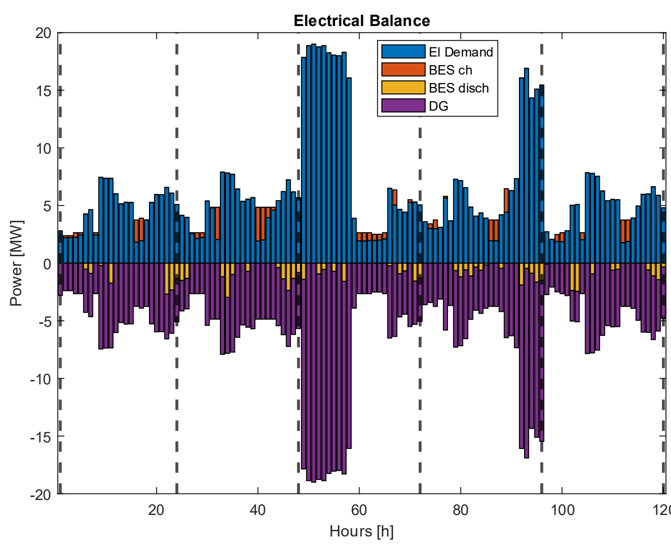

Figure 6.3: Electrical demand and optimal overall electrical energy balance.

The findings indicate that the bulk of onboard electricity is generated by Internal Combustion Engine (ICE) generators, while the contribution of the Battery Energy Storage System (BES) remains modest but strategically important. The primary function of the battery is to support peak demand and enhance system flexibility. Specifically, the maximum battery discharge is observed at the 10th hour of the second typical day, reaching 2.97 MW, which corresponds to approximately 38% of the peak electrical demand (7.9 MW). Conversely, the maximum charging power is observed at the 16th hour, reaching 2.93 MW, which exceeds the instantaneous demand (152%), indicating that surplus generation is effectively stored for later use.

The Figure 6.4 reports the optimal scheduling of thermal energy supply for typical-day operation.

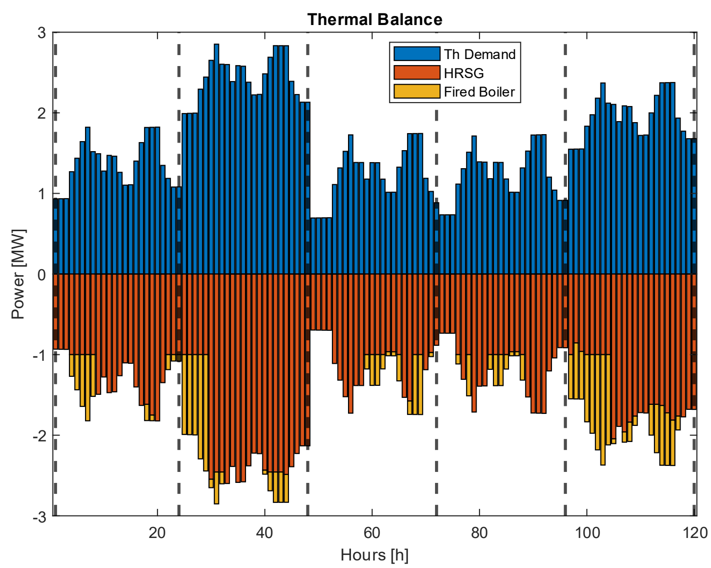

Figure 6.4: Thermal demand and optimal overall thermal energy balance.

The majority of the thermal demand is satisfied through Heat Recovery Heat Exchangers (HRHE) due to the high availability of waste heat from ICE generators. The optimisation model successfully prioritises this highly efficient operating condition, thereby maximising the utilisation of recovered heat and reducing the need for additional fuel for thermal generation. The results obtained demonstrate the efficacy of the MEDO framework in coordinating electrical and thermal energy flows, thereby enhancing system efficiency and reducing operational costs.

The maximum thermal power provided by the auxiliary FB is 1.44 MW, occurring at the 5th hour of a typical day 2, contributing 59% to the overall thermal demand in that hour. It is important to note that the high share of FB thermal power in the initial hours of the day can be attributed to the limited power generation capacity of the ICEs (see Figure 6.3). This, in turn, reduces the exhaust mass flow, thereby diminishing the thermal recovery potential.

As illustrated in Figure 6.5, the optimised operating strategy of the Battery Energy Storage System (BES) encompasses both the power profiles and the State of Charge (SoC) evolution, with a detailed breakdown of the contribution from each battery pack. The findings underscore a coordinated utilisation of the storage system, with the largest battery pack (BES_2, with a capacity of 3.73 MWh) predominantly responsible for the majority of energy exchange, particularly during periods necessitating sustained charging or discharging. In contrast, the smaller battery packs are primarily utilised to manage short-term fluctuations and power peaks, operating with more dynamic charge–discharge cycles and higher ramp rates. This differentiated utilisation enables the system to balance both energy and power requirements efficiently.

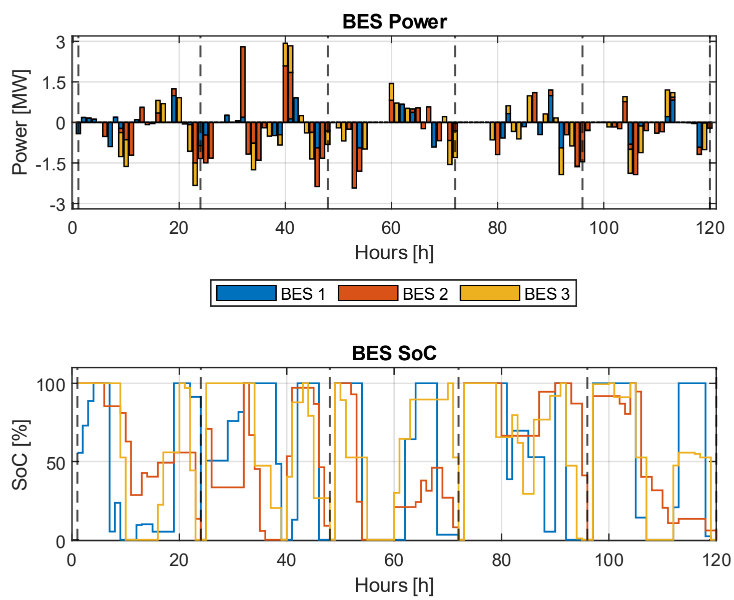

Figure 6.5: BES optimal power allocation and SoC.

As demonstrated in Figure 6.6, there is a clear delineation between the thermal demand of Heat Recovery Heat Exchangers (HRHE) and Fired Boilers (FB). HRHE A is observed to operate close to full load for the majority of the time, while HRHE B is activated during periods of higher thermal demand. In accordance with prior observations, the utilisation of fired boilers is contingent upon the recovery of insufficient heat from the ICE generators, a scenario that arises particularly when these operate at part load and are unable to supply adequate thermal energy. This behaviour corroborates the optimisation strategy, which prioritises waste heat recovery over additional fuel consumption, thereby enhancing overall system efficiency.

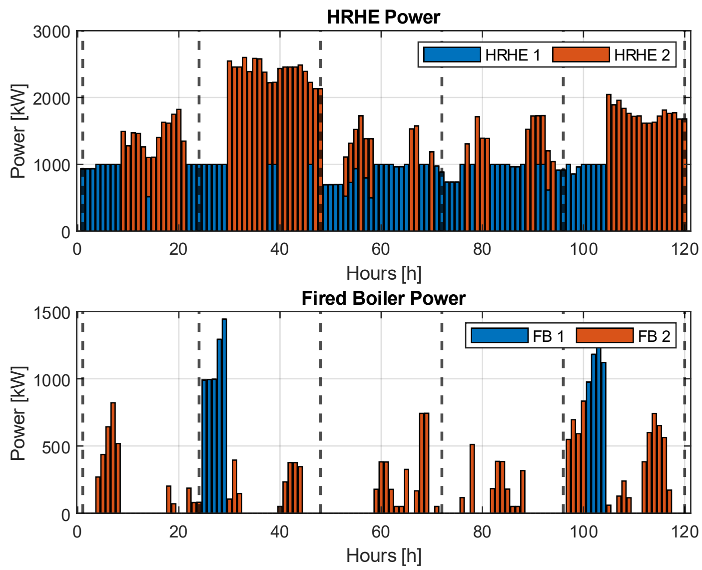

Figure 6.6: HRHE and FB optimal thermal power allocation.

Finally, Figure 7 quantifies the environmental benefit of integrating the BES into the system. The findings suggest a reduction of over 20 tons of CO_2 emissions over the course of five typical days of analysis, corresponding to approximately a 5% decrease in comparison with a configuration based on internal combustion engines (ICE). On an annual basis, this equates to a reduction of approximately 1,450 tons of CO2, thereby demonstrating the significant potential of energy storage systems in lowering emissions and enhancing the sustainability of maritime energy systems.

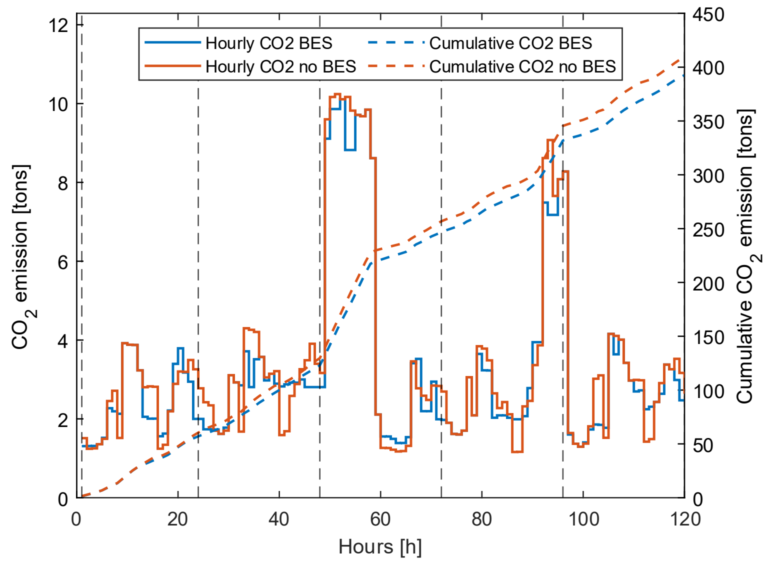

Figure 6.7: Trend of hourly CO2 emission and cumulative savings over the whole mission.

The Table 6.3 illustrates the various contributions from the objective function for the traditional configuration devoid of batteries, in addition to a more flexible solution that incorporates on-board battery installation. As can be seen, when all contributions are taken into account, there is a slight reduction in costs.

Table 6.3: Objective function values in the optimised case.

	Fuel Cost DG	Fuel Cost FB	Fuel Cost TOT	CO_2 Cost DG	CO_2 Cost FB	CO_2 Cost TOT	BES SoC_i Cost	CAPEX	Total Obj Value
With BESS [M€]	4.84	0.13	4.97	2.79	0.07	2.86	0.03	0.66	8.52
No BESS [M€]	4.88	0.13	5.01	2.81	0.08	2.89	0.00	0.68	8.58
Variation	-0.76%	-3.73%	-0.84%	-0.76%	-3.73%	-0.84%	100%	-3.22%	-0.66%

Chapter 7

EMS for Remote Island

This chapter presents two analyses conducted to evaluate the performance of MEDO in the context of demand-driven systems. In such systems, the presence of multiple energy sources makes the problem significantly more complex in terms of managing and defining optimal dispatch. The MEDO framework is based on a Mixed-Integer Linear Programming (MILP) formulation, which allows for the representation of both continuous operational variables and discrete decisions associated with system operation.

Remote and islanded systems present a particularly critical case, as they often rely on imported fossil fuels for electricity generation while facing limited infrastructure and constrained resource availability. In such environments, the transition toward hybrid energy systems that combine conventional generation units with renewable technologies is an important step toward reducing fuel consumption, operational costs, and environmental impact. At the same time, these systems can be expanded to support the production of additional energy vectors, such as hydrogen and fresh water. This enables a multi-vector energy approach that increases system flexibility and resource efficiency. Hydrogen production is an increasingly viable solution for medium- and long-term energy storage, particularly for applications where seasonal storage is necessary to offset the temporal discrepancy between renewable energy production and demand. As well as its role as an energy carrier, hydrogen can also contribute to decarbonising sectors with significant non-electrical energy demand, such as transportation. However, the production of hydrogen necessitates substantial amounts of fresh water, which could pose a significant challenge in remote or arid regions characterised by limited water resources [131,132].

Consequently, desalination technologies have become increasingly important for supporting sustainable development in water-scarce regions and isolated islands. The most widely adopted desalination technologies are Reverse Osmosis (RO) and Multi-

Stage Flash (MSF), which convert seawater into fresh water for residential, industrial and agricultural applications. The integration of desalination systems with renewable-based energy systems and energy storage technologies enables the development of integrated infrastructures capable of simultaneously producing electricity, hydrogen, and fresh water. The optimal management of such complex systems requires advanced modelling and optimisation tools capable of capturing the interactions between multiple energy vectors and technologies.

7.1 EMS for electrical demand, Ikaria Island

The deployment of renewable energy sources assumes greater significance in the context of decentralised and non-interconnected island grids. In such scenarios, the generation of electricity is often associated with elevated costs, primarily attributable to factors such as fuel supply, infrastructure development, operational expenses, and maintenance requirements. In such contexts, conventional generation technologies become less economically attractive, while RES emerge as a more cost-effective and sustainable alternative. A number of studies have demonstrated the merits of integrating RES into island energy systems [133,134]. For instance, hybrid wind-diesel and PV-wind-diesel configurations have been shown to significantly reduce both operational costs and CO2 emissions, highlighting the economic and environmental advantages of renewable integration in isolated grids [135]. However, the high penetration of intermittent energy sources, such as solar photovoltaic (PV), can also introduce operational challenges. These include reduced efficiency of conventional generators due to part-load operation and the need for increased system flexibility . In this regard, previous analyses have demonstrated that smaller, more flexible generation units, such as ICEs, may exhibit superior overall system efficiency in comparison to larger gas turbines, despite the higher capital costs associated with the former [136].

In this research, the optimal transition pathway towards higher RES penetration in an islanded energy system is investigated, with a specific focus on the case of Ikaria Island. The system under scrutiny comprises conventional ICE generators integrated with renewable energy sources, including PV, Wind Turbine, and pumped hydro storage. The primary objective of this study is to evaluate the most effective strategy for managing the integration of renewable energy into an existing grid. Secondly, the study aims to assess the MEDO tool's capacity to address large-scale problems, with only one demand profile that has to be managed.

7.1.1 Energy system layout and grid security requirements

The Ikaria's electrical energy demand, which is managed by the internal energy system, experiences fluctuation between 2 MW and 8 MW during different periods of the year. As illustrated in Figure 7.1, the distribution of the island's electricity demand is characterised by the first and third quartiles of 2.57 MW and 3.7 MW, respectively.

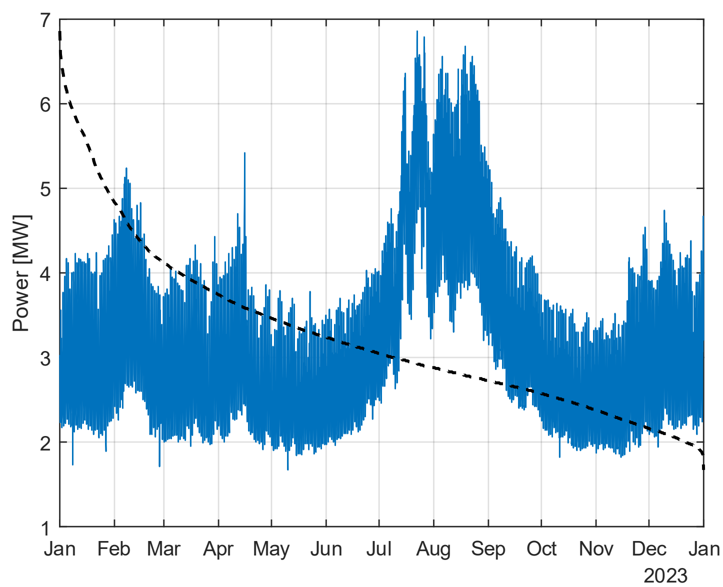

Figure 7.1: Ikaria Island annual electrical demand distribution.

The demand profile shows seasonality, with a higher peak in demand during the summer months. The median demand is 3.04 MW, with a annual average of 3.25 MW. The Figure 7.2 shows the configuration of the modelled electrical grid system. The network has been modelled as a single bus, with all components connected to ensure electrical balance. The system illustrated in Figure 7.2 is the one currently operational at the Ikaria island, thus serving as the baseline scenario. In order to furnish a more general overview, it is evident that the capacity of renewable energy sources has been subject to continuous variation within a specific range, to asses the system behaviour. Moreover, the significance of comprehensive flexibility in the management of pumped-storage hydroelectricity has been emphasised, as it substantially mitigates the intermittent nature of renewable energy sources.

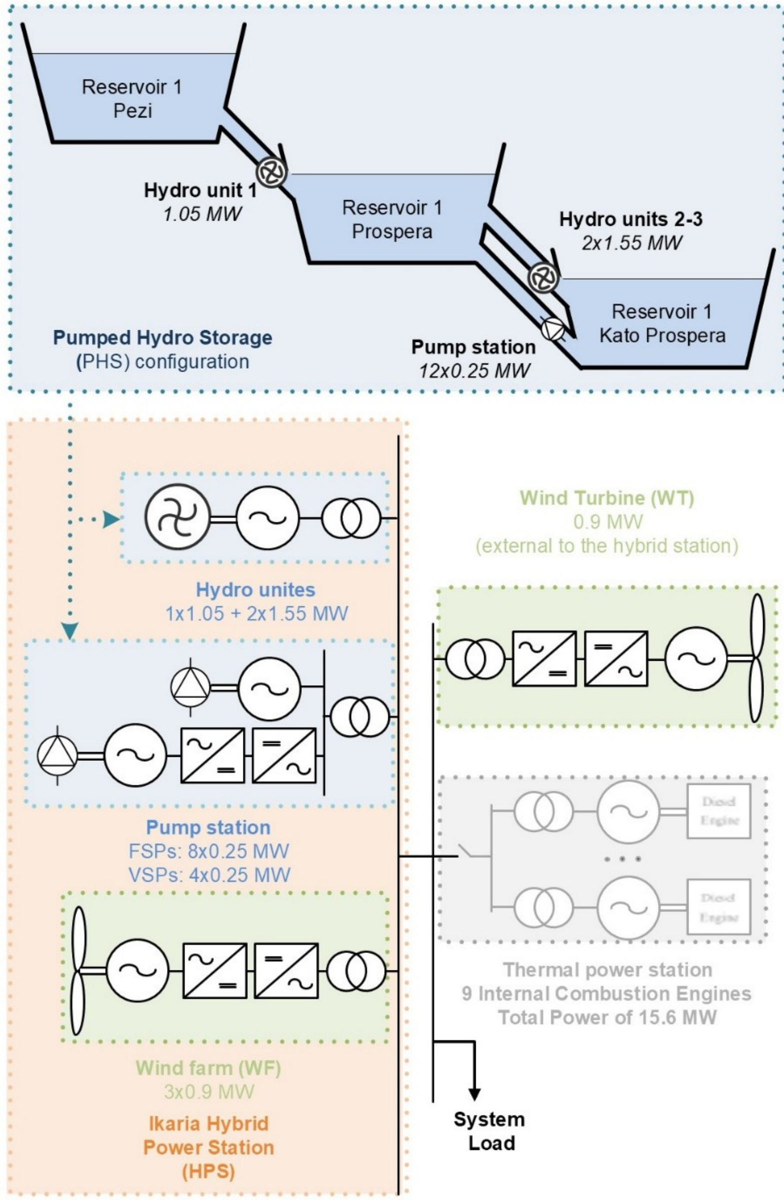

Figure 7.2: Ikaria island state of the art system configuration [137].

In Table 7.1 and Hydro units 1 and 2 have a rated power of 1.55 MW each and are used for the PHS system. The pumping station, located at Kato Proespera, comprises eight fixed-speed pumps (FSPs) of 250 kW each, controlled by a soft starter, and four Variable-Speed Pumps (VSPs) of 250 kW each. The VSPs are prioritized for operation, while the minimum pump load is 50%, equivalent to 125 kW. When wind potential is available, the WT and pumping station operate in tandem to pump and store water as hybrid energy in the reservoirs. This process effectively converts intermittent wind energy into stored hydraulic energy, which is then used to generate hydroelectric power to meet the demand load. Further details of the system components can be found in [92,137].

Table 7.2, the off-design curves are reported for the main production units of the Ikaria grid [137,138]. These off-design curves were used to develop the MILP model of the Ikaria Island power system. The respective generation facilities include a conventional Autonomous Local Fuel Power Station (ALFPS) consisting of 9 heavy fuel oil (mazut/diesel) ICE with a total capacity of 15.6 MW. The system has a total installed WT capacity of 3.6 MW, divided into two wind plants of 0.9 MW and 2.7 MW. The most flexible component is the PHS, which consists of three reservoirs, two-generation power stations with hydraulic turbines with a total output power of 4.6 MW, and a pumping station at the lowest reservoir with a total absorbed power of 3 MW. Reservoir 1 (Pezi) is a natural reservoir with a total capacity of 900,000 m3. The hydroelectric unit for this reservoir can be used only in winter and spring; only a surplus of water is used for power generation, while in summer, the reservoir is used only for irrigation and water supply. The actual PHS plant is composed of Reservoir 2 (Proespera) and Reservoir 3 (Proespera Kato), with a capacity of 80,000 m3 each. These two reservoirs are hydraulically connected by a double penstock system, ensuring that generation and pumping operations remain independent for higher operational flexibility.

Table 7.1: ICE off-design performance used for the MEDO tool [137].

ALFPS	SFOC gr/kWh			Efficiency [%]			Power [kW]		
Load	50%	75%	100%	50%	75%	100%	50%	75%	100%
ICE_1	235.7	226.5	224.3	36.80	38.30	38.67	1750	2625	3500
ICE_2	235.7	226.5	224.3	36.80	38.30	38.67	1750	2625	3500
ICE_3	235.7	226.5	224.3	36.80	38.30	38.67	1450	2175	2900
ICE_4	245.4	225.8	220.9	35.35	38.42	39.27	1100	1650	2200
ICE_5	255	239	237.5	34.02	36.30	36.53	375	562.5	750
ICE_6	255	239	237.5	34.02	36.30	36.53	375	562.5	750
ICE_7	255	239	237.5	34.02	36.30	36.53	375	562.5	750
ICE_8	255	239	237.5	34.02	36.30	36.53	375	562.5	750
ICE_9	267.5	252.6	246	32.43	34.34	35.26	375	562.5	750

Hydro units 1 and 2 have a rated power of 1.55 MW each and are used for the PHS system. The pumping station, located at Kato Proespera, comprises eight fixed-speed pumps (FSPs) of 250 kW each, controlled by a soft starter, and four Variable-Speed

Pumps (VSPs) of 250 kW each. The VSPs are prioritized for operation, while the minimum pump load is 50%, equivalent to 125 kW. When wind potential is available, the WT and pumping station operate in tandem to pump and store water as hybrid energy in the reservoirs. This process effectively converts intermittent wind energy into stored hydraulic energy, which is then used to generate hydroelectric power to meet the demand load. Further details of the system components can be found in [92,137].

Table 7.2: PHS off-design performance used for the MEDO tool [137].

PHS Plant	Mass Flow Rate [m^3/h]			Efficiency [%]			Power [kW]		
N°	10%	50%	100%	10%	50%	100%	10%	50%	100%
HT	136.2	627.3	1235.1	82.0	89.0	90.4	150	750	1550
HP	153.0	791.1	1610.4	70.9	73.3	74.6	300	1500	3000

To highlight the impact of the new renewable capacity integration into the system, Reservoir 1, located in Pezi, was neglected, as it only provides energy for a specific period, and its operation is prioritized for irrigation and water supply needs. In the developed model, only Reservoir 2 and Reservoir 3 were considered for the PHS. Thus, the optimiser respected the operational and security constraints of the network. For the electricity grid security and operational continuity, it is necessary to introduce two constraints related to the minimum baseload guaranteed by programmable load technologies. These two constraints are formulated in Eq. 7.1 and Eq. 7.2. The first constraint requires a minimum amount of energy to be supplied by ICE at each optimisation hour. Based on historical data acquired within the EU SINNOGENES project (Sinnogenes, 2023), the C_1 value was set at 20%. The second constraint defines a minimum required energy that must be provided by both the ICE and the Hydro Turbines intended for use in the Pumped Hydro Storage (PHS); based on historical data, it has been observed that the C_2 value should be at least 60%. The optimisation is conducted for a year, with hourly granularity.

$$SR_1 = \frac{E_{ICE_t}}{E_{D_t}} \cdot 100 \geq C_1 , \forall\, t \in [1, 8760] \tag{7.1}$$

$$SR_2 = \frac{E_{ICE_t} + E_{HT}}{E_{D_t}} \cdot 100 \geq C_2 , \forall\, t \in [1, 8760] \tag{7.2}$$

To evaluate the impact of the system's performance with an increased capacity of renewable energy for Ikaria Island a two-scenario sensitivity analysis was defined for varying the installed capacity of photovoltaic panels and wind turbines; the capacity values considered for the sensitivity analysis are presented in Table 7.3. For scenario 1, with no PHS considered, three variations of SR_2 were considered (20%, 40% and 60%), as this parameter has a strong impact on the curtailment levels and RES penetration. For the second scenario, with PHS included, the analysis included only the WT and PV installed capacity, with SR_1 and SR_2 set to 20% and 60%, respectively.

Table 7.3: Wind and Photovoltaic installed capacity.

Parameter	RES Installed Capacity [MW]								
Wind	0	0.4	1	2	3	4	5	6	7
Photovoltaic	0	1	2	3	3.6	4	5	6	7

7.1.2 Comparison Metric Definition

Four KPIs have been introduced to compare different scenarios of installed RES capacity. The KPIs characterize the electricity grid for different shares of renewable energy. These include two technical indicators ($E_{RES}\%$ and $E_c\%$), one economic indicator (*LCOE*), and one environmental indicator (SCI).

The RES share ($E_{RES}\%$) indicator quantifies the share of total electrical Energy Demand (E_D) met by renewable energy sources, specifically WT and PV systems, for the scenario without PHS (i.e. Scenario 1), while for Scenario 2, the $E_{RES}\%$ also takes into account the energy provided by PHS, as charging energy is provided by the RES excess. In Eq.7.3, the actual E_{RES} consumption is calculated as the difference between the total electrical energy demand E_D and the total electrical energy supplied by the ICE (E_{ICE}) weighted by the total E_D for the entire year.

$$E_{RES}\% = \frac{\sum_{t=1}^{8760}\left(E_{D_t} - E_{ICE_t}\right)}{\sum_{t=1}^{8760} E_{D_t}} \cdot 100 = \frac{\sum_{t=1}^{8760} E_{RES_t}}{\sum_{t=1}^{8760} E_{D_t}} \cdot 100\ [\%] \qquad 7.3$$

The RES Curtailment ($E_c\%$) indicator evaluates the grid's ability to absorb the available renewable energy, highlighting the extent to which excess energy from RES cannot be utilized due to system constraints. The RES curtailment is calculated in Eq. 7.4 as the difference between the available renewable energy and the actual renewable energy used, weighted by the total RES energy available throughout the year.

$$E_c\% = \frac{\sum_{t=1}^{8760}\left(E_{RES_t}^{available} - E_{RES_t}\right)}{\sum_{t=1}^{8760} E_{RES_t}^{available}} \cdot 100\ [\%] \qquad 7.4$$

The Levelized Cost of Electricity (*LCOE*) is an economic indicator that compares different scenarios based on their financial impact. For this assessment, only the CAPEX of the newly installed RES capacity is considered, as conventional technologies are already in place. In Eq. 7.5, the Capital Recovery Factor (CRF_k) is defined for the WT and (PV) systems; i_{rate} is the interest rate equal to 5%, n is the useful life span of each system (n_{WT} 27 years; n_{PV} 25 years). The specific capital cost for the WT was considered to be 1.11 M€/MW and for the PV panels, 0.56 M€/MW [139]. CRF_k coefficient enables the total CAPEX investment costs to be annualized, allowing for a consistent assessment of both system operating costs OPEX and investment costs on the same time basis. The *LCOE*, i.e., the specific cost of electricity, taking into account the total annual costs, is given in Eq. 7.6.

$$CRF_k = \frac{i_{rate} \cdot (1 + i_{rate})^n}{(1 + i_{rate})^n - 1} \qquad 7.5$$

$$LCOE = \frac{\sum_{t=1}^{8760}\left(OPEX_{ICE_t}\right) + CRF_{WT} \cdot CAPEX_{WT} + CRF_{PV} \cdot CAPEX_{PV}}{\sum_{t=1}^{8760} E_{D_t}} \left[\frac{€}{MWh}\right] \qquad 7.6$$

Specific Carbon Intensity (*SCI*) is an environmental indicator that measures the specific CO_2 emissions to provide a unit of energy. The Specific Carbon emission reduction is related to the ability to substitute traditional fossil fuel production with renewable energy, as defined in Eq. 7.7. Due to the Safety Grid Requirement (SR_1 and SR_2), there is a limitation on the achievable maximum reduction.

$$SCI = \frac{\sum_{t=1}^{8760} CO_{2_t}}{\sum_{t=1}^{8760} E_{D_t}} \left[\frac{ton}{MWh}\right] \qquad 7.7$$

7.1.3 Optimal Dispatch Profile

Prior to the presentation of the KPIs' results, Figure 7.3 and discussed to highlight the operational dispatch profiles. The example given is based on a total RES installed capacity of 6 MW, comprising 3 MW of wind turbines and 3 MW of photovoltaic panels.

As illustrated in Figure 7.3, he negative y-axis denotes demand and charging from pumped hydro storage, while the positive y-axis indicates ICE, RES production, and discharging from pumped hydro storage. The black line on the y-axis indicates the total demand for electricity and charging energy of PHS. Should the available RES exceed the line, the energy will be curtailed without the possibility of storage for subsequent periods. As illustrated in Figure 7.3 the conditions for low and high RES production are clearly delineated, facilitating comprehension of the system's operation throughout the year of optimisation. The figure illustrates that even in circumstances where RES production is high, it is essential to maintain the minimum base load of ICE in order to adhere to security requirement SR1 of 20%. In the high RES scenario, especially on the 19th and 20th of February, the system operates the pumped hydro plant to its maximum capacity in order to reduce the amount of electricity produced by the ICE modules, thereby minimising the total annual cost of generation.

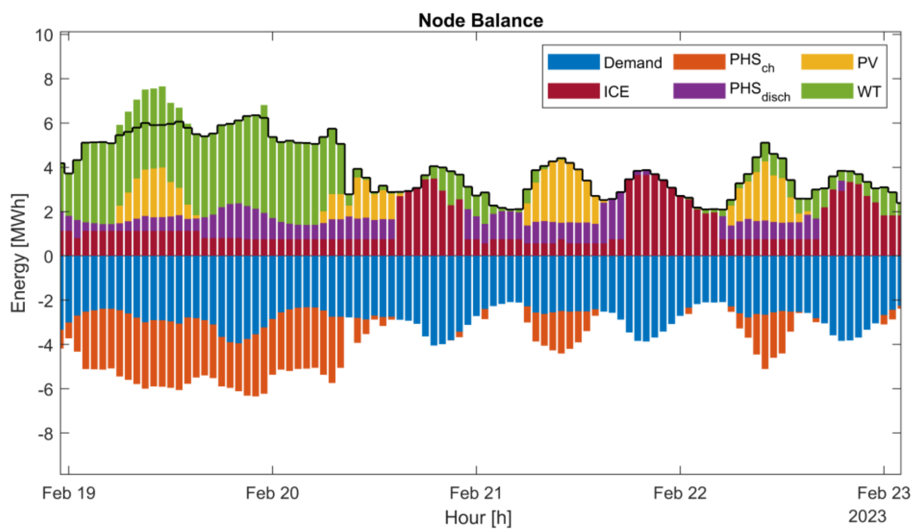

Figure 7.3: Example of dispatch in Scenario 2 (with PHS): Electrical hourly energy balance for the Ikaria Island Grid, with a total RES capacity installed of 6 MW (3 MW of Wind Turbines and 3 MW of Photovoltaic Panels).

On 19 February at noon, there was excess high-RES energy that the pumping station was unable to absorb, resulting in a curtailment. On days where there is not much wind, the system will increase the amount of energy it gets from the ICE, starting from the afternoon of 20 February. The planned pumped storage facility will play a pivotal role in enhancing the utilisation of renewable energy sources (RES), minimising energy wastage, and augmenting RES production. The PHS system comprises two pipelines. One is used exclusively for the discharge phase, and the other is used for the charging phases. This configuration enhances flexibility by dividing the two phases. Security requirements SR_2

have necessitated the implementation of this solution, despite its energy inefficiency due to round-trip efficiency. The stability of the grid is prioritised over energy optimisation.

7.1.4 Techno-economic and Environmental results

The following section presents and discusses the results using the KPIs defined in the previous section. First, technical parameters such as RES share ($E_{RES}\%$) and RES curtailment ($E_c\%$) are presented. These parameters are evaluated in relation to both the installed capacity and the potential annual energy of WT and PV. Next, the economic parameter Levelized Cost Of Electricity ($LCOE$) is analysed, also taking into account the level of curtailment, as this represents an inefficiency in the system's ability to absorb the total renewable potential. Finally, the discussion focuses on the evolution of the environmental parameter, Specific Carbon Intensity (SCI), once again taking into account curtailment levels.

Figure 7.4 presents the RES share ($E_{RES}\%$) as a function of the installed capacities of WT and PV, while RES curtailment ($E_c\%$) levels are represented as contour lines in red to improve readability. The black line facilitates the determination of the optimal installed capacity of WT and PV to ensure a given RES share with the least curtailment. From Figure 7.4, it can be observed that for high SR_1 values in Scenario 1, there are significant challenges in increasing RES share, leading to a sharp rise in curtailment levels. In the worst-case scenario (Figure 7.4a), the maximum $E_{RES}\%$ reaches 35%, while $E_c\%$ is 75%. By reducing SR*1* values, it is possible to achieve a maximum RES share of 65% and $E_c\%$ of 52.5%, ensuring lower security requirements (Figure 7.4c). In Scenario 2 (Figure 7.4d), the significant benefits of PHS can be observed, as it helps maintain security constraints at actual working levels while improving RES integration, reducing the RES curtailment strongly. It is worth noting that in Scenario 2, for a capacity range of 3 MW of WT nominal installed capacity to 4.5 MW of PV nominal installed capacity, the curtailment is less than 1%, ensuring a maximum RES penetration of 50%. This indicates a system capable of efficiently absorbing all renewable production. For a 3 MW WT capacity, it can be seen that a RES share value of 50% can be achieved. However, to exceed this threshold while minimizing $E_c\%$, a significant amount of PV capacity needs to be installed. A more balanced distribution between the two installed capacities is then restored. The maximum $E_{RES}\%$ is 70%, while in that condition the minimum $E_c\%$ is 35%.

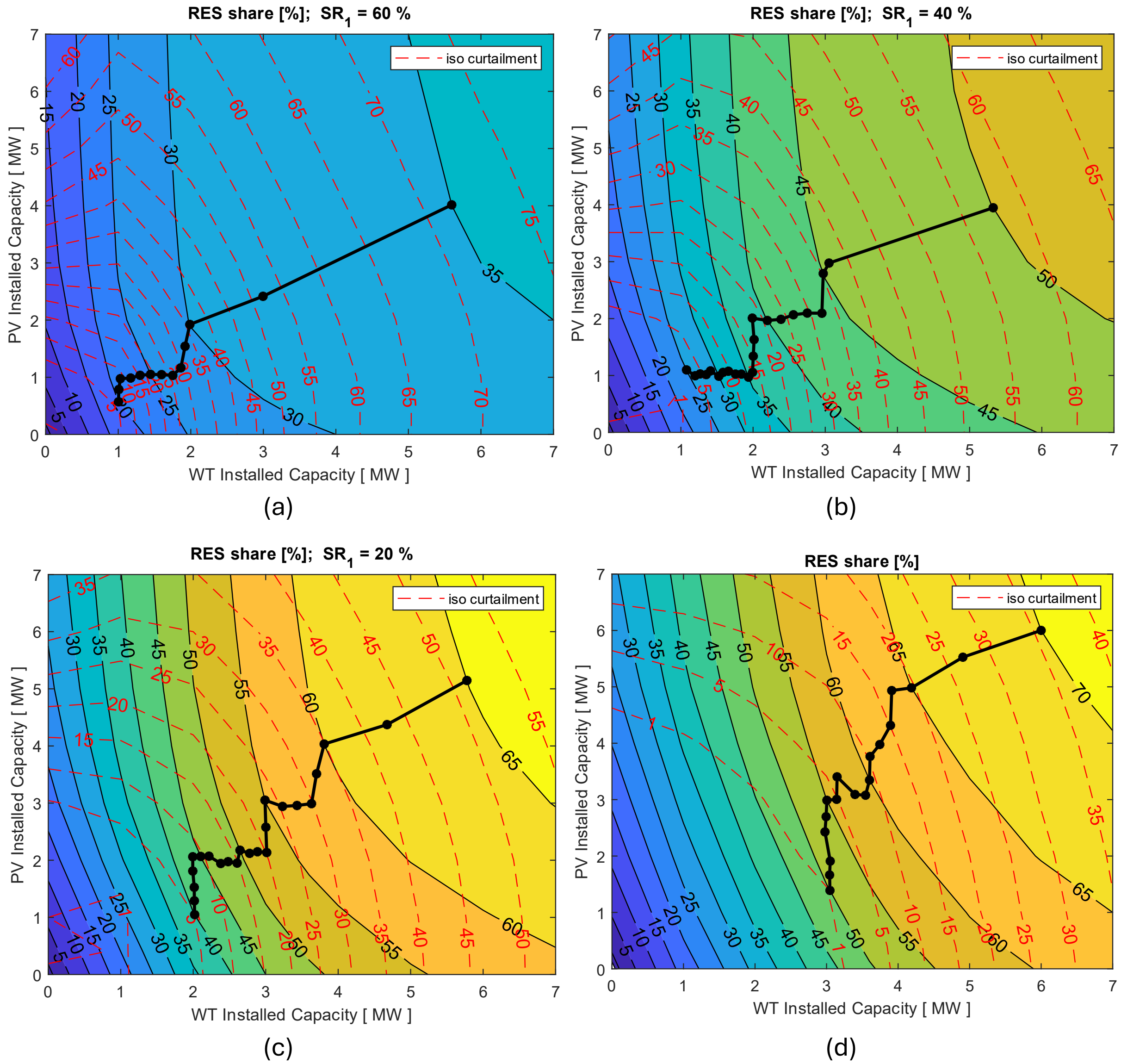

Figure 7.4: Renewable Energy Sources Share and iso-Curtailment levels for different Installed Capacities levels for Wind Turbines (x-axis) and Photovoltaic panels (y-axis). (a-c) Scenario 1 SR1 (60%, 40% and 20%), (d) Scenario 2 SR1 20%; SR2 60%.

It can be noticed that at the beginning of stable curtailment occurrence (5% for Scenario 1 and 1% for Scenario 2), the optimal ratio between installed WT and PV capacity is approximately 2. This effect is mainly due to longer operating hours (the WT are producing 90% of the hours vs 50% of the PVs) and a higher capacity factor of up to 57% vs 20% more than compensating for the higher CAPEX. When curtailment starts, the addition of capacity is shared among WT and PV, with a still not completely clear saw-tooth pattern. When the curtailment grows, the contribution of the PV capacity increases up to roughly a 1:1 ratio. In fact, under high curtailment conditions, the decoupling effect between the production profiles of the two different RES sources becomes predominant over time.

The Figure 7.5 illustrates the trends for RES share and RES curtailment, but this time as a function of the annual renewable energy potential. This visualisation clearly shows that small variations in installed WT capacity lead to significantly higher energy production. Hence, increasing the installed PV capacity is less beneficial under certain conditions, as its capacity factor is much lower, up to 20%, due to the inherent nature of the energy source. When a stable curtailment is achieved, the production from the WT in the ideal condition is up to 5 times the PV one. It can be seen that the reduction of the backup grid requirements and the use of PHS in Scenario 2 allows an increase in the amount of energy produced by the PV panels as a result of the storage mitigating the peak shaving effect.

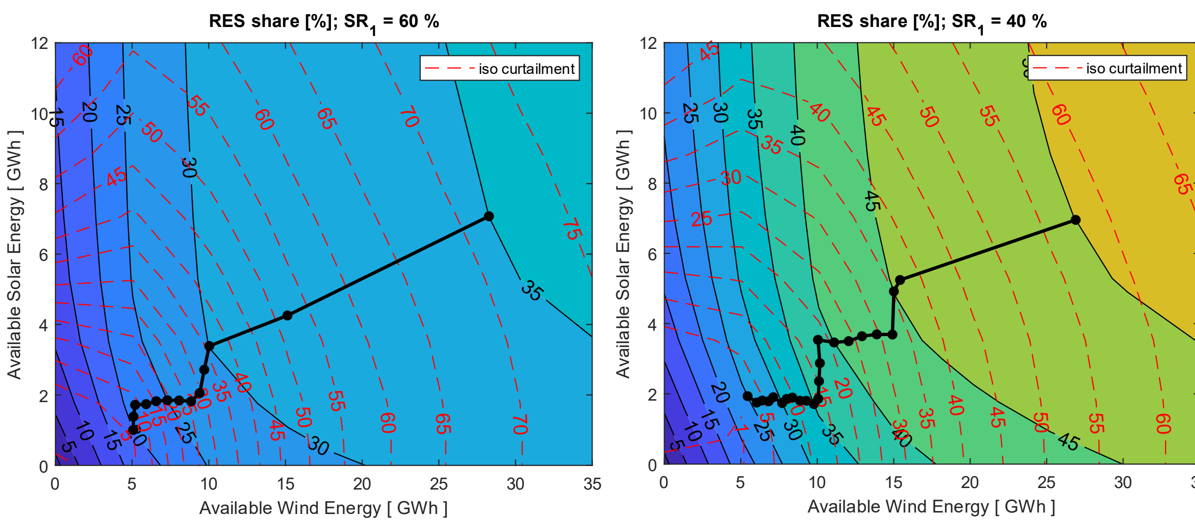

(a) (b)

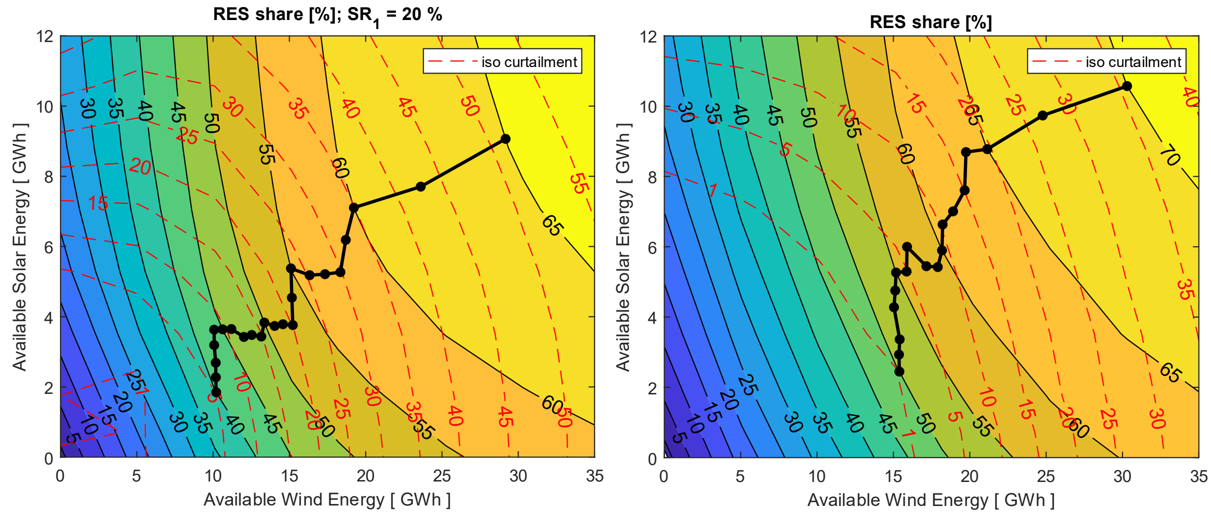

(c) (d)

Figure 7.5: Renewable Energy Sources Share and iso-Curtailment levels for different Available Energy for Wind Turbines (x-axis) and Photovoltaic panels (y-axis). (a-c) Scenario 1: SR1 (60%, 40% and 20%), (d) Scenario 2: SR1 20%; SR2 60%.

As illustrated in Figure 7.6 the Levelized Cost of Electricity ($LCOE$) demonstrates clear trends within the range of installed renewable energy (RES) capacity investigated. As expected, compared to an LCOE of 150 €/MWh when only ICEs are adopted, the introduction of the RES generators with their lower nominal $LCOE$ has a beneficial effect. When curtailment becomes significant, the resulting $LCOE$ from RES starts growing since the additional CAPEX is not compensated by a proportional production.

It is important to note that a curtailment limit of around 55% is observed in all scenarios. This means that, beyond this limit, increases in the share of RES are no longer economically viable. This is due to the fact that the higher initial investment costs outweigh the benefit of the additional RES share.

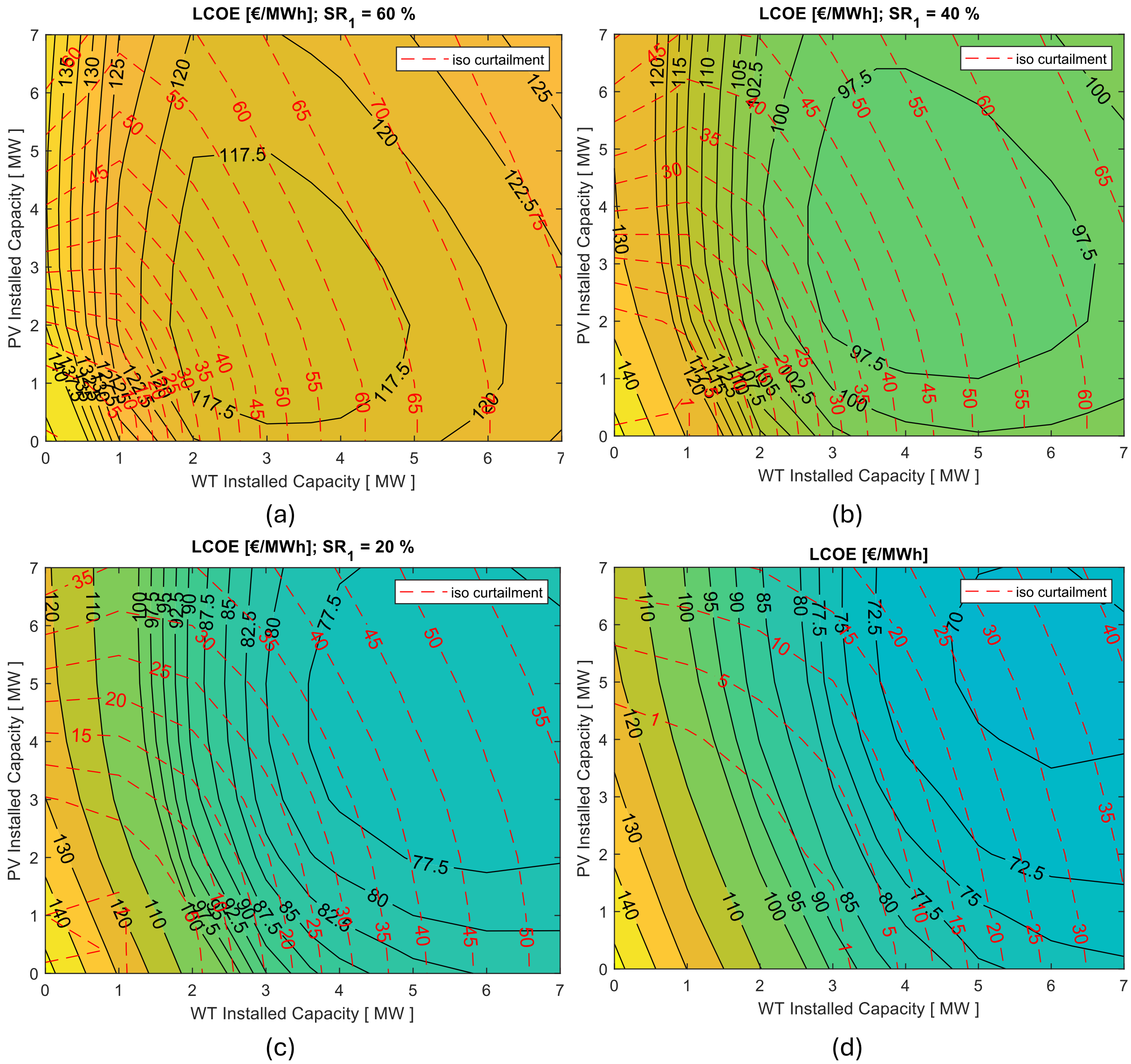

Figure 7.6: Levelized Cost Of Electricity (LCOE) and iso-curtailment levels for different Installed Capacity for Wind Turbines (x-axis) and Photovoltaic panels (y-axis). (a-c) Scenario 1: SR1 (60%, 40% and 20%), (d) Scenario 2: SR1 20%; SR2 60%.

In Scenario 1 Figure 7.6 a-c, the maximum achievable *LCOE* reduction is limited to about 21% for highest SR_1 due to the low flexibility capability of the system to manage periods of excess RES production For the lowest SR_1, the maximum reduction is significant, reaching up to 48%, but comes with a substantial reduction in reserve capacity.

In contrast, Scenario 2 (Figure 7.6d) achieves a significant reduction in $LCOE$, from a maximum of 150 €/MWh in the absence of RES to 70 €/MWh at maximum installed capacity, a reduction of 53%. This significant reduction results from the fact that the PHS plant is already in place, and no additional investment is required. It is noted that, despite lower security in Scenario 1 with SR_1 = 20%, results close to those of Scenario 2 can be achieved if only $LCOE$ is considered, with a difference of approximately 7.75 €/MWh. This difference is entirely attributable to the system's reduced capability to absorb RES production peaks, resulting in higher curtailment levels.

Figure 7.7 presents the fourth indicator considered, namely the Specific Carbon Intensity (SCI). SCI is represented within the domain of installed RES capacities. In Scenario 1, with no RES capacity installed, emissions reach almost 700 kg/MWh, primarily due to ICEs operating at an average efficiency of around 38% [137]. Unlike the economic indicator (*LCOE*), the environmental one (*SCI*) consistently decreases by an additional installation of RES capacity because every increase in RES share reduces the capacity factor of ICEs, which in turn results in lower emissions.

With a higher SR_1 value (Figure 7.7a) and maximum installed RES capacity, SCI decreases to approximately 500 kg/MWh, representing a 28% reduction. Conversely, for minimum SR_1 (Figure 7.7c), SCI is even lower, with a reduction of around 57%.

In Scenario 2 (Figure 7.7d), a significant reduction in SCI is observed even for low installed power levels, reaching a maximum reduction of 64%. Once again, for equal WT and PV installed capacity, there is no significant variation in SCI. This is due to both the low capacity factor and the fact that PV generation is concentrated in certain time slots.

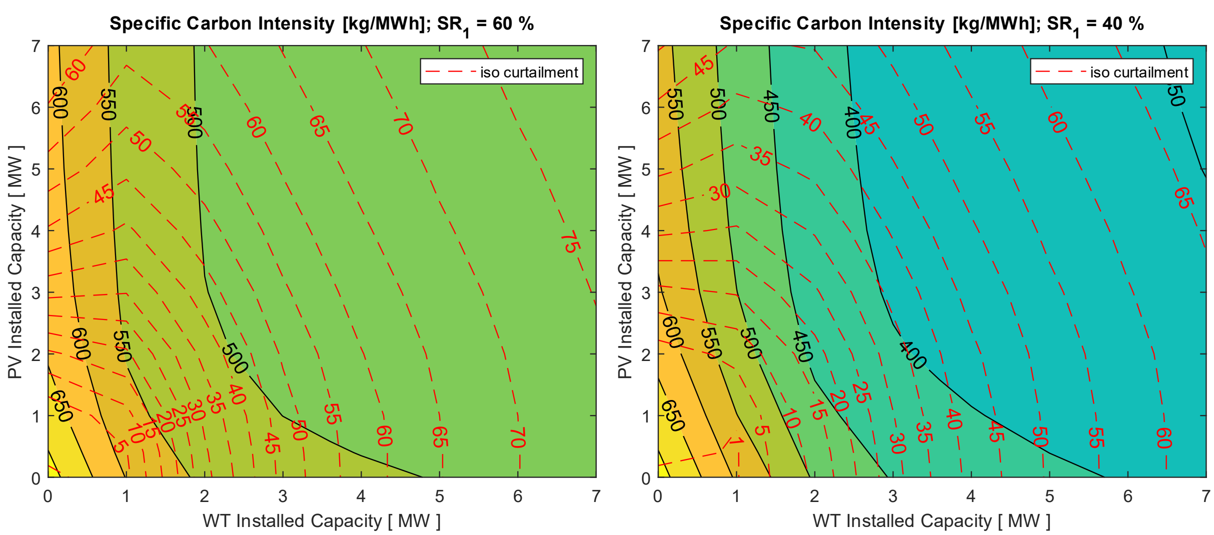

(a) (b)

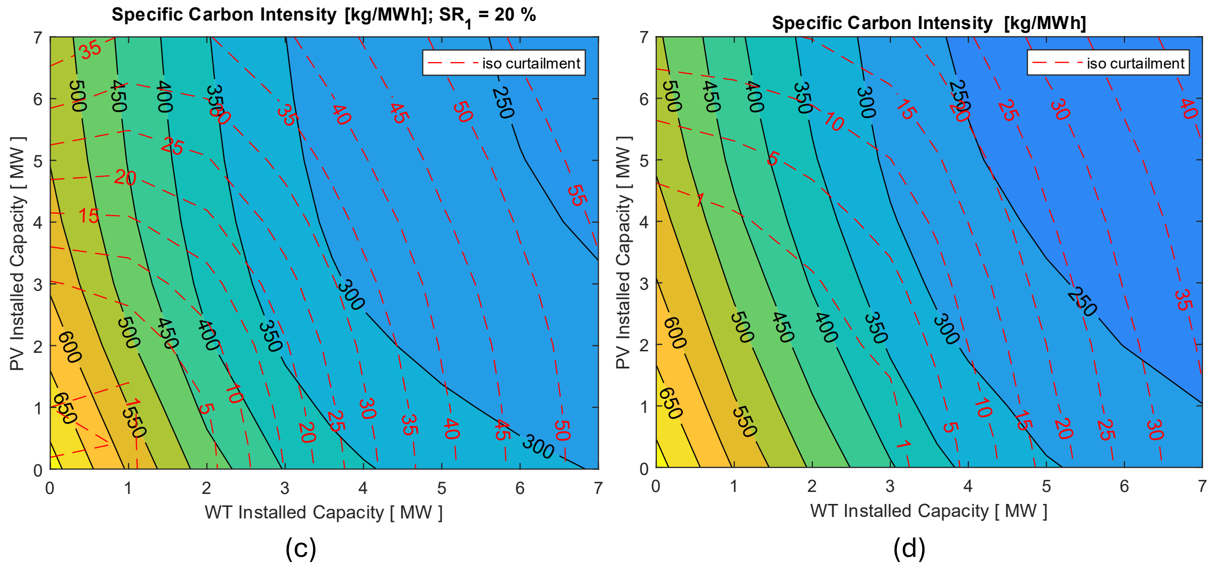

Figure 7.7: Specific Carbon Intensity and iso-curtailment levels for different Installed Capacity for Wind Turbines (x-axis) and Photovoltaic Panels (y-axis). (a-c) Scenario 1: SR1 (60%, 40% and 20%), (d) Scenario 2: SR1 20%; SR2 60%.

7.1.5 The impact of simulation window and solver capability

The objective of this section is to evaluate whether a substantial increase in the simulation window leads to a different optimal dispatch strategy and consequently to a variation in the total operating cost. Increasing the simulation window improves the accuracy of the system modelling, particularly in capturing the variability and intermittency of renewable generation. However, this enhancement does necessitate substantially elevated computational time. While extended computation times do not pose a significant challenge when conducting feasibility assessments or sensitivity analyses, simulations can require several hours to complete. Therefore, it is vital to comprehend the computational behaviour and limitations of the developed optimisation tool in order to ascertain potential strategies for reducing simulation time.

It is evident that the computational effort increases rapidly with the number of decision variables included in the optimisation problem, leading to an almost exponential increase in simulation time as model complexity increases. For the purposes of this analysis, the energy system configuration includes a PHS unit, which represents the key component enabling medium-term energy storage due to its large storage capacity and operational flexibility. The presence of PHS allows the system to effectively manage fluctuations in wind generation, making it a suitable benchmark for evaluating the impact of increased renewable penetration on the optimal dispatch solution. The considered installed wind and photovoltaic capacity for the following sensitivity analysis has been assumed 3.6 MW for both sources.

Sensitivity analyses have been performed on a PC, with Microsoft Windows 10 as OS and the following features:

- Processor: Intel(R) Core(TM) i7-10700, CPU 2.90 GHz
- RAM: 16.0 GB (15.7 GB available)
- Operating system: 64-bit, processor based on x64

The initial set of evaluation metrics analysed encompasses operating costs, RES share, and RES curtailment, all of which are contingent on the size of the simulation window. These indicators are reported in Figure 7.8 as the percentage variation relative to the reference case, corresponding to the simplest configuration with a SW equal to 24 hours. The results demonstrate that the model is highly sensitive to the optimisation horizon, with larger windows producing noticeable improvements in system performance.

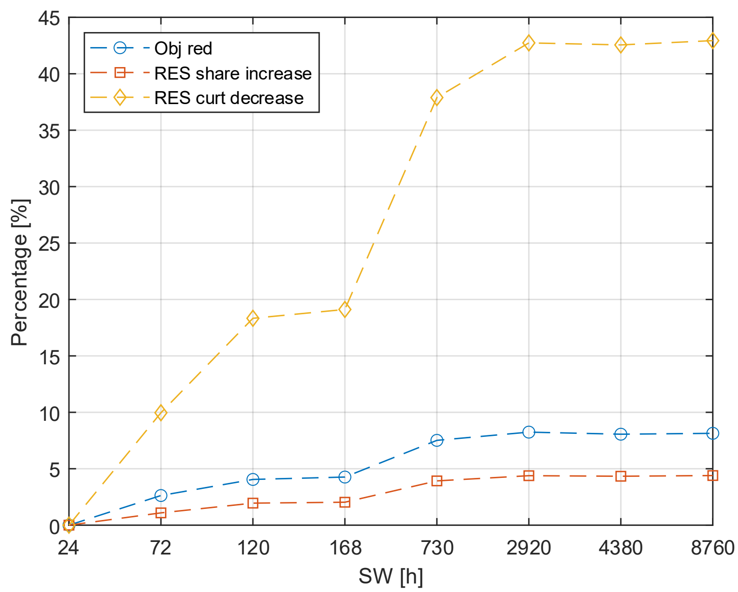

Figure 7.8: Economic and energy indicators as function of the simulation window.

In terms of operating costs, the most significant reduction is observed when the simulation window is extended to 730 hours (approximately one month), resulting in a decrease of about 7.5% compared to the reference case. A similar trend is observed for the share of renewable energy within the system, which increases progressively as the window expands. The most significant enhancement is observed when transitioning from an SW of 168 hours (equivalent to one week) to 730 hours, resulting in an approximate 4.75% increase in the RES share. Beyond a one-month timeframe, however, further increases in the simulation window will only yield marginal economic and energy benefits. A comparable behaviour can be observed for RES curtailment. The most significant reduction is evident when the window increases from 168 to 730 hours. In contrast to the previous indicators, extending the optimisation horizon further results in additional reductions in curtailed renewable energy, albeit with diminishing returns. In order to identify the most appropriate simulation window, it is necessary to balance the improvements in system performance against the corresponding computational effort. For this reason, the total computation times required to simulate the same annual period were investigate and the results are presented below.

Figure 7.9 provides a comprehensive analysis of the computational time required to perform the annual optimisation. In this context, the reported value corresponds to the total optimisation time needed to obtain the dispatch solution for the entire year. For instance, when a sliding window (SW) of 24 hours is adopted, the annual simulation is decomposed into 365 sequential sub-simulations; therefore, the total computation time equals the sum of the optimisation times of these 365 sub-problems.

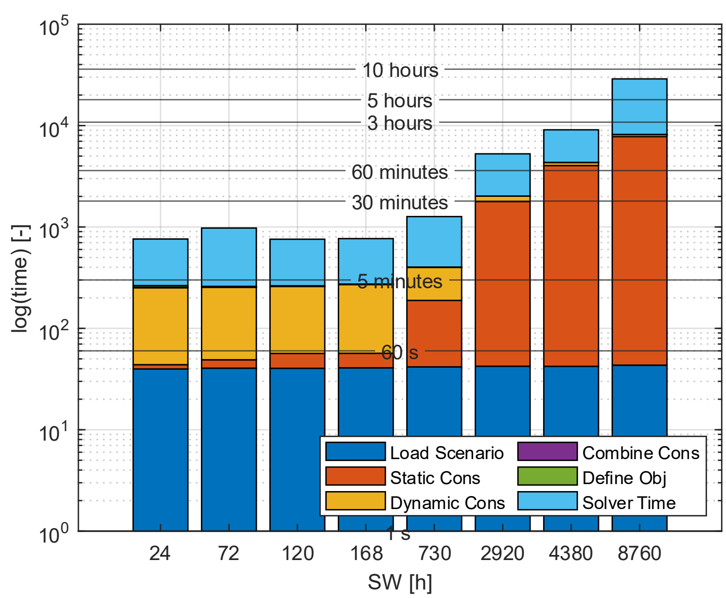

Figure 7.9: Simulation time decomposition (logarithmic y-axis) as a function of simulation window.

As shown in the Figure 7.9, where the simulation time is represented on a logarithmic scale, the overall computational effort can be divided into several phases.

The load scenario phase is the initial step in which all the necessary input data are loaded into memory. This includes demand profiles, renewable generation time series, and component interconnection. The static constraint phase represents the time required to define and store all model constraints that do not vary over time, such as component operational limits and structural interconnections between system elements. The dynamic constraint phase formulates time-dependent constraints within each sub-simulation. These include demand profiles, renewable generation availability, and market-driven problems, such as electricity prices.

The Combine Cons phase represents the time needed to assemble and concatenate all the previously defined constraints into the final optimisation problem. The next step is to define the objective function. This involves formulating and storing the objective function for each sub-optimisation instance. Finally, the solution time is the actual time the solver takes to compute the optimal solution. In this study, the optimisation problem is solved using the Gurobi solver, whose performance significantly influences the total computational time.

Firstly, it is important to note that the time required to load the input data, concatenate the constraints, and write the objective function is negligible, as these operations occur at a significantly lower order of magnitude than the other computational steps.

A thorough review of the behaviour of static and dynamic constraints indicates that the time required to formulate the dynamic equations becomes increasingly significant when the optimisation problem is decomposed into a large number of small subproblems. This is because the total time associated with dynamic constraints is proportional to the number of sub-simulations multiplied by the average time required to define the time-dependent equations for each sub-simulation. Consequently, the overall computational effort shows an approximate linear trend with the number of simulations. Conversely, the formulation of static constraints becomes more computationally demanding when larger SW values are adopted. This is because the model must handle more variables and constraints within each individual optimisation problem.

During the solver phase, solution time shows clear nonlinear growth as the simulation window increases. This behaviour is not immediately visible in Figure 7.9 due to the logarithmic scale adopted for the time axis. However, the exponential trend is much clearer in Figure 7.10, where the axis is intentionally set to a linear scale to emphasise the nonlinear increase in computational time with the simulation window size. Furthermore, Figure 7.9 shows that the write times for static constraints also exhibit nonlinear behaviour with respect to the simulation window size.

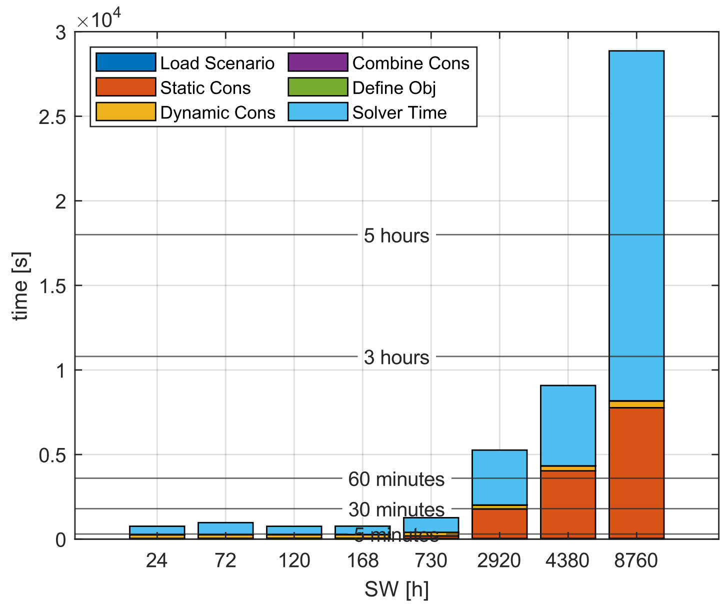

Figure 7.10: Simulation time decomposition (linear y-axis) as a function of simulation window.

Figure 7.11 shows the total simulation time and the average simulation time required for each sub-simulation as a function of the number of optimised variables. The y-axis is represented on a logarithmic scale. The figure illustrates the discrepancy between the minimum time required for a single sub-simulation and the overall time needed to complete the annual optimisation.

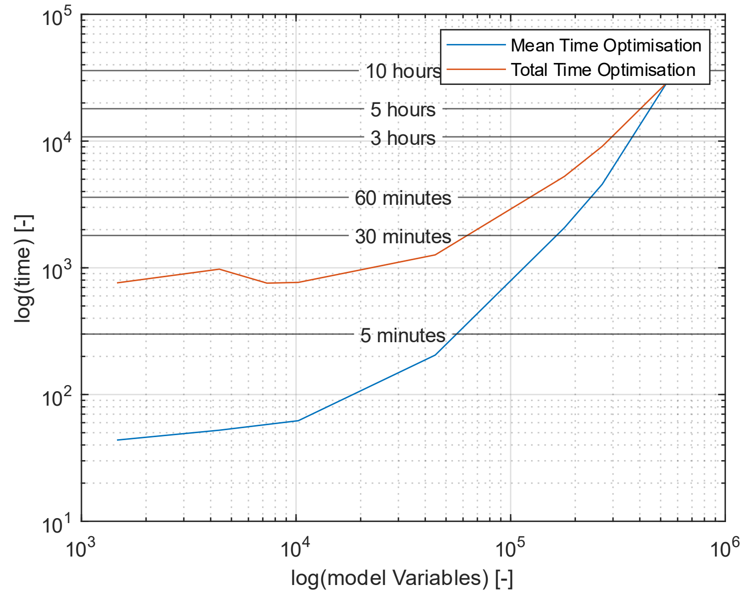

Figure 7.11: Total simulation time (logarithmic y-axis) as a function of the number of optimised variables.

For relatively short simulation windows with a maximum duration of approximately one week, the total computation time required to simulate a full year remains very limited, generally below 10 minutes. However, as the optimisation window increases, the computational time grows exponentially. It has been demonstrated that, for high simulation windows, the total simulation time required to complete the optimisation over the same annual period can reach almost 8 hours.

The findings underscore the importance of selecting an appropriate SW size that balances improvements in technical and economic performance indicators with the associated computational cost. In other words, the optimisation horizon must be sufficiently long to encompass pertinent intertemporal effects, including storage operations and renewable variability, while avoiding undue prolongation of the simulation duration. In the case of the island of Ikaria, previous analyses have demonstrated that an intermediate window size provides a satisfactory compromise between model accuracy and computational efficiency.

To conclude, the final Figure 7.12, presents a percentage breakdown of the time spent. The data show that, across all simulations, the solution time accounts for an average of 60% of the total solving time. This suggests that the solver is a critical component. Furthermore, it is important to examine the variation in the proportion of time allocated to defining dynamic and static constraints, which generally accounts for the remaining 35%.

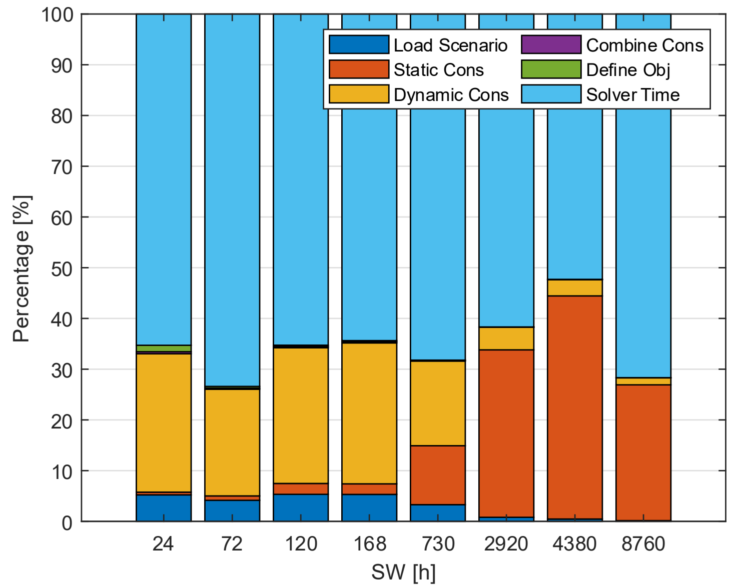

Figure 7.12: Total simulation time percentage decomposition as a function of the simulation window.

7.2 Multi-vector EMS for Ikaria Island

The present study investigates the integrated management of electricity, freshwater, and hydrogen production in isolated island energy systems. The primary objective of the study is to evaluate the capability of the Multi-Energy Dispatch Optimiser (MEDO) to simultaneously manage multiple energy demand sources and production technologies. The objective for this research is to provide sustainable and autonomous solutions for remote communities. The mismatch between renewable production and demand profiles necessitates the implementation of energy storage solutions that function across disparate temporal scales. The production of hydrogen is regarded as a potentially viable solution for the long-term or seasonal storage of energy. This approach facilitates the conversion of renewable electricity, which is typically generated in abundance during specific seasons, such as summer, into hydrogen. The hydrogen is then stored for subsequent utilisation during periods of higher energy demand. Furthermore, hydrogen has the potential to contribute to non-electrical energy sectors, such as transportation, thereby further enhancing the flexibility and resilience of the energy system [132]. However, the process of hydrogen production through electrolysis necessitates the utilisation of substantial quantities of freshwater, a factor that can prove to be a critical constraint in island environments characterised by limited natural water resources and arid climates [131]. In such contexts, desalination technologies become essential to ensure a reliable supply of freshwater for residential, industrial, agricultural, and energy-related uses. In light of this, the present sections investigates the integration of two established desalination technologies, Reverse Osmosis (RO) and Multi-Stage Flash Distillation (MSF) [140–142], within a multi-energy system that also incorporates a reversible Solid Oxide Cell (rSOC). The SOC functions as both an electrolyser for hydrogen production and a fuel cell for electricity generation.

The analysis focuses on a remote tourist island context, where strong seasonal variations in both energy and water demand occur due to the fluctuation between resident population levels and tourist inflows [143]. Demand profiles for electricity, hydrogen, and freshwater are defined on an annual basis in order to reflect realistic operating conditions. The optimisation framework determines the optimal operational strategy of the integrated system, identifying how renewable electricity should be allocated between direct consumption, desalination processes, and hydrogen production.

A sensitivity analysis is also conducted on the nominal production capacity of the desalination plants in order to evaluate how different design configurations affect overall system performance. The assessment of the various system configurations is facilitated by the employment of techno-economic indicators, such as the Levelised Cost of Electricity (LCOE) and the Levelised Cost of Water (LCOW). These indicators encompass both the costs of investment and operation.

The present work demonstrates the efficacy of a multi-energy optimisation approach in effectively coordinating different energy vectors and demand sectors within a single integrated framework. The results of the study demonstrate the efficacy of MEDO in managing complex interactions between renewable generation, energy storage, water production, and hydrogen generation. This enables enhanced system flexibility, reduced renewable curtailment, and improved sustainability for isolated island communities.

7.2.1 System Layout

The system is fundamentally designed around the utilisation of PV panels for the purpose of producing electrical energy. This energy is then used for two key purposes, as shown in the Figure 7.13.

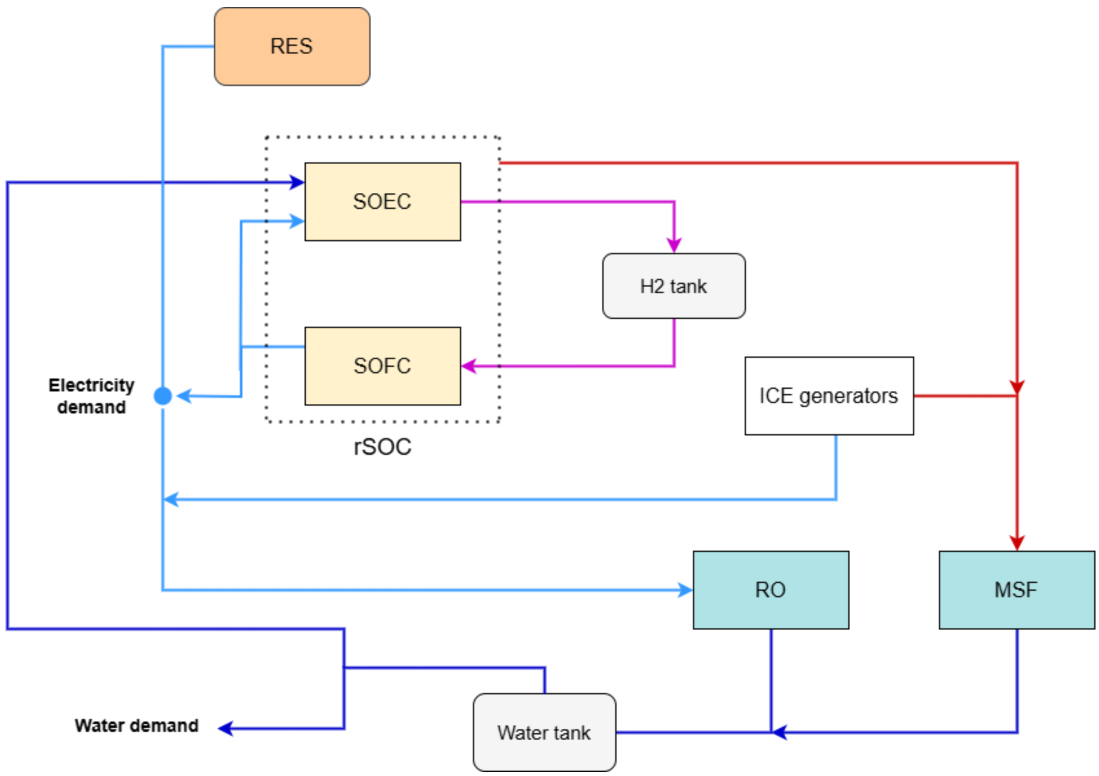

Figure 7.13: Overall layout of the integrated water/hydrogen production system.

Firstly, it helps meet the local electricity demand, and secondly, it provides the necessary electricity to operate desalination plants, which are responsible for producing potable water. The facilities in question utilise two well-established desalination techniques. The MSF distillation process requires a significant quantity of thermal energy. In order to enhance energy autonomy, the system integrates waste heat recovery from conventional ICE generators. These generators are an integral component of the island's power infrastructure, alongside the RES plant, with the purpose of enhancing grid stability.

The overall system layout is illustrated in Figure 7.13, in which the mass and energy fluxes are also delineated. The freshwater yielded by this process serves numerous critical functions. A considerable proportion of this water is allocated to meet the daily water consumption needs of the local and tourist population, thereby ensuring a consistent and sufficient supply. Moreover, the utilisation of purified water enables the functioning of a reversible solid oxide cell (rSOC). In electrolyser mode, the rSOC is contingent upon a reliable supply of water for the generation of green hydrogen. Each chemical is introduced into a tank, and subsequently distributed in accordance with demand. As demonstrated, the reversible SOC in FC mode has the capacity to supply heat energy for the MSF demand in the form of water vapour.

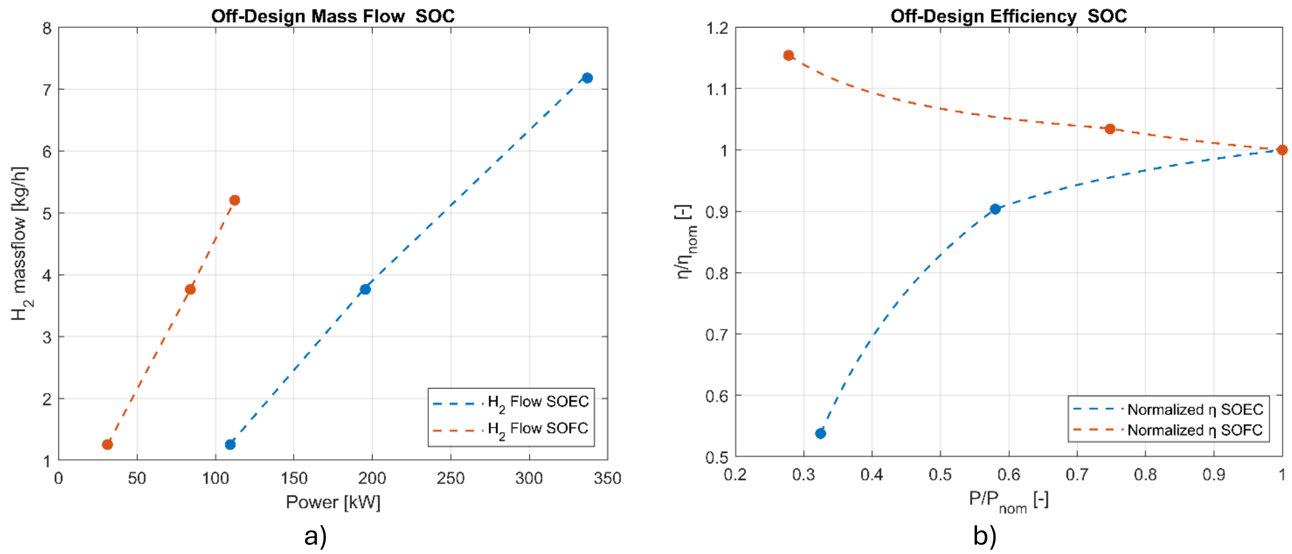

Figure 7.14: Overview of the reversible SOC fuel mass flow (a) and reversible SOC efficiency (b) as a result of piece-wise linearization of fuel mass flow.

The results of the linearisation process for the reversible rSOC in both SOEC and SOFC modes are presented in Figure 7.14, under the assumption that the mass and energy rates are always positive. It should be noted that the assumption of perfect linearity of the fuel flow curves Figure 7.14 (a). Conversely, the efficiencies shown in Figure 7.14 (b) are calculated a posteriori, using the linearized fuel mass flow and power. Furthermore, the marked decline in efficiency observed for SOEC mode can be explained by the fact that the system is particularly affected by the increased percentage of off-design losses due to balance of plant (BOP) components, such as the air compressor, heat exchangers and, in particular, the internal electric heater that has to sustain the overall thermal balance [144,145].

7.2.2 Inputs: electricity and feed water demands

In order to assess the potential of combined production of freshwater and hydrogen, the case study of a temperate Ikaria, Greek island, was chosen. The primary simulation parameters of the islands, along with pertinent demographic data [146] and freshwater demand per capita [147], are documented in Table 7.4.

Table 7.4: Main features of the chase study island (Greek Island).

Variable	**Value**	**Unite**
Resident population (2021)	8845	-
Climate type (Koppen zone)	Temperate (Csa)	-
Installed desalination capacity	500 (RO)	m^3/day
Winter Freshwater consumption	150	litres/day pc
Summer Freshwater consumption	250	litres/day pc

The freshwater consumption data of the Greek island refer exclusively to domestic use and do not include agricultural, industrial or recreational uses. In order to simplify the analysis, and in particular due to the absence of data in the existing literature on hourly water consumption over the course of a year, the optimisation process was simplified to cover only 12 representative days, one day from each month.

Furthermore, Figure 7.15a and Figure 7.15b illustrate the seasonal population variation and the hourly freshwater demand for a typical winter and a typical summer day, respectively. The selection of typical months for the representation was made with consideration for the months exhibiting the most significant disparities in population; consequently, January and August were identified as the extreme month, as illustrated in Figure 7.15. There is a pronounced increase in the number of inhabitants during the summer months, with a more than twofold rise in population as shown in Figure 7.15. Furthermore, the resident population was hypothesised to remain constant over the course of the year [147].

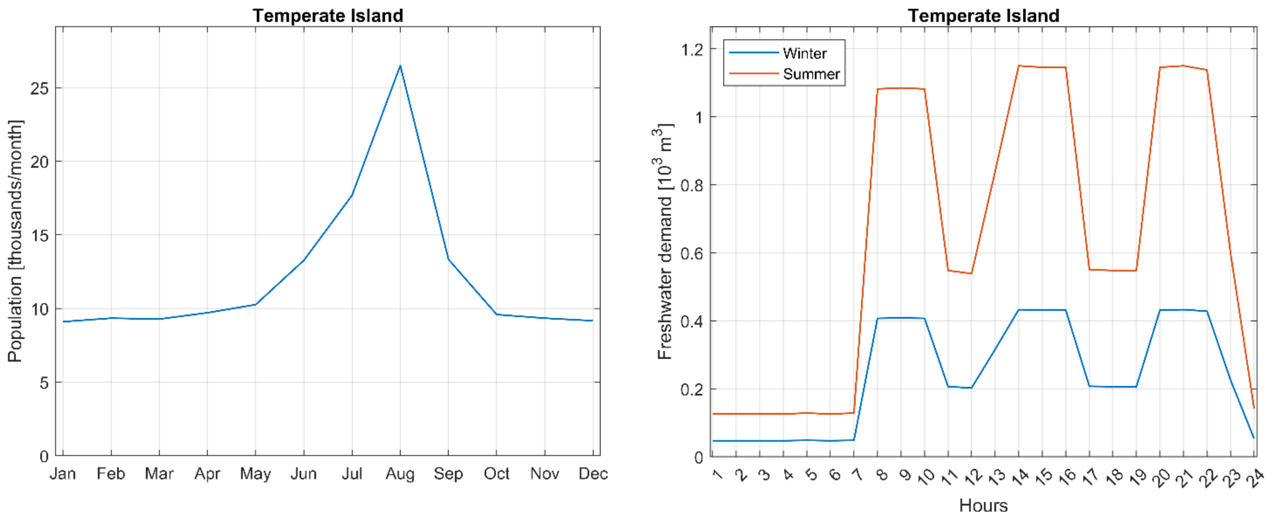

a) b)

Figure 7.15: Monthly variation of population (a) and hourly freshwater consumption (b) on the case study island

7.2.3 Scenario and KPI definition

In order to explore the advantages of coupling an integrated RO/rSOC system to a photovoltaic panel renewable power system, two cases were considered. In the baseline the presence of ICE is necessary for the production of electricity. Consequently, the capital expenditures of these components are not accounted for the LCOW, and the desalinated water is obtained via thermal MSF, thereby utilising ICE waste heat recovery. The Scenario 1 includes the addition of membrane-based reverse osmosis desalination and PV for power production (PV/RO), while Scenario 2 is expanded with the inclusion of the reversible SOC or RC as adopted in the future equations (PV/RO/RC).

A sensitivity analysis has been performed, depending on the relevant parameters, such as installed PV power, RO installed capacity, and rSOC installed power in electrolyser mode. The results are then compared in terms of techno-economic metrics, including LCOE, Levelised Cost of Water (LCOW), renewable energy share, and SCI. As defined in Eq. 6-9, the levelised costs are defined in the context of the presence or absence of the Reversible Cell system (RC). The specific CAPEX values employed in the computation of economic figures are documented in Table 7.5.

Table 7.5: Overview of simulation cases and economic parameters for each technology.

Technology	Scenario	Specific CAPEX	Unite
ICE	1,2	350	€/kW
Thermal Process (MSF) [148]	1,2	$2567 \cdot \dot{V}^{0.9878}$	€/ (m³/day)
RES (PV) [149]	1,2	530	€/kW
Membrane Process (RO) [78]	1,2	1910	€/(m³/day)
rSOC [77]	2	1000	€/kW_{EC}

The CAPEX values are computed by multiplying the specific CAPEX from Table 7.5 by the CRF, defined through Eq. 7.12. This enables the consistent assessment of OPEX and CAPEX on the same time horizon. The interest rate *i* is set equal to 5% and the useful life *n* is assumed as 25 years for each technology. On the other hand, $P_{RO,PAY}$ is the fraction of power supplied by the RO which does not derive from curtailed PV power and thus represents an active cost contribute in the LCOW definition.

$$LCOE_{w/o\ RC}\ \left[\frac{€}{MWh}\right] = \frac{CAPEX_{PV} + OPEX_{ICE} + CO_{2,ICE}}{Demand_{el} + P_{RO}} \quad 7.8$$

$$LCOW_{w/o\ RC}\ \left[\frac{€}{MWh}\right] = \frac{CAPEX_{RO}\ +\ CAPEX_{MSF} + LCOE \cdot P_{RO,PAY}}{Prod_{RO} + Prod_{MSF}} \quad 7.9$$

$$LCOE_{RC}\ \left[\frac{€}{MWh}\right] = \frac{CAPEX_{PV} + CAPEX_{RC} + OPEX_{ICE} + CO_{2,ICE}}{Demand_{el} + P_{RO}} \quad 7.10$$

$$LCOW_{RC}\ \left[\frac{€}{MWh}\right] = \frac{CAPEX_{RO} +\ CAPEX_{MSF} + LCOE \cdot P_{RO,PAY}}{Prod_{RO} + Prod_{MSF} + Prod_{RC}} \quad 7.11$$

$$CRF_k = \frac{i \cdot (1+i)^n}{(1+i)^n - 1} \quad 7.12$$

7.2.4 Results and discussion, Scenario 1 (PV+RO)

In this initial section, the scenario of baseline water production via MSF combined with PV and RO integration was analysed in terms of the KPIs presented in the preceding section.

Initially, the levelised costs of the primary products of the combined generation system are evaluated for varying installed capacities of reverse osmosis plants and differing levels of installed photovoltaic power. In the subsequent stage of the analysis, the RES share, Specific Carbon Intensity (SCI), and water production via MSF and RO are also evaluated as a function of the same parameters size parameters.

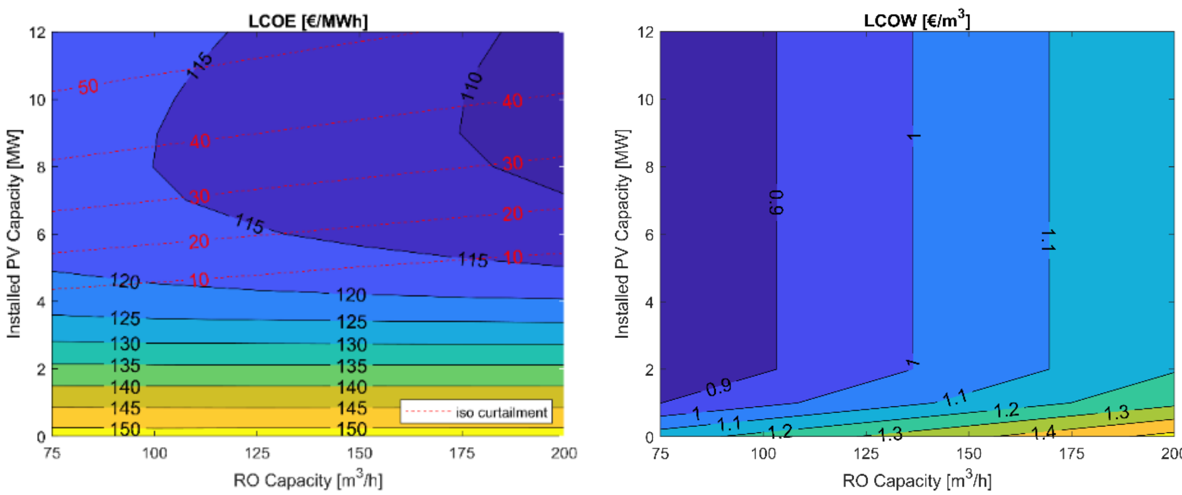

a) b)

Figure 7.16: LCOE (a) and LCOW (b) for different installed RO and PV capacities under Scenario 1

As illustrated in Figure 7.16, the LCOE (a) and LCOW (b) for Scenario 1 are presented, with the RES curtailment levels indicated as red contour lines as a percentage of RES potential. As illustrated in Figure 7.16a, the implementation of PV installations has been shown to contribute to a reduction in the Levelized Cost of Energy (LCOE). This is primarily achieved through the substitution of conventional internal combustion engine (ICE) production with RES, keeping the values of RES curtailment value below 10%. This optimal value is reported to be approximately 4 MW, where a LCOE ranging from 120 to 125 €/MWh. In this zero curtailment zone, the level of dependence of LCOE on RO capacity is minimal, suggesting that a significant proportion of electricity is still produced by ICE generators at a higher cost. For higher values of PV capacity, an optimum trend is registered, and RES curtailment is influenced by RO capacity in terms of its ability to absorb excess generation, thereby producing water at zero cost and acting as an effective solution to mitigate the curtailment. This results in the lowest electricity cost with large RO and photovoltaic capacity. As illustrated in Figure 7.16b, the boundary of LCOW dependence on photovoltaic capacity is demonstrated to be approximately 2 MW. In scenarios where the value is lower than the specified benchmark, the cost of freshwater is predominantly influenced by the expenses associated with the energy consumption of the RO plant. This energy expenditure is compensated through the remuneration of the plant's LCOE. For larger values, the energy absorbed by RO is equivalent to the PV overgeneration with respect to the Electrical Demand, rendering the quantity of installed RES potential irrelevant. It has been demonstrated that the impact of RO adoption on LCOE and LCOW is contrary: transitioning from MSF to RO production results in a reduction of the LCOE from 115 to 110 €/MWh (- 4.5%), due to a decrease in electricity production by ICE. Conversely, there is an augmentation in water production costs from 0.9 to 1.1 €/m^3 (+22%), due to the increase capital cost for the RO system.

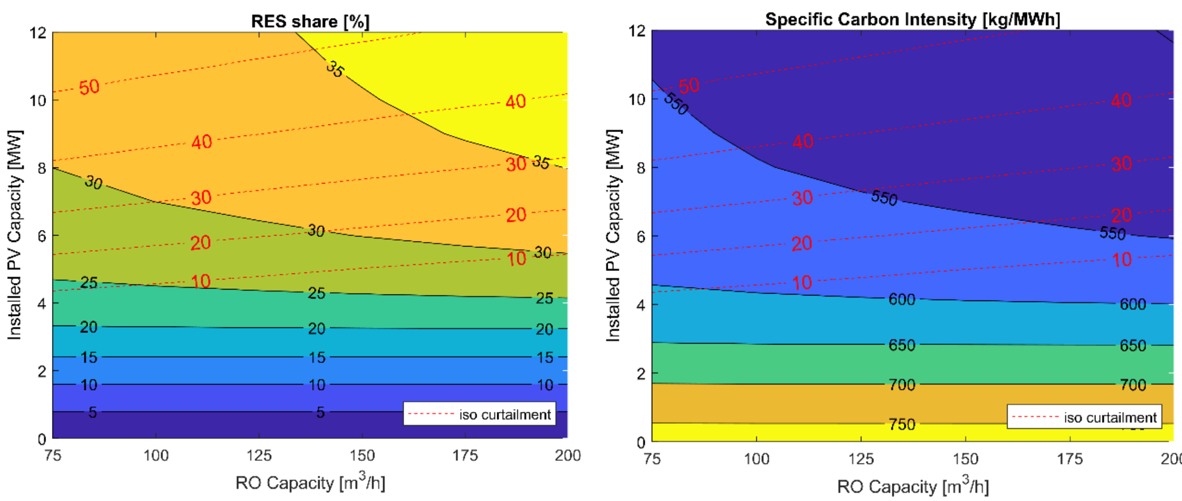

Figure 7.17: RES share (a) and Specific Carbon Intensity (b) for different installed RO and PV capacities under Scenario 1

As illustrated in Figure 7.17a, it appears to be confirmed that the 4 MW threshold is indicative of the optimal RES share and RES curtailment. In this condition the RES share is quite independent of installed RO. However, it is noteworthy that the proportion of electricity generated by photovoltaic (PV) systems remains below 35%, even for large installed capacity of PV. This phenomenon can be elucidated by considering the concurrent freshwater production activities undertaken by MSF. Consequently, the incorporation of thermal energy from ICEs does not contribute to the overall cost of electricity production. Consequently, the optimiser maximises the cheaper water produced by MSF under all circumstances, even when the potential to produce it from renewable sources is high. As demonstrated in Figure 7.17b, the SCI (total specific carbon emission of the system) displays a trend that is analogous to the RES share.

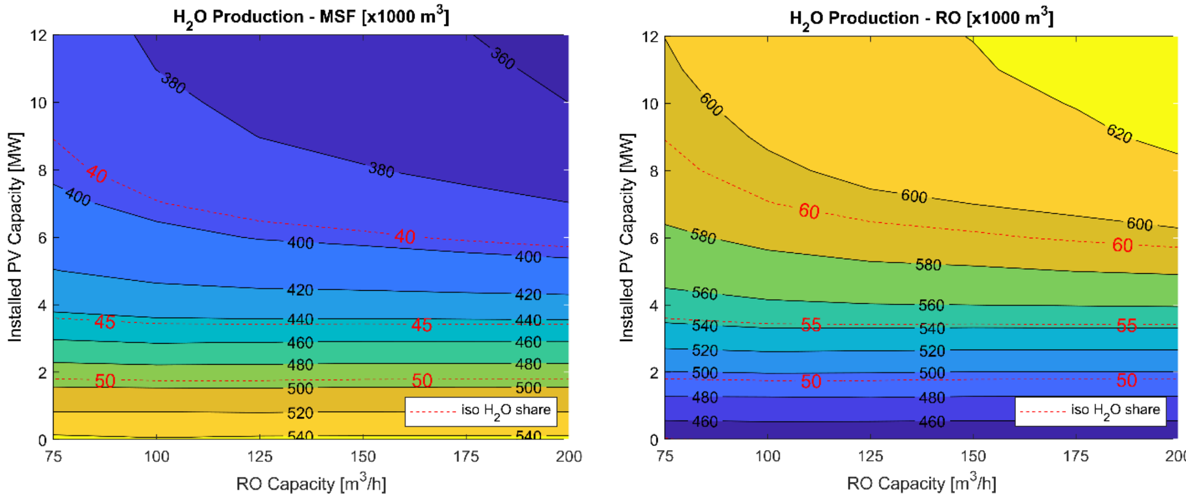

a) b)

Figure 7.18: Water production via MSF (a) and RO (b) for different installed RO and PV capacities under Scenario 1

Figure 7.18a and Figure 7.18b illustrate the freshwater production of Multi-Stage Flash and Reverse Osmosis, respectively. It has been observed that the behaviour exhibited by systems with PV capacities below 2 MW is predominantly influenced by the amount of RO input electricity that is not associated with overgeneration. In addition, it appears evident that, despite exhibiting a consistent potential, the proportion of water production via RO/RES is constrained to a value slightly exceeding 60%. This phenomenon can be attributed to the fact that MSF exploitation remains more expedient, even when ICE operates at reduced loads.

7.2.5 Results and discussion, Scenario 2 (PV+RO+rSOC)

In the second scenario, the sensitivity analysis is conducted by considering the variation of the installed capacity of the rSOC in electrolytic cell (EC) mode. The RO capacity was set at 100 m^3/h, under which conditions a minimum LCOE of 115 €/MWh is achieved for 8 MW of installed photovoltaic capacity and 0.9 €/m^3 for the LCOW, regardless of installed PV capacity, as shown in Figure 7.16b. The installed SOEC capacity on the x-axis was considered as the aggregate of multiple units of the same type. In this analysis, hydrogen demand was not considered, and the only use of the produced hydrogen is as fuel when the rSOC operates in FC mode as a storage medium.

As illustrated in Figure 7.19, the results are presented in terms of levelised costs. As demonstrated in Figure 7.19, in instances where rSOC is not utilised as storage, the installed capacity of the SOEC has a negative effect on the LCOE. This is attributable to the increase in capital expenditure (CAPEX) with size, as expressed in Eq. 7.8. For PV capacities exceeding 4 MW, the rSOC exhibits an increase in operability, resulting in a reduction of curtailed RES production for an equivalent PV capacity as observed in Scenario 1. The phenomenon can be explained by the increased capacity of the rSOC/RO assembly, which has a greater probability of functioning as a storage system that generates water and hydrogen. When the PV capacity reaches 6 MW, the minimum LCOE of Scenario 1 is attained, at 115 €/MWh, for 1.3 MW of SOEC capacity, resulting in 5% curtailment, where analogous economic conditions are achieved in Scenario 1 with approximately 38% of discarded RES production. Furthermore, at 8 MW of PV, a lower LCOE can be attained, nominally 110 €/MWh, with 2.5 MW of SOEC without exceeding 10% curtailment.

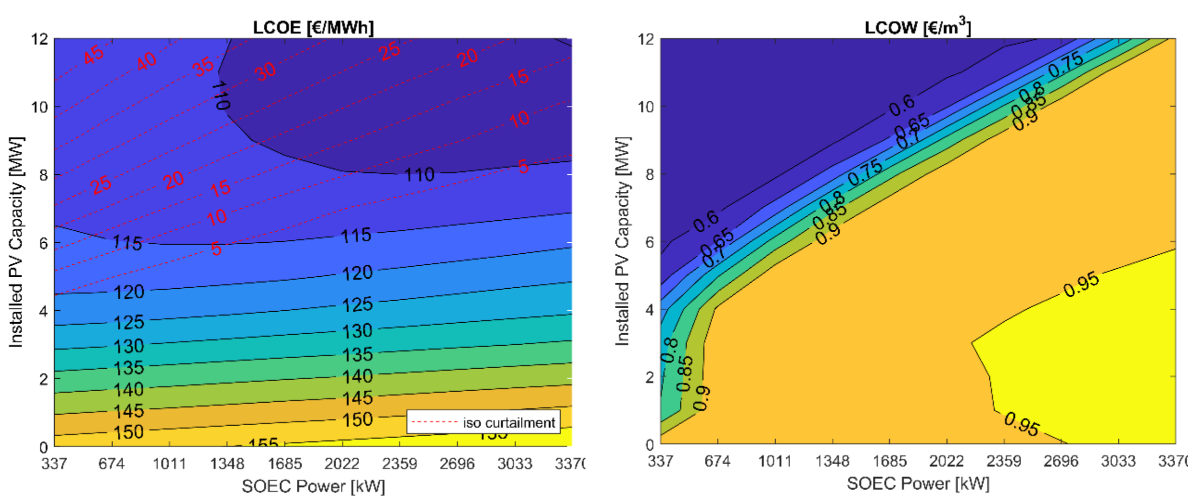

a) b)

Figure 7.19: LCOE (a) and LCOW (b) for different installed rSOC and PV capacities under Scenario 2

Conversely, Figure 7.19b demonstrates that the LCOW remains contingent on both rSOC capital cost and correlated LCOE variation. In contradistinction to Scenario 1, a substantial area characterised by minimal water costs is identified for high PV capacity and reduced SOEC size. Moreover, the LCOW trend differs considerably from that of Scenario 1, suggesting that the quantity of installed PV has a considerable effect on the cost of water, which remains consistently lower than in Scenario 1. The cost exceeds the base cost of 0.9 €/m^3 only in the absence of curtailment, remaining below 1 €/m^3 even for minimal PV capacity.

As previously highlighted, the results of Scenario 1 are consistent with the findings of the study. For instance, the combination of 6 MW PV and 1.3 MW rSOC results in a cost of 0.9 €/m3 of fresh water, while an increase in the rSOC size leads to a general rise in water costs. Increases in photovoltaic (PV) production in the presence of storage have been shown to result in a decrease in water costs, reaching a plateau of 0.6 €/m3 when all the RO input energy is provided by excess renewable energy production.

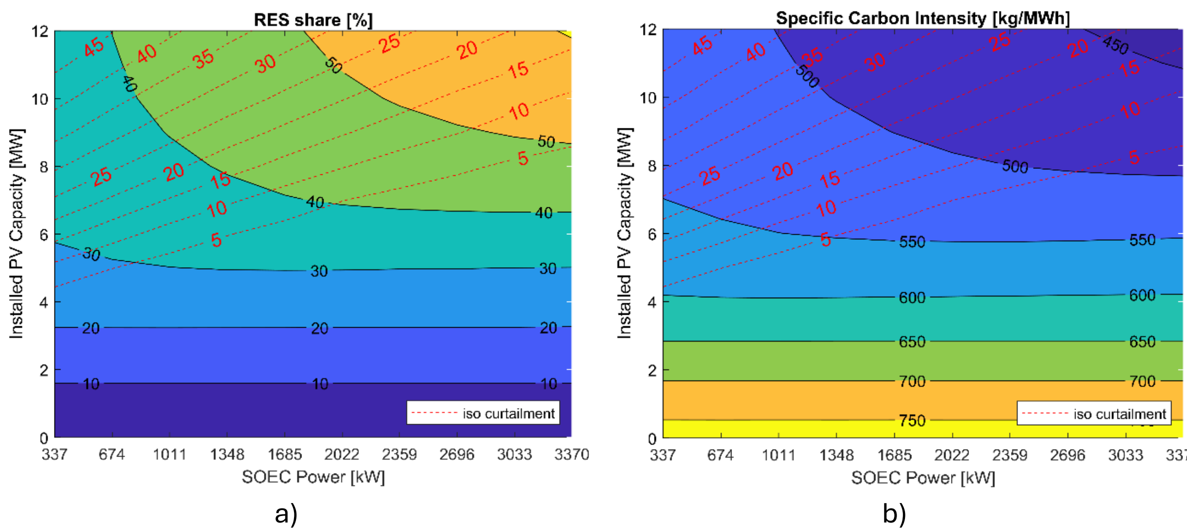

Figure 7.20: RES share (a) and Specific Carbon Intensity (b) for different installed rSOC and PV capacities under Scenario 2

Concerning the RES share in Scenario 2 Figure 7.20 (a), the overall trend is consistent with that observed in Scenario 1Figure 7.17 (a), although the absolute values are systematically higher. This enhancement can be attributed primarily to the augmented capacity of the system to absorb surplus renewable energy, facilitated by the integration of both RO and the reversible Solid Oxide Cell (rSOC). The contour plots of curtailed RES energy further corroborate this behaviour, demonstrating a general reduction in renewable curtailment as system flexibility increases.

A similar pattern is observed for the Specific Carbon Intensity presented in Figure 7.20 (b). Although the trend closely mirrors that of Scenario 1, the absolute reduction in emissions per unit of electricity generated remains relatively limited. This outcome can be attributed to the sustained substantial contribution of ICE generators, which continue to be utilised not only for electricity generation but also for the provision of thermal energy for the MSF desalination process.

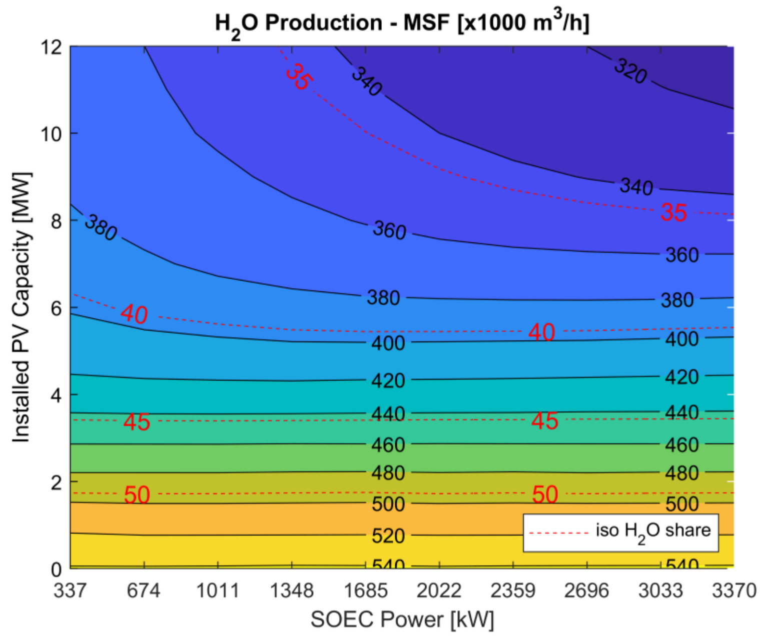

Figure 7.21: Water production via MSF for different installed rSOC and PV capacities under Scenario 2

This interpretation is further substantiated by Figure 7.21, Figure 7.22 and Figure 7.23, which indicate that freshwater production is almost equally shared between RO and MSF technologies, even under scenarios with high installed PV capacity and large rSOC systems. The contribution of the rSOC to freshwater production, whether operating in electrolysis (EC) or fuel cell (FC) mode, remains negligible, accounting for no more than approximately 3.5% of the total freshwater supply. This is only the case, however, in conditions of high renewable availability coupled with large system sizing. The findings indicate that, while the rSOC enhances the system's flexibility and its capacity to utilise surplus renewable energy, its direct impact on freshwater production is constrained. However, it is imperative to interpret this finding in conjunction with hydrogen production dynamics, which have the capacity to alter the overall system behaviour and engender divergent operational outcomes when the full multi-energy interaction is given full consideration.

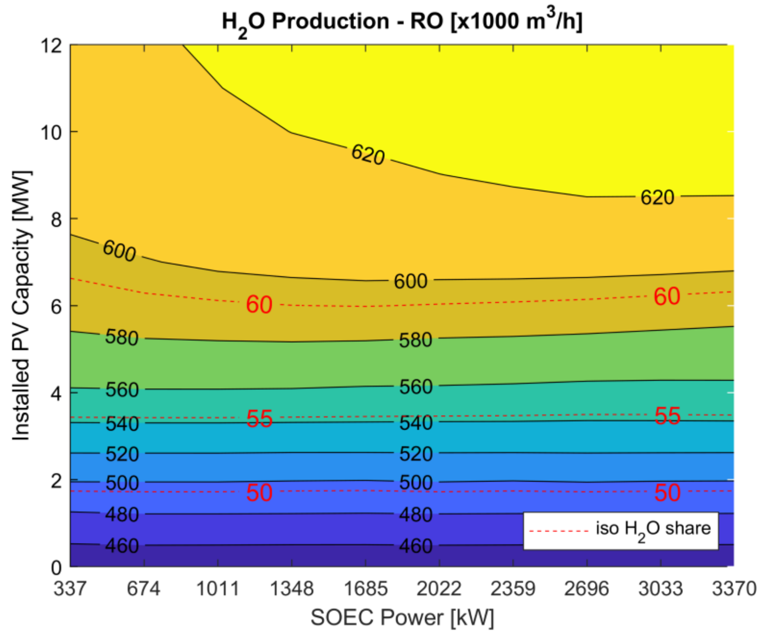

Figure 7.22: Water production via RO for different installed rSOC and PV capacities under Scenario 2

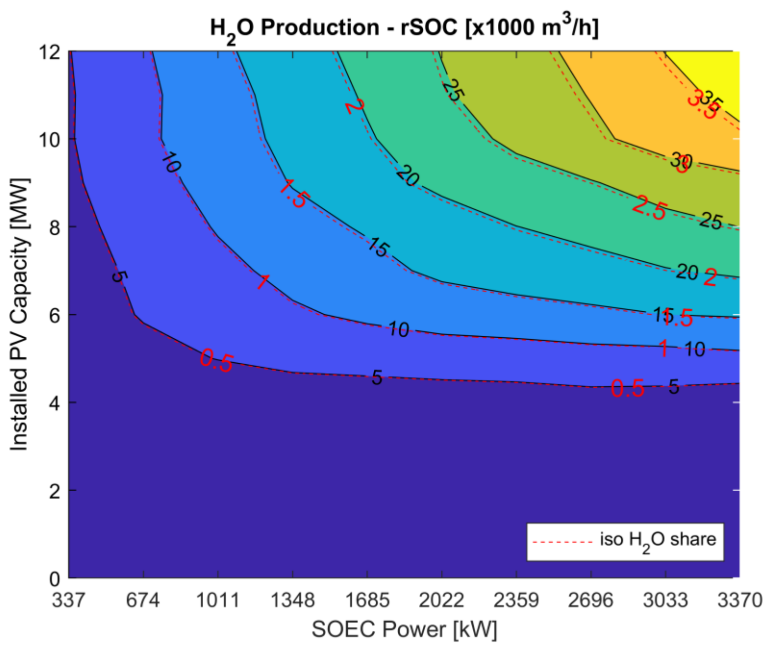

Figure 7.23: Water production via rSOC for different installed rSOC and PV capacities under Scenario 2

Chapter 8

Conclusion and remarks

This thesis presents the development and application of the Multi-Energy Dispatch Optimiser (MEDO), a MILP-based framework for the optimal management of complex energy systems in the maritime sector and in isolated energy environments. The work has addressed both methodological and application-oriented challenges associated with modern energy management systems.

A comparative analysis of optimisation frameworks was conducted at the outset of this work. MILP, which operates on discretised or linearised objective functions, was compared with algorithms based on continuous optimisation of a nonlinear objective function. While non-linear algorithms can fully evaluate the complexity of the objective function, the results show that MILP outperforms these methods for dispatch optimisation. Specifically:

- MILP demonstrated better convergence with increasing problem size (number of optimised variables), while other algorithms suffered performance degradation due to the complexity of the problem.
- MILP consistently demonstrated higher optimality and was generally the fastest algorithm, outperforming Active Set, Interior Point, and SQP algorithms. It has been determined that the slowest algorithms are those of a genetic and surrogate nature.
- Algorithms requiring an initial solution were highly sensitive to the choice of this solution. This problem limited the robustness and reproducibility of the optimal solution; MILP, on the other hand, has consistently found the same optimal solution.

These findings emphasise the robustness and scalability of MILP, making it a particularly suitable solution for real-world energy dispatch problems where reliability and global optimality are essential. The design of complex systems requires a robust framework that supports the definition of complex constraints, both those specific to each module and those governing their interconnections.

The MEDO framework was applied to onboard energy management for a cruise ship, aiming to optimise the combined electrical and thermal power generation. The electrical demand was primarily met by the engines, with up to 3.8% supplied by BES. The recovery of heat from engine exhaust was optimised to meet demand, thereby improving the overall system efficiency. During the 120-hour mission, CO_2 emissions were reduced by 5%, equivalent to approximately 1,450 tons per year. MEDO provided rapid and reliable convergence, with residuals below 0.3% after 140 seconds, while piecewise linearization of system characteristics ensured accurate representation of off-design behaviour.

The MEDO framework was also applied to isolated island energy systems to evaluate the optimal integration of renewable energy sources, storage, and hybrid technologies under different operational scenarios. The studies demonstrated that, in the absence of energy storage, the maximum share of renewables was constrained by system flexibility, often resulting in curtailment rates of up to 55%. An optimal wind-to-PV ratio of approximately 2 was identified to balance generation between sources. The introduction of energy storage, either through pumped hydro storage (PHS) or reversible solid oxide cells (rSOC), has led to a significant reduction in curtailment to below 1–25%, while enabling higher renewable shares of up to 50%. Economically, the levelized cost of electricity (LCOE) decreased with increased renewable capacity, reaching a minimum of 70–77.5 €/MWh when storage was included, compared to 100–117.5 €/MWh without storage. From an environmental perspective, the incorporation of renewables and storage solutions has led to a significant reduction in the specific carbon intensity (SCI). In scenarios with high reliance on fossil fuels, the SCI has been reduced from 500 kg/MWh to 250–350 kg/MWh, depending on the specific scenario analysed. The studies also demonstrated that energy storage and hybrid technologies, such as reverse osmosis for water production and rSOC for hydrogen generation, effectively absorbed surplus renewable energy, enhancing system flexibility and maximising renewable utilisation. The results demonstrate that system flexibility and storage integration are pivotal in achieving high renewable energy penetration, minimising curtailment, enhancing economic performance, and reducing carbon emissions in isolated energy systems.

The developed framework has proven highly flexible and adaptable to a wide range of optimisation problems. In fact, in addition to the scenarios examined in this thesis, it has been used in sectors such as industry and hydrogen production. Several future developments and improvements can be anticipated, such as adding a module that optimises the size of plant components directly into the objective function rather than through sensitivity analysis. This avoids overfitting to a specific operating profile, but requires significantly longer optimisation periods.

In the context of remote islands and, more generally, where renewable generators are present, it is important to conduct a sensitivity analysis of production uncertainty to provide a more robust solution and generalise the optimisation output.

Bibliography

[1] Internetional Maritime Organization, (IOM), 2018, “IMO, Initial IMO GHG Strategy.” [Online]. Available: https://www.imo.org/en/MediaCentre/HotTopics/Pages/Reducing-greenhouse-gas-emissions-from-ships.aspx. [Accessed: 07-Mar-2024].

[2] International Maritime Organization, 2023, “IMO and the UNFCCC Policy Framework.” [Online]. Available: https://www.imo.org/en/ourwork/environment/pages/2023-imo-strategy-on-reduction-of-ghg-emissions-from-ships.aspx. [Accessed: 19-Mar-2026].

[3] Ritchie, H., Rosado, P., and Roser, M., 2023, “CO_2 and Greenhouse Gas Emissions,” Our World in Data.

[4] Martin, R., “GHG EMISSIONS OF ALL WORLD COUNTRIES JRC SCIENCE FOR POLICY REPORT.” https://doi.org/10.2760/5917997.

[5] L. Cozzi, and T. Gould, 2025, *World Energy Outlook*. [Online]. Available: https://www.iea.org/reports/world-energy-outlook-2025. [Accessed: 23-Mar-2026].

[6] Maamoun, N., 2019, “The Kyoto Protocol: Empirical Evidence of a Hidden Success,” J. Environ. Econ. Manage., pp. 227–256.

[7] United Nations Climate Change, 2015, “The Paris Agreement.” [Online]. Available: https://unfccc.int/process-and-meetings/the-paris-agreement. [Accessed: 23-Mar-2026].

[8] IMO, “IMO Emissions Control Areas.” [Online]. Available: https://www.imo.org/en/ourwork/environment/pages/emission-control-areas-(ecas)-designated-under-regulation-13-of-marpol-annex-vi-(nox-emission-control).aspx. [Accessed: 23-Mar-2025].

[9] IMO, “Short-Term GHG Reduction Measure,” 2022. [Online]. Available: https://www.imo.org/en/ourwork/environment/pages/short-term-ghg-reduction-measure.aspx. [Accessed: 23-Mar-2025].

[10] Mathworks, “Matlab Fmincon Algorithms.” [Online]. Available: https://it.mathworks.com/help/optim/ug/constrained-nonlinear-optimisation-algorithms.html. [Accessed: 13-Oct-2022].

[11] MatLab, “MILP.” [Online]. Available: https://it.mathworks.com/help/optim/ug/mixed-integer-linear-programming-algorithms.html. [Accessed: 06-Oct-2022].

[12] MatLab, “Global Optimisation Toolbox.” [Online]. Available: https://it.mathworks.com/help/gads/. [Accessed: 06-Oct-2022].

[13] MatLab, “ Fmincon Choosing the Algorithm.” [Online]. Available: https://it.mathworks.com/help/optim/ug/choosing-the-algorithm.html#brppuoz. [Accessed: 10-Oct-2022].

[14] Mehrotra, S., 1992, "On the Implementation of a Primal-Dual Interior Point Method," SIAM Journal on Optimisation, **2**(4). https://doi.org/10.1137/0802028.

[15] Zhang, Y., 1998, "Solving Large-Scale Linear Programs by Interior-Point Methods under the MATLAB Environment," Optim. Methods Softw., **10**(1). https://doi.org/10.1080/10556789808805699.

[16] Dantzig, G. B., Orden, A., and Wolfe, P., 1955, "The Generalized Simplex Method for Minimizing a Linear Form under Linear Inequality Restraints," Pac. J. Math., **5**(2). https://doi.org/10.2140/pjm.1955.5.183.

[17] Mészáros, C., and Suhl, U. H., 2003, "Advanced Preprocessing Techniques for Linear and Quadratic Programming," OR Spectrum, **25**(4). https://doi.org/10.1007/s00291-003-0130-x.

[18] Cornuéjols, G., 2008, "Valid Inequalities for Mixed Integer Linear Programs," *Mathematical Programming*. https://doi.org/10.1007/s10107-006-0086-0.

[19] Achterberg, T., Bixby, R. E., Gu, Z., Rothberg, E., and Weninger, D., 2020, "Presolve Reductions in Mixed Integer Programming," INFORMS J. Comput., **32**(2). https://doi.org/10.1287/ijoc.2018.0857.

[20] Waltz, R. A., Morales, J. L., Nocedal, J., and Orban, D., 2006, "An Interior Algorithm for Nonlinear Optimisation That Combines Line Search and Trust Region Steps," Math. Program., **107**(3). https://doi.org/10.1007/s10107-004-0560-5.

[21] Byrd, R. H., Hribar, M. E., and Nocedal, J., 1999, "An Interior Point Algorithm for Large-Scale Nonlinear Programming," SIAM Journal on Optimisation, **9**(4). https://doi.org/10.1137/S1052623497325107.

[22] Byrd, R. H., Gilbert, J. C., and Nocedal, J., 2000, "A Trust Region Method Based on Interior Point Techniques for Nonlinear Programming," Mathematical Programming, Series B, **89**(1). https://doi.org/10.1007/PL00011391.

[23] Moré, J. J., and Sorensen, D. C., 1983, "Computing a Trust Region Step," SIAM Journal on Scientific and Statistical Computing, **4**(3). https://doi.org/10.1137/0904038.

[24] Schittkowski, K., 1986, "NLPQL: A Fortran Subroutine Solving Constrained Nonlinear Programming Problems," Ann. Oper. Res., **5**(1–4). https://doi.org/10.1007/BF02739235.

[25] Chambers, LL. G., 2001, "Practical Methods of Optimisation (2nd Edn)," The Mathematical Gazette, **85**(504). https://doi.org/10.2307/3621816.

[26] Dennis, J. E., Gay, D. M., and Walsh, R. E., 1981, "An Adaptive Nonlinear Least-Squares Algorithm," ACM Transactions on Mathematical Software (TOMS), **7**(3). https://doi.org/10.1145/355958.355965.

[27] Dantzig, G. B., 2021, "Linear Programming and Extensions," *A Century in Books: Princeton University Press 1905–2005*. https://doi.org/10.2307/2344013.

[28] Goldberg, D. E., 1989, "Genetic Algorithms in Search," Optimisation, and MachineLearning, **27**(02).

[29] Conn, A. R., Gould, N. I. M., and Toint, P. L., 1991, "Globally Convergent Augmented Lagrangian Algorithm for Optimisation with General Constraints and Simple Bounds," SIAM J. Numer. Anal., **28**(2). https://doi.org/10.1137/0728030.

[30] Conn, A. R., Gould, N., and Toint, Ph. L., 1997, "A Globally Convergent Lagrangian Barrier Algorithm for Optimisation with General Inequality Constraints and Simple Bounds," Math. Comput., **66**(217). https://doi.org/10.1090/s0025-5718-97-00777-1.

[31] Regis, R. G., and Shoemaker, C. A., 2007, "A Stochastic Radial Basis Function Method for the Global Optimisation of Expensive Functions," INFORMS J. Comput., **19**(4). https://doi.org/10.1287/ijoc.1060.0182.

[32] Gutmann, H.-M., 2001, *A Radial Basis Function Method for Global Optimisation*.

[33] Kolda, T. G., Lewis, R. M., and Torczon, V., 2003, "Optimisation by Direct Search: New Perspectives on Some Classical and Modern Methods," SIAM Review, **45**(3). https://doi.org/10.1137/S003614450242889.

[34] Fleischer, M., 2003, "The Measure of Pareto Optima Applications to Multi-Objective Metaheuristics," Lecture Notes in Computer Science (including subseries Lecture Notes in Artificial Intelligence and Lecture Notes in Bioinformatics), **2632**. https://doi.org/10.1007/3-540-36970-8_37.

[35] Bratley, P., and Fox, B. L., 1988, "Algorithm 659: Implementing Sobol's Quasirandom Sequence Generator," ACM Transactions on Mathematical Software (TOMS), **14**(1). https://doi.org/10.1145/42288.214372.

[36] Sorce, A., Giugno, A., Marino, D., Piola, S., and Guedez, R., 2019, "Analysis of a Combined Cycle Exploiting Inlet Conditioning Technologies for Power Modulation," *Proceedings of the ASME Turbo Expo*. https://doi.org/10.1115/GT2019-91541.

[37] Ricerca sul Sistema Energetico – RSE SpA, 2014, *Energia Elettrica, Anatomia Dei Costi*.

[38] Rodilla, P., Cerisola, S., and Batlle, C., 2014, "Modeling the Major Overhaul Cost of Gas-Fired Plants in the Unit Commitment Problem," IEEE Transactions on Power Systems, **29**(3), pp. 1001–1011. https://doi.org/10.1109/TPWRS.2013.2293604.

[39] TSO, T. S. O., 2008, "Transparency Platform (ENTSOe)." [Online]. Available: https://transparency.entsoe.eu/?appState=%7B%22sa%22%3A%5B%5D%2C%22st%22%3A%22BZN%22%2C%22mm%22%3Atrue%2C%22ma%22%3Afalse%2C%22sp%22%3A%22CLOSED%22%2C%22dt%22%3Anull%2C%22df%22%3Anull%2C%22tz%22%3A%22CET%22%7D. [Accessed: 19-Nov-2025].

[40] Investing, "Dutch TTF Natural Gas Futures Historical Data." [Online]. Available: https://www.investing.com/commodities/dutch-ttf-gas-c1-futures-historical-data. [Accessed: 20-Nov-2025].

[41] Intergovernmental panel on climate change (IPCC)., Masson-Delmotte, V., Zhai, P., and Pirani, A., 2021, *Climate Change 2021 : The Physical Science Basis : Summary for Policymakers : Working Group I Contribution to the Sixth Assessment Report of the Inter-Governmental Panel on Climate Change*.

[42] EMBER, 2021, "Average CO2 Cost." [Online]. Available: https://ember-climate.org/data/data-tools/carbon-price-viewer/. [Accessed: 06-Oct-2022].

[43] Climate Copernicus, "Temperature." [Online]. Available: https://cds.climate.copernicus.eu/cdsapp#!/dataset/reanalysis-era5-land?tab=form. [Accessed: 12-Oct-2022].

[44] Lee, J. O., and Kim, Y. S., 2022, “Novel Battery Degradation Cost Formulation for Optimal Scheduling of Battery Energy Storage Systems,” International Journal of Electrical Power and Energy Systems, **137**. https://doi.org/10.1016/j.ijepes.2021.107795.

[45] Mauler, L., Duffner, F., Zeier, W. G., and Leker, J., 2021, “Battery Cost Forecasting: A Review of Methods and Results with an Outlook to 2050,” Energy Environ. Sci., **14**(9), pp. 4712–4739. https://doi.org/10.1039/d1ee01530c.

[46] Cole, W., Frazier, A. W., and Augistine, C., 2021, *Cost Projections for Utility-Scale Battery Storage: 2021 Update.*

[47] MathWorks, 2022, *Optimisation Toolbox™ User’s Guide R2022b*. [Online]. Available: www.mathworks.com.

[48] Mathworks, “Fmincon Function.” [Online]. Available: https://it.mathworks.com/help/optim/ug/fmincon.html. [Accessed: 27-Jun-2024].

[49] Vasylyev, A., Vannoni, A., and Sorce, A., 2024, “Best Practices for Electricity Generators and Energy Storage Optimal Dispatch Problems,” J. Eng. Gas Turbine. Power, **146**(3). https://doi.org/10.1115/1.4063529.

[50] Mancarella, P., 2014, “MES (Multi-Energy Systems): An Overview of Concepts and Evaluation Models,” Energy, **65**. https://doi.org/10.1016/j.energy.2013.10.041.

[51] Papavasiliou, A., and Oren, S. S., 2014, “Large-Scale Integration of Deferrable Demand and Renewable Energy Sources,” IEEE Transactions on Power Systems, **29**(1). https://doi.org/10.1109/TPWRS.2013.2238644.

[52] Meng, Y., Wang, Y., Sun, S., Wang, S., and Zhang, H., 2023, “Multi-Objective Optimal Dispatching of Demand Response-Enabled Microgrid Considering Uncertainty of Renewable Energy Generations Based on Two-Level Iterative Strategy,” Energy Reports, **9**. https://doi.org/10.1016/j.egyr.2022.12.149.

[53] Parvania, M., and Fotuhi-Firuzabad, M., 2010, “Demand Response Scheduling by Stochastic SCUC,” IEEE Trans. Smart Grid, **1**(1). https://doi.org/10.1109/TSG.2010.2046430.

[54] Niknam, P. H., Fisher, R., Ciappi, L., and Sciacovelli, A., 2024, “Optimally Integrated Waste Heat Recovery through Combined Emerging Thermal Technologies: Modelling, Optimisation and Assessment for Onboard Multi-Energy Systems,” Appl. Energy, **366**. https://doi.org/10.1016/j.apenergy.2024.123298.

[55] Sioshansi, R., Denholm, P., Jenkin, T., and Weiss, J., 2009, “Estimating the Value of Electricity Storage in PJM: Arbitrage and Some Welfare Effects,” Energy Econ., **31**(2). https://doi.org/10.1016/j.eneco.2008.10.005.

[56] Vasylyev, A., Dubey, A., and Sorce, A., 2026, “Economic Potential of Combined Cycle Flexibility: Bottoming Cycle Hot Standby Mode and Gas Turbine Peak Firing in the European and u.s. Markets,” *ASME 2026 Turbomachinery Technical Conference & Exposition (GT2026)*, Milan.

[57] Kim, H., Vasylyev, A., and Sorce, A., 2026, “Comparative Performance and Operating Strategies of Electric-Heating-Assisted Compressed Air Energy Storage,” *ASME 2026 Turbomachinery Technical Conference & Exposition (GT2026)*, Milan.

[58] Natali, J. M., and Pinto, J. M., 2009, “Piecewise Polynomial Interpolations and Approximations of One-Dimensional Functions through Mixed Integer Linear Programming,” Optim. Methods Softw., **24**(4–5). https://doi.org/10.1080/10556780802614507.

[59] D’Ambrosio, C., Lodi, A., and Martello, S., 2010, “Piecewise Linear Approximation of Functions of Two Variables in MILP Models,” Operations Research Letters, **38**(1). https://doi.org/10.1016/j.orl.2009.09.005.

[60] Wartsila, “Wartsila Configurator.” [Online]. Available: https://www.wartsila.com/marine/engine-configurator. [Accessed: 13-Feb-2026].

[61] Vannoni, A., Sorce, A., and Massardo, A. F., 2023, *Flexible Heat and Power Generation: Market Opportunities for Combined Cycle Gas Turbines and Heat Pumps Coupling Supervisor: Co-Supervisor*.

[62] Fang, T., and Lahdelma, R., 2016, “Optimisation of Combined Heat and Power Production with Heat Storage Based on Sliding Time Window Method,” Appl. Energy, **162**(4), pp. 723–732. https://doi.org/10.1016/j.apenergy.2015.10.135.

[63] Palma-Behnke, R., Benavides, C., Lanas, F., Severino, B., Reyes, L., Llanos, J., and Saez, D., 2013, “A Microgrid Energy Management System Based on the Rolling Horizon Strategy,” IEEE Trans. Smart Grid, **4**(2). https://doi.org/10.1109/TSG.2012.2231440.

[64] Vasylyev, A., Vannoni, A., and Sorce, A., 2023, “Best Practices for Electricity Generators and Energy Storage Optimal Dispatch Problems,” Journal of Gas Turbine and Power, **146**(3). https://doi.org/https://doi.org/10.1115/1.4063529.

[65] Heragu, S. S., and Kusiak, A., 1991, “Efficient Models for the Facility Layout Problem,” Eur. J. Oper. Res., **53**(1). https://doi.org/10.1016/0377-2217(91)90088-D.

[66] Jung, S., 2016, “Facility Siting and Plant Layout Optimisation for Chemical Process Safety,” Korean Journal of Chemical Engineering, **33**(1). https://doi.org/10.1007/s11814-015-0242-4.

[67] Li, J., Ge, S., Liu, H., Du, Y., Wang, C., and Tian, W., 2024, “A Network-Secure Two-Stage Framework for Hierarchical Energy Management of EVs, Charging Stations, and Distribution Network,” Appl. Energy, **371**. https://doi.org/10.1016/j.apenergy.2024.123139.

[68] Rehman, W. ur, Bo, R., Mehdipourpicha, H., and Kimball, J. W., 2022, “Sizing Battery Energy Storage and PV System in an Extreme Fast Charging Station Considering Uncertainties and Battery Degradation,” Appl. Energy, **313**. https://doi.org/10.1016/j.apenergy.2022.118745.

[69] Khojasteh, M., Faria, P., Lezama, F., and Vale, Z., 2023, “A Robust Model for Portfolio Management of Microgrid Operator in the Balancing Market,” Energies (Basel)., **16**(4). https://doi.org/10.3390/en16041700.

[70] Sorce, A., Barberis, S., and Traverso, A., 2025, “Techno-Economic Investigation of Solutions for Decarbonizing the Thermal Management of the Stand-Still State of Combined Cycles,” E3S Web of Conferences, **663**, p. 01002. https://doi.org/10.1051/e3sconf/202566301002.

[71] L. Angello, *Hot Section Maintenance Interval Estimation for General Electric Combustion Turbines*. [Online]. Available: www.epri.com.

[72] Beagle, D., Moran, B., Mcdufford, M., and Merine, M., *HEAVY-DUTY GAS TURBINE OPERATING AND MAINTENANCE CONSIDERATIONS*.

[73] Ferriday, T. B., and Middleton, P. H., 2021, "Alkaline Fuel Cell Technology - A Review," Int. J. Hydrogen Energy, **46**(35). https://doi.org/10.1016/j.ijhydene.2021.02.203.

[74] Manzo, D., Thai, R., Le, H. T., and Venayagamoorthy, G. K., 2025, "Fuel Cell Technology Review: Types, Economy, Applications, and Vehicle-to-Grid Scheme," Sustainable Energy Technologies and Assessments, **75**. https://doi.org/10.1016/j.seta.2025.104229.

[75] Trevisan, S., Buchbjerg, B., and Guedez, R., 2022, "Power-to-Heat for the Industrial Sector: Techno-Economic Assessment of a Molten Salt-Based Solution," Energy Convers. Manag., **272**. https://doi.org/10.1016/j.enconman.2022.116362.

[76] Niccolini, C. A., Barberis, S., Sorce, A., and Magistri, L., 2025, "Techno-Economic Analysis of High-Temperature PEM Fuel Cells Integration in Cogeneration Systems," *Journal of Physics: Conference Series*. https://doi.org/10.1088/1742-6596/3143/1/012035.

[77] Bellotti, D., Rivarolo, M., and Magistri, L., 2022, "A Comparative Techno-Economic and Sensitivity Analysis of Power-to-X Processes from Different Energy Sources," Energy Convers. Manag., **260**. https://doi.org/10.1016/j.enconman.2022.115565.

[78] Caldera, U., and Breyer, C., 2017, "Learning Curve for Seawater Reverse Osmosis Desalination Plants: Capital Cost Trend of the Past, Present, and Future," Water Resour. Res., **53**(12). https://doi.org/10.1002/2017WR021402.

[79] Al-Karaghouli, A., and Kazmerski, L. L., 2013, "Energy Consumption and Water Production Cost of Conventional and Renewable-Energy-Powered Desalination Processes," Renewable and Sustainable Energy Reviews, **24**. https://doi.org/10.1016/j.rser.2012.12.064.

[80] Darwish, M. A., 1991, "Thermal Analysis of Multi-Stage Flash Desalting Systems," Desalination, **85**(1). https://doi.org/10.1016/0011-9164(91)85147-M.

[81] Al-Mutaz, I. S., and Al-Namlah, A. M., 2004, "Characteristics of Dual Purpose MSF Desalination Plants," Desalination, **166**(1–3). https://doi.org/10.1016/j.desal.2004.06.083.

[82] Buros, O. K., 2000, "The ABCs of Desalting," International Desalination Association,Topsfield, Mass, (2).

[83] Miller, J. E., *Review of Water Resources and Desalination Technologies*. [Online]. Available: http://www.doe.gov/bridge.

[84] Mulder, M., 1991, "Basic Principles of Membrane Technology." https://doi.org/10.1524/zpch.1998.203.part_1_2.263.

[85] Al-Karaghouli, A., Renne, D., and Kazmerski, L. L., 2010, "Technical and Economic Assessment of Photovoltaic-Driven Desalination Systems," Renew. Energy, **35**(2). https://doi.org/10.1016/j.renene.2009.05.018.

[86] Vasylyev, A., Vannoni, A., and Sorce, A., 2023, "Optimal Dispatch of Battery Energy Storage Considering Cycling and Calendar Ageing," *E3S Web of Conferences*. https://doi.org/10.1051/e3sconf/202341401004.

[87] Vasylyev, A., Vannoni, A., and Sorce, A., 2025, “Optimal Dispatch of Li-Ion Battery Energy Storage, Reviewing and Considering Cycling and Calendar Ageing Models,” Appl. Therm. Eng., **265**. https://doi.org/10.1016/j.applthermaleng.2025.125597.

[88] Blakers, A., Stocks, M., Lu, B., and Cheng, C., 2021, “A Review of Pumped Hydro Energy Storage,” Progress in Energy, **3**(2). https://doi.org/10.1088/2516-1083/abeb5b.

[89] Barbour, E., Wilson, I. A. G., Radcliffe, J., Ding, Y., and Li, Y., 2016, “A Review of Pumped Hydro Energy Storage Development in Significant International Electricity Markets,” Renewable and Sustainable Energy Reviews, **61**. https://doi.org/10.1016/j.rser.2016.04.019.

[90] Zhao, C., Andersen, P. B., Træholt, C., and Hashemi, S., 2023, “Grid-Connected Battery Energy Storage System: A Review on Application and Integration,” Renewable and Sustainable Energy Reviews, **182**. https://doi.org/10.1016/j.rser.2023.113400.

[91] Papakonstantinou, A. G., Konstanteas, A. I., and Papathanassiou, S. A., 2023, “Solutions to Enhance Frequency Regulation in an Island System with Pumped-Hydro Storage under 100% Renewable Energy Penetration,” IEEE Access, **11**. https://doi.org/10.1109/ACCESS.2023.3296890.

[92] Rancilio, G., Lucas, A., Kotsakis, E., Fulli, G., Merlo, M., Delfanti, M., and Masera, M., 2019, “Modeling a Large-Scale Battery Energy Storage System for Power Grid Application Analysis,” Energies (Basel)., **12**(17). https://doi.org/10.3390/en12173312.

[93] Energy Agency, I., *World Energy Outlook Special Report Batteries and Secure Energy Transitions*. [Online]. Available: www.iea.org.

[94] Xu, B., Oudalov, A., Ulbig, Dipl.-I. A., and Zürich, Z., 2013, *Degradation-Limiting Optimisation of Battery Energy Storage Systems Operation*.

[95] Stroe, D. I., Swierczynski, M., Stroe, A. I., Laerke, R., Kjaer, P. C., and Teodorescu, R., 2016, “Degradation Behavior of Lithium-Ion Batteries Based on Lifetime Models and Field Measured Frequency Regulation Mission Profile,” IEEE Trans. Ind. Appl., **52**(6). https://doi.org/10.1109/TIA.2016.2597120.

[96] Rancilio Supervisor, G., Delfanti Tutor, M., and Merlo, M., *Department Of Energy Doctoral Programme In Electrical Engineering Abate The Barriers: Opening Electricity Markets To Storage And Res*. [Online]. Available: https://www.politesi.polimi.it/handle/10589/188700. [Accessed: 22-Jan-2024].

[97] Stroe, D. I., 2014, “Lifetime Models for Lithium-Ion Batteries Used in Virtual Power Plant Applications.” [Online]. Available: https://vbn.aau.dk/en/publications/lifetime-models-for-lithium-ion-batteries-used-in-virtual-power-p. [Accessed: 22-Jan-2024].

[98] Stroe, D. I., Knap, V., Swierczynski, M., Stroe, A. I., and Teodorescu, R., 2017, “Operation of a Grid-Connected Lithium-Ion Battery Energy Storage System for Primary Frequency Regulation: A Battery Lifetime Perspective,” IEEE Trans. Ind. Appl., **53**(1). https://doi.org/10.1109/TIA.2016.2616319.

[99] Zhou, C., Qian, K., Allan, M., and Zhou, W., 2011, “Modeling of the Cost of EV Battery Wear Due to V2G Application in Power Systems,” IEEE Transactions on Energy Conversion, **26**(4). https://doi.org/10.1109/TEC.2011.2159977.

[100] Mallon, K. R., Assadian, F., and Fu, B., 2017, “Analysis of On-Board Photovoltaics for a Battery Electric Bus and Their Impact on Battery Lifespan,” Energies (Basel)., **10**(7). https://doi.org/10.3390/en10070943.

[101] Xu, B., Oudalov, A., Ulbig, A., Andersson, G., and Kirschen, D. S., 2018, “Modeling of Lithium-Ion Battery Degradation for Cell Life Assessment,” IEEE Trans. Smart Grid, **9**(2). https://doi.org/10.1109/TSG.2016.2578950.

[102] Sayfutdinov, T., Ali, M., and Khamisov, O., 2020, “Alternating Direction Method of Multipliers for the Optimal Siting, Sizing, and Technology Selection of Li-Ion Battery Storage,” Electric Power Systems Research, **185**. https://doi.org/10.1016/j.epsr.2020.106388.

[103] Sayfutdinov, T., Patsios, C., Vorobev, P., Gryazina, E., Greenwood, D. M., Bialek, J. W., and Taylor, P. C., 2020, “Degradation and Operation-Aware Framework for the Optimal Siting, Sizing, and Technology Selection of Battery Storage,” IEEE Trans. Sustain. Energy, **11**(4). https://doi.org/10.1109/TSTE.2019.2950723.

[104] Fallahifar, R., and Kalantar, M., 2023, “Optimal Planning of Lithium Ion Battery Energy Storage for Microgrid Applications: Considering Capacity Degradation,” J. Energy Storage, **57**. https://doi.org/10.1016/j.est.2022.106103.

[105] Ju, C., Wang, P., Goel, L., and Xu, Y., 2018, “A Two-Layer Energy Management System for Microgrids with Hybrid Energy Storage Considering Degradation Costs,” IEEE Trans. Smart Grid, **9**(6). https://doi.org/10.1109/TSG.2017.2703126.

[106] Liaw, B. Y., Roth, E. P., Jungst, R. G., Nagasubramanian, G., Case, H. L., and Doughty, D. H., 2003, “Correlation of Arrhenius Behaviors in Power and Capacity Fades with Cell Impedance and Heat Generation in Cylindrical Lithium-Ion Cells,” *Journal of Power Sources*. https://doi.org/10.1016/S0378-7753(03)00196-4.

[107] Swierczynski, M., Stroe, D. I., Stan, A. I., Teodorescu, R., and Kær, S. K., 2015, “Lifetime Estimation of the Nanophosphate LiFePO4/C Battery Chemistry Used in Fully Electric Vehicles,” IEEE Trans. Ind. Appl., **51**(4). https://doi.org/10.1109/TIA.2015.2405500.

[108] BloombergNEF, 2023, “Lithium-Ion Battery Pack Prices.” [Online]. Available: https://about.bnef.com/blog/lithium-ion-battery-pack-prices-hit-record-low-of-139-kwh/. [Accessed: 13-Feb-2024].

[109] IEA, 2023, *World Energy Outlook 2023*. [Online]. Available: www.iea.org/terms.

[110] IMO, 2018, *INITIAL IMO STRATEGY ON REDUCTION OF GHG EMISSIONS FROM SHIPS*. [Online]. Available: http://www.imo.org.

[111] Armellini, A., Daniotti, S., Pinamonti, P., and Reini, M., 2018, “Evaluation of Gas Turbines as Alternative Energy Production Systems for a Large Cruise Ship to Meet New Maritime Regulations,” Appl. Energy, **211**, pp. 306–317. https://doi.org/10.1016/J.APENERGY.2017.11.057.

[112] Balcombe, P., Brierley, J., Chester, L., Skatvedt, L., Speirs, J., Hawkes, A., and Staffell, I., 2019, *How to Decarbonise International Shipping: Options for Fuels, Technologies and Policies*.

[113] Rivarolo, M., Rattazzi, D., and Magistri, L., 2018, “Best Operative Strategy for Energy Management of a Cruise Ship Employing Different Distributed Generation Technologies,” Int. J. Hydrogen Energy, **43**(52), pp. 23500–23510. https://doi.org/10.1016/j.ijhydene.2018.10.217.

[114] Inal, O. B., and Deniz, C., 2020, “Assessment of Fuel Cell Types for Ships: Based on Multi-Criteria Decision Analysis,” J. Clean. Prod., **265**. https://doi.org/10.1016/j.jclepro.2020.121734.

[115] Bouakkaz, A., Mena, A. J. G., Haddad, S., and Ferrari, M. L., 2021, “Efficient Energy Scheduling Considering Cost Reduction and Energy Saving in Hybrid Energy System with Energy Storage,” J. Energy Storage, **33**. https://doi.org/10.1016/j.est.2020.101887.

[116] Baldi, F., Ahlgren, F., Nguyen, T. Van, Thern, M., and Andersson, K., 2018, “Energy and Exergy Analysis of a Cruise Ship,” Energies (Basel)., **11**(10). https://doi.org/10.3390/en11102508.

[117] Baldi, F., Ahlgren, F., Melino, F., Gabrielii, C., and Andersson, K., 2016, “Optimal Load Allocation of Complex Ship Power Plants,” Energy Convers. Manag., **124**, pp. 344–356. https://doi.org/10.1016/j.enconman.2016.07.009.

[118] Baldi, F., Ahlgren, F., Nguyen, T. Van, Thern, M., and Andersson, K., 2018, “Energy and Exergy Analysis of a Cruise Ship,” Energies (Basel)., **11**(10). https://doi.org/10.3390/en11102508.

[119] 2024, “WinGD General Technical Data (GTD).”

[120] 2023, *Heating Systems - Steam Boilers and Waste Heat Boilers*.

[121] 2023, *Alfa Laval Aalborg - Micro Waste Heat Recovery Boiler*. [Online]. Available: www.alfalaval.com.

[122] 2023, *Alfa Laval Aalborg-Xs-Tc7a*.

[123] 2023, *Energy Storage Systems - Corvus Orca*.

[124] 2023, *Energy Storage Systems 12 Corvus Energy • Corvus Blue Whale*.

[125] 2023, *Energy Storage Systems 14 Corvus Energy Corvus Energy Safety Innovations Passive Single-Cell-Level Thermal Runaway (TR) Isolation Corvus Dolphin Energy NxtGen*.

[126] 2023, *Nidec Marine Battery*. [Online]. Available: www.nidec-industrial.com.

[127] 2024, “EMEA Bunker Prices.” [Online]. Available: https://shipandbunker.com/prices/emea. [Accessed: 10-Jun-2024].

[128] Marine Benchmark, 2020, *Maritime CO2 Emissions*. [Online]. Available: https://safety4sea.com/wp-content/uploads/2020/11/Marine-Benchmark-Maritime-CO2-Emissions-2020_11.pdf. [Accessed: 10-Jun-2024].

[129] World Bank, “State and Trends of Carbon Pricing Dashboard.”

[130] Kumar, P., Date, A., Mahmood, N., Kumar Das, R., and Shabani, B., 2024, “Freshwater Supply for Hydrogen Production: An Underestimated Challenge,” Int. J. Hydrogen Energy, **78**. https://doi.org/10.1016/j.ijhydene.2024.06.257.

[131] Rivard, E., Trudeau, M., and Zaghib, K., 2019, "Hydrogen Storage for Mobility: A Review," Materials, **12**(12). https://doi.org/10.3390/ma12121973.

[132] Arefin, S. S., and Das, N., 2017, "Optimised Hybrid Wind-Diesel Energy System with Feasibility Analysis," Technology and Economics of Smart Grids and Sustainable Energy, **2**(1). https://doi.org/10.1007/s40866-017-0025-6.

[133] Parthasarathy, P., and Narayanan, S. K., 2014, "Effect of Hydrothermal Carbonization Reaction Parameters On," Environ. Prog. Sustain. Energy, **33**(3), pp. 676–680. https://doi.org/10.1002/ep.

[134] Bird, L., Lew, D., Milligan, M., Carlini, E. M., Estanqueiro, A., Flynn, D., Gomez-Lazaro, E., Holttinen, H., Menemenlis, N., Orths, A., Eriksen, P. B., Smith, J. C., Soder, L., Sorensen, P., Altiparmakis, A., Yasuda, Y., and Miller, J., 2016, "Wind and Solar Energy Curtailment: A Review of International Experience," Renewable and Sustainable Energy Reviews, **65**, pp. 577–586. https://doi.org/10.1016/j.rser.2016.06.082.

[135] Dubey, A., Sorce, A., Rivarolo, M., Traverso, A., and Sala, S., 2025, "Techno-Economic Analysis of Pressure Gain Combustion Gas Turbine for Island Grids with High Renewable Solar Share," Appl. Therm. Eng., **265**(January 2024), p. 125609. https://doi.org/10.1016/j.applthermaleng.2025.125609.

[136] Papaefthymiou, S. V., Karamanou, E. G., Papathanassiou, S. A., and Papadopoulos, M. P., 2010, "A Wind-Hydro-Pumped Storage Station Leading to High RES Penetration in the Autonomous Island System of Ikaria," IEEE Trans. Sustain. Energy, **1**(3). https://doi.org/10.1109/TSTE.2010.2059053.

[137] Malamaki, K. N. D., Fotopoulou, M., Andriopoulos, N., Martinez-Lopez, D., Ferrer-Fernandez, P., Tzanis, N., Lampsidis, G., Kaousias, K., Chassioti, E., and Moraitis, I., 2024, "Optimal Short-Term Dispatch of Insular Systems: The Case of Ikaria," *2024 International Conference on Smart Energy Systems and Technologies: Driving the Advances for Future Electrification, SEST 2024 - Proceedings*, Institute of Electrical and Electronics Engineers Inc. https://doi.org/10.1109/SEST61601.2024.10694615.

[138] Jørgensen, B., Holst, ;, Madsen, P., Hauge, ;, Giebel, G. ;, Martí, I. ;, and Thomsen, K., "General Rights DTU International Energy Report 2021: Perspectives on Wind Energy." https://doi.org/10.11581/DTU.00000200.

[139] Salsabila, N., Anwar, A., Shubbar, H. T., Khan, M. I., Al-Ansari, T., and Bicer, Y., 2025, "Comparative Sustainability Assessment of Hybrid Desalination Systems for Freshwater Production," Energy Nexus, **18**. https://doi.org/10.1016/j.nexus.2025.100440.

[140] Shemer, H., and Semiat, R., 2017, "Sustainable RO Desalination – Energy Demand and Environmental Impact," Desalination, **424**. https://doi.org/10.1016/j.desal.2017.09.021.

[141] Nassrullah, H., Anis, S. F., Hashaikeh, R., and Hilal, N., 2020, "Energy for Desalination: A State-of-the-Art Review," Desalination, **491**. https://doi.org/10.1016/j.desal.2020.114569.

[142] Kyriakarakos, G., Papadakis, G., and Karavitis, C. A., 2022, "Renewable Energy Desalination for Island Communities: Status and Future Prospects in Greece," Sustainability (Switzerland), **14**(13). https://doi.org/10.3390/su14138176.

[143] Agnew, G. D., Bozzolo, M., Moritz, R. R., and Berenyi, S., 2005, "The Design and Integration of the Rolls-Royce Fuel Cell Systems 1MW SOFC," *Proceedings of the ASME Turbo Expo*. https://doi.org/10.1115/GT2005-69122.

[144] Magistri, L., Bozzolo, M., Tarnowski, O., Agnew, G., and Massardo, A. F., 2007, "Design and Off-Design Analysis of a MW Hybrid System Based on Rolls-Royce Integrated Planar Solid Oxide Fuel Cells," J. Eng. Gas Turbine. Power, **129**(3). https://doi.org/10.1115/1.1839917.

[145] Thomas Brinkhoff, "City Population." [Online]. Available: https://www.citypopulation.de/. [Accessed: 17-Mar-2026].

[146] Spyrou, I. D., and Anagnostopoulos, J. S., 2010, "Design Study of a Stand-Alone Desalination System Powered by Renewable Energy Sources and a Pumped Storage Unit," Desalination, **257**(1–3). https://doi.org/10.1016/j.desal.2010.02.033.

[147] Chen, Z., Su, C., Zhan, H., Chen, L., Wang, W., Zhang, H., Chen, X., Sun, C., Kong, Y., Yang, L., Du, X., and Zhang, N., 2024, "Thermodynamic and Economic Analyses of Nuclear Power Plant Integrating with Seawater Desalination and Hydrogen Production for Peak Shaving," Int. J. Hydrogen Energy, **82**. https://doi.org/10.1016/j.ijhydene.2024.08.055.

[148] International Renewable Energy Agency (IRENA), 2024, *RENEWABLE POWER GENERATION COSTS IN 2023 2*. [Online]. Available: www.irena.org.